



The MOSDEF Survey: The Evolution of the Mass–Metallicity Relation from $z = 0$ to $z \sim 3.3^*$

Ryan L. Sanders^{1,13} , Alice E. Shapley² , Tucker Jones¹ , Naveen A. Reddy³ , Mariska Kriek⁴ , Brian Siana³ , Alison L. Coil⁵ , Bahram Mobasher³, Irene Shvaei^{6,13} , Romeel Dave⁷ , Mojegan Azadi⁸ , Sedona H. Price⁹ , Gene Leung¹⁰ , William R. Freeman³ , Tara Fetherolf³ , Laura de Groot¹¹ , Tom Zick⁴, and Guillermo Barro¹²

¹ Department of Physics and Astronomy, University of California, Davis, One Shields Avenue, Davis, CA 95616, USA; rlsand@ucdavis.edu

² Department of Physics & Astronomy, University of California, Los Angeles, 430 Portola Plaza, Los Angeles, CA 90095, USA

³ Department of Physics & Astronomy, University of California, Riverside, 900 University Avenue, Riverside, CA 92521, USA

⁴ Astronomy Department, University of California, Berkeley, CA 94720, USA

⁵ Center for Astrophysics and Space Sciences, University of California, San Diego, 9500 Gilman Drive, La Jolla, CA 92093-0424, USA

⁶ Department of Astronomy/Steward Observatory, 933 North Cherry Avenue, Room N204, Tucson, AZ, 85721-0065, USA

⁷ Institute for Astronomy, University of Edinburgh, James Clerk Maxwell Building, Peter Guthrie Tait Road, Edinburgh, EH9 3FD, UK

⁸ Harvard-Smithsonian Center for Astrophysics, 60 Garden Street, Cambridge, MA 02138, USA

⁹ Max-Planck-Institut für extraterrestrische Physik, Postfach 1312, Garching, D-85741, Germany

¹⁰ Department of Astronomy, University of Texas at Austin, 2515 Speedway, Stop C1400, Austin, TX 78712, USA

¹¹ Department of Physics, The College of Wooster, 1189 Beall Avenue, Wooster, OH 44691, USA

¹² Department of Physics, University of the Pacific, 3601 Pacific Avenue, Stockton, CA 95211, USA

Received 2020 September 14; revised 2021 April 1; accepted 2021 April 2; published 2021 June 9

Abstract

We investigate the evolution of galaxy gas-phase metallicity (O/H) over the range $z = 0$ – 3.3 using samples of ~ 300 galaxies at $z \sim 2.3$ and ~ 150 galaxies at $z \sim 3.3$ from the MOSDEF survey. This analysis crucially utilizes different metallicity calibrations at $z \sim 0$ and $z > 1$ to account for evolving interstellar medium (ISM) conditions. We find significant correlations between O/H and stellar mass (M_*) at $z \sim 2.3$ and $z \sim 3.3$. The low-mass power-law slope of the mass–metallicity relation (MZR) is remarkably invariant over $z = 0$ – 3.3 , such that $\text{O/H} \propto M_*^{0.30}$ at all redshifts in this range. At fixed M_* , O/H decreases with increasing redshift as $d\log(\text{O/H})/dz = -0.11 \pm 0.02$. We find no evidence that the fundamental metallicity relation between M_* , O/H, and star formation rate evolves out to $z \sim 3.3$. We employ analytic chemical evolution models to place constraints on the mass and metal loading factors of galactic outflows. The efficiency of metal removal increases toward lower M_* at fixed redshift and toward higher redshift at fixed M_* . These models suggest that the slope of the MZR is primarily set by the scaling of the outflow metal loading factor with M_* , not by the change in gas fraction as a function of M_* . The evolution toward lower O/H at fixed M_* with increasing redshift is driven by both higher gas fraction (leading to stronger dilution of ISM metals) and higher metal removal efficiency. These results suggest that the processes governing the smooth baryonic growth of galaxies via gas flows and star formation hold in the same form over at least the past 12 Gyr.

Unified Astronomy Thesaurus concepts: Galaxy evolution (594); Galaxy chemical evolution (580); High-redshift galaxies (734); Galaxy abundances (574); Chemical abundances (224); Metallicity (1031); Galaxy winds (626); Emission line galaxies (459)

1. Introduction

The metallicity of the interstellar medium (ISM) of galaxies is a powerful tool with which to understand the baryonic processes that govern the secular growth of galaxies. Gas-phase metallicity is closely related to past and current star formation (the nucleosynthetic origin of metals), the gas reservoir, and gas flows including accretion from the intergalactic medium (IGM) and circumgalactic medium (CGM), outflows driven by feedback from supernovae (SNe) and accreting black holes, and recycling of material from past outflows. Characterizing how metallicity scales with global galaxy properties including stellar mass (M_*) and star formation rate (SFR) over a range of redshifts can constrain the scaling of gas accretion and outflow

rates with these properties, providing insight into galaxy growth throughout cosmic history.

The relation between the gas-phase oxygen abundance (O/H) and M_* , referred to as the mass–metallicity relation (MZR), has been extensively studied in the local universe, where O/H and M_* are found to be positively correlated over five decades in M_* (e.g., Lequeux et al. 1979; Tremonti et al. 2004; Lee et al. 2006; Kewley & Ellison 2008; Mannucci et al. 2010; Berg et al. 2012; Andrews & Martini 2013, hereafter AM13; Blanc et al. 2019; Curti et al. 2020b). At $z = 0$, the MZR is generally described by a power law at low masses ($\lesssim 10^{10} M_\odot$) that begins to flatten toward an asymptotic value in metallicity at high masses.

The MZR has been observed out to $z \sim 3.5$ and evolves such that O/H decreases with increasing redshift at fixed M_* (Savaglio et al. 2005; Erb et al. 2006a; Maiolino et al. 2008, hereafter M08; Mannucci et al. 2009; Zahid et al. 2011, 2014a, 2014b; Wuyts et al. 2012, 2016; Belli et al. 2013; Henry et al. 2013; Kulas et al. 2013; Cullen et al. 2014; Maier et al. 2014; Steidel et al. 2014; Troncoso et al. 2014; Kacprzak et al. 2015, 2016; Ly et al. 2015, 2016;

* Based on data obtained at the W.M. Keck Observatory, which is operated as a scientific partnership among the California Institute of Technology, the University of California, and NASA, and was made possible by the generous financial support of the W.M. Keck Foundation.

¹³ Hubble Fellow.

Sanders et al. 2015, 2018, 2020b; Hunt et al. 2016; Onodera et al. 2016; Suzuki et al. 2017). At $z > 4$, the commonly used rest-optical metallicity indicators redshift out of atmospheric transmission windows that are accessible from the ground (i.e., beyond $2.5 \mu\text{m}$). The metallicity of only a single galaxy at $z = 4.4$ has been measured from a rest-optical line ratio (Shapley et al. 2017). Attempts have been made to constrain the MZR at redshifts above $z = 4$ through rest-UV metal absorption lines at $z = 4\text{--}5$ (Faisst et al. 2016) and far-IR [O III] $88 \mu\text{m}$ emission detected with the Atacama Large Millimeter/submillimeter Array at $z \sim 8$ (Jones et al. 2020), but these methods currently suffer from large systematic uncertainties in metallicity, precluding useful comparisons with results from rest-optical line ratios at lower redshift. A robust picture of MZR evolution at $z > 4$ will require spectra from the James Webb Space Telescope (JWST) that can access wavelengths beyond $2.5 \mu\text{m}$.

In past studies, the evolution of the MZR has been found to be slow out to $z \sim 2.5$ where O/H is ~ 0.3 dex lower than at $z \sim 0$ at fixed M_* (e.g., Erb et al. 2006a; Steidel et al. 2014; Sanders et al. 2015). Rapid metallicity evolution has been inferred above $z \sim 3$, with metallicity dropping 0.3–0.4 dex between $z \sim 2.5$ and $z \sim 3.5$ despite only 1 Gyr of cosmic time passing between these redshifts (Maiolino et al. 2008; Mannucci et al. 2009; Troncoso et al. 2014; Onodera et al. 2016). Such fast evolution between $z \sim 2.5$ and $z \sim 3.5$ is not observed in numerical simulations of galaxy formation and evolution, which instead find a smooth decline in metallicity at fixed M_* out to $z \sim 6$ (e.g., Ma et al. 2016; Davé et al. 2017; De Rossi et al. 2017; Torrey et al. 2019). There is thus tension between previous constraints on the MZR at $z > 3$ and models of hierarchical galaxy formation. Suzuki et al. (2017) found very little MZR evolution between $z \sim 2$ and $z \sim 3.2$, but their comparison relies on metallicities derived using different indicators and calibrations at each redshift and the accompanying systematic effects are unclear.

The $z = 0$ MZR has been found to have a secondary dependence on SFR such that there is a three-parameter relation among M_* , SFR, and O/H, known as the fundamental metallicity relation (FMR; e.g., Ellison et al. 2008; Lara-López et al. 2010; Mannucci et al. 2010; Yates et al. 2012; Cresci et al. 2019; Curti et al. 2020b). In the FMR, O/H decreases with increasing SFR at fixed M_* . The FMR is closely connected to a relation among M_* , O/H, and gas fraction in which O/H and gas fraction are anticorrelated at fixed M_* (Bothwell et al. 2013, 2016a, 2016b; Brown et al. 2018). The FMR was proposed to be independent of redshift out to $z \sim 2.5$ (Mannucci et al. 2010). Due to small samples, low-signal-to-noise ratio (S/N) measurements, and biases in metallicity estimates, early work yielded inconclusive results regarding the redshift invariance of the FMR and whether the high-redshift MZR displayed any secondary dependence on SFR (e.g., Wuyts et al. 2012, 2014; Belli et al. 2013; Stott et al. 2013; Steidel et al. 2014; Cullen et al. 2014; Zahid et al. 2014b; Salim et al. 2015; Sanders et al. 2015; Yabe et al. 2015; Grasshorn Gebhardt et al. 2016; Kashino et al. 2017). With improved data sets, recent work has found that the MZR does depend secondarily on SFR at $z \sim 2.3$ (Sanders et al. 2018) and that the FMR holds out to $z \sim 2.5$, though a small offset of ~ 0.1 dex from the local FMR is seen in some studies (Sanders et al. 2018; Cresci et al. 2019; Curti et al. 2020b). Galaxies at $z > 3$ do not appear to follow the FMR, with metallicities $\sim 0.3\text{--}0.6$ dex below the metallicity predicted by the local relation (Troncoso et al. 2014; Onodera et al. 2016).

A class of chemical evolution models known as “bathtub” or “equilibrium” models has shown success in reproducing the observed MZR and its evolution, as well as the FMR (e.g., Finlator & Davé 2008; Peebles & Shankar 2011, hereafter PS11; Davé et al. 2012; Lilly et al. 2013). These models operate on the principle of conservation of baryonic mass in galaxies, establishing a balance between the mass inflow and outflow rates, SFR, rate of returning stellar material back into the ISM, and rate of change of the total gas mass (some models assume the latter quantity is negligible; Davé et al. 2012). Galaxies satisfying this balance between gas flows and internal gas processing are said to be in equilibrium. In this theoretical framework, the MZR arises because gas fractions are higher and/or material is more efficiently removed by outflows at lower M_* (Tremonti et al. 2004; Davé et al. 2012; Lilly et al. 2013). Other secondary effects may come into play as well, including variations with M_* of the stellar initial mass function (IMF) that affect metal yields (Köppen et al. 2007) and the metallicity of accreted gas through galactic fountains and outflow recycling (Davé et al. 2011; Anglés-Alcázar et al. 2017). These equilibrium models provide a way to utilize MZR and FMR observations to constrain gas accretion and outflow rates.

The shape and normalization of the MZR and FMR are sensitive to the method used to derive metallicities. Given the difficulty of measuring faint O recombination lines or auroral emission lines (e.g., [O III] $\lambda 4363$) that are required to employ the most robust metallicity derivation techniques, the use of calibrations between ratios of strong emission lines and metallicity is the most practical approach to measure metallicity scaling relations for large and representative samples spanning wide ranges in M_* and SFR (e.g., Kewley & Dopita 2002; Pettini & Pagel 2004; Maiolino et al. 2008; Curti et al. 2017, hereafter C17). Kewley & Ellison (2008) showed that the form of the $z \sim 0$ MZR varies widely in both high-mass asymptotic O/H and low-mass slope based on the choice of strong-line metallicity calibration. A robust translation between strong-line ratio and O/H is therefore critical to any analysis of metallicity scaling relations.

The problem of calibration choice is further complicated when investigating the evolution of the MZR and FMR over a wide range of redshifts. Star-forming galaxies at $z \sim 2$ have been shown to follow different excitation sequences from those of their $z \sim 0$ counterparts and local H II regions, most notably in the [N II] Baldwin, Phillips, & Terlevich (BPT; Baldwin et al. 1981) diagram (e.g., Steidel et al. 2014, 2016; Shapley et al. 2015; Sanders et al. 2016; Kashino et al. 2017; Strom et al. 2017, 2018; Runco et al. 2021; Topping et al. 2020a, 2020b). There is consensus that the excitation properties of $z > 1$ galaxies signify that high-redshift H II regions have a set of ionized gas physical properties that is distinct from those of $z = 0$ H II regions. The relation between strong-line ratios and metallicity depends sensitively on these same physical properties (e.g., Kewley et al. 2013), thus it is probable that metallicity calibrations evolve with redshift. Nevertheless, it remains the overwhelmingly common practice to apply $z = 0$ metallicity calibrations to $z > 1$ galaxies. A robust analysis of the evolution of the MZR and FMR must take into account the evolution of metallicity calibrations accordingly by applying appropriate calibrations at each redshift.

In this work, we investigate the evolution of the MZR and FMR over $z = 0\text{--}3.3$ using large samples of representative star-forming galaxies at $z \sim 2.3$ and $z \sim 3.3$ from the MOSDEF

survey. In addition to a significantly larger sample size at $z > 3$, our analysis includes several key improvements over past studies, including more robust dust corrections for $z > 3$ galaxies calibrated to Balmer decrement measurements at $z \sim 2.3$, metallicities derived from a uniform set of emission lines that is the same for samples at all redshifts, and, for the first time, the application of different metallicity calibrations to samples in the local and high-redshift universe to reflect evolving ionized gas conditions in star-forming regions. We combine our improved constraints on MZR evolution with analytic chemical evolution models to infer the roles of metal-enriched outflows and gas fractions in controlling the slope and evolution of the MZR.

This paper is organized as follows. In Section 2, we describe the measurements, samples, and derived quantities. We report the methods for deriving metallicities in Section 3. We characterize the MZR at $z \sim 2.3$ and $z \sim 3.3$ and investigate the evolution of the FMR in Section 4. We interpret our results using analytic chemical evolution models in Section 5, placing constraints on the metal loading factor of outflows and investigating which physical mechanisms govern the slope and evolution of the MZR. We discuss our results in Section 6, comparing to past high-redshift MZR and FMR studies and considering the implications of our models for the evolution of the outflow mass-loading factor and its scaling with stellar mass. Finally, in Section 7, we summarize our conclusions. Throughout, we assume a standard Λ CDM cosmology with $H_0 = 70 \text{ km s}^{-1} \text{ Mpc}^{-1}$, $\Omega_m = 0.3$, and $\Omega_\Lambda = 0.7$. Magnitudes are in the AB system (Oke & Gunn 1983) and wavelengths are given in Å. The term metallicity refers to the gas-phase oxygen abundance unless otherwise stated.

2. Data, Measurements, and Derived Quantities

2.1. The MOSDEF survey

Our high-redshift galaxy samples are drawn from the MOSDEF survey, a 4 yr program that used the Multi-Object Spectrometer For Infrared Exploration (MOSFIRE; McLean et al. 2012) on the 10 m Keck I telescope to obtain rest-frame optical spectra of galaxies at $z = 1.4\text{--}3.8$ (Kriek et al. 2015). Galaxies were targeted in three redshift ranges: $1.37 \leq z \leq 1.70$, $2.09 \leq z \leq 2.61$, and $2.95 \leq z \leq 3.80$. In these redshift intervals, strong rest-optical emission lines fall within windows of near-infrared atmospheric transmission. Here, we focus on the higher two redshift bins. At $z \sim 2.3$ (3.3), [O II] $\lambda\lambda$ 3726,3729 and [Ne III] λ 3869 fall in the J (H) band; H β and [O III] $\lambda\lambda$ 4959,5007 fall in the H (K) band; and H α , [N II] $\lambda\lambda$ 6548,6584, and [S II] $\lambda\lambda$ 6716,6731 fall in the K band (these lines are not covered at $z \sim 3.3$). Targets were drawn from the 3D-HST survey photometric catalogs (Brammer et al. 2012; Skelton et al. 2014; Momcheva et al. 2016), selected based on H -band (rest-frame optical) magnitude as measured from Hubble Space Telescope (HST)/WFC3 F160W imaging ($H_{\text{AB}} < 24.5$ (25.0) at $z \sim 2.3$ (3.3)) and redshift (spectroscopic or HST grism when available, otherwise photometric). The H -band magnitude limit corresponds to an approximate stellar mass limit of $\log(M_*/M_\odot) \sim 9.0$ that is constant across the three redshift bins. The completed survey targeted ~ 1500 galaxies and measured ~ 1300 redshifts, with approximately half of the sample at $z \sim 2.3$ and one quarter at $z \sim 3.3$. For a detailed description of the MOSDEF survey design and data reduction, see Kriek et al. (2015).

2.2. Measurements and Derived Quantities

2.2.1. Emission-line Fluxes and Redshifts

We utilize measurements of redshifts and emission-line fluxes from extracted 1D science spectra that have been corrected for slit losses, as described in Kriek et al. (2015). The absolute flux calibration of slit-loss-corrected science spectra is accurate to better than 18% on average with a 16% uncertainty, and the relative calibration between filters is biased less than 13% with an uncertainty of 18%. The MOSDEF line measurements thus provide robust line ratios even when the lines fall in different filters (e.g., [O III]/[O II], H α /H β) and total line fluxes for calculating SFRs.

2.2.2. Stellar Masses and Emission-line-corrected Photometry

Stellar masses were determined using the extensive broadband photometry in the CANDELS fields (Grogin et al. 2011; Koekemoer et al. 2011) spanning observed-frame optical to mid-infrared (rest-frame UV to near-IR), as cataloged by the 3D-HST survey team (Skelton et al. 2014; Momcheva et al. 2016). Because galaxies at $z > 2$ commonly have large emission-line equivalent widths ($\text{EW}_{\text{obs}} \gtrsim 300 \text{ \AA}$; Reddy et al. 2018b), it is important to correct photometric measurements for the contribution from emission lines before fitting with stellar-continuum-only models.

Photometry in rest-optical filters was corrected using the following method. For each MOSDEF target with a secure spectroscopic redshift and at least one emission line detected at $S/N \geq 3$, a model emission-line-only spectrum was created by summing the best-fit Gaussian profiles of all emission lines with $S/N \geq 3$. This model spectrum was passed through the transmission curves of all filters covering the rest-frame optical to determine the flux contributed by emission lines in each filter, and this flux was subtracted from the original photometric measurements. For each filter, if the difference between the original and corrected photometry was $> 1\sigma$ based on the original photometric uncertainty, then the corrected photometry is used. No correction is made if the difference is $\leq 1\sigma$. Uncertainties on MOSDEF emission-line fluxes are propagated into uncertainties on corrected photometry.

Emission-line-corrected photometry for each target was fit using flexible stellar population synthesis models (Conroy et al. 2009) and the spectral energy distribution (SED) fitting code FAST (Kriek et al. 2009). Constant star formation histories, solar stellar metallicities, the Calzetti et al. (2000) attenuation curve, and a Chabrier (2003) IMF are assumed for all galaxies in the sample. We investigate the effects of varying the SED fitting assumptions on our results in Section 4.4. This SED fitting procedure yields stellar masses, $E(B - V)_{\text{stars}}$, SFR(SED), and a best-fit model of the stellar continuum. Hydrogen Balmer recombination-line fluxes are corrected for the effects of stellar Balmer absorption by measuring the absorption line flux from the best-fit SED model and applying a correction equal to the total absorption flux multiplied by an emission filling fraction of 0.36 (0.23) for H α (H β ; Reddy et al. 2018b). Typical Balmer absorption corrections are $\lesssim 1\%$ ($\lesssim 3\%$) for H α (H β).

2.2.3. Reddening Correction

Dust-corrected line fluxes are required for both SFR and metallicity calculations. When both H α and H β are detected

with $S/N \geq 3$, $E(B - V)_{\text{gas}}$ is calculated using the Balmer decrement assuming an intrinsic ratio of $H\alpha/H\beta = 2.86$ (Osterbrock & Ferland 2006) and the Milky Way extinction curve (Cardelli et al. 1989). A nebular attenuation curve derived directly from $z \sim 2$ MOSDEF data is consistent with the Milky Way curve, suggesting this curve is an appropriate assumption (Reddy et al. 2020). However, $H\alpha$ is not covered for galaxies at $z > 2.65$ and $H\beta$ is not always detected for galaxies in the $z \sim 2.3$ bin. An alternative dust correction method that does not require detections of multiple Balmer lines is needed for these targets.

It is common practice to estimate $E(B - V)_{\text{gas}}$ from the stellar continuum reddening derived from SED fitting, either assuming nebular reddening is larger than stellar reddening as found in local starbursts ($E(B - V)_{\text{gas}} = E(B - V)_{\text{stars}}/0.44$; Calzetti et al. 2000) and low-metallicity high-redshift galaxies (Shivaei et al. 2020) or that the two are equal as found by several studies at $z > 1$ (Erb et al. 2006b; Kashino et al. 2013; Pannella et al. 2015; Reddy et al. 2015; Puglisi et al. 2016). Nebular reddening of high-redshift galaxies has also been estimated from the rest-UV slope at 1600 Å, β_{UV} , by assuming a relation between β_{UV} and $A_{\text{UV,stars}}$ (e.g., Meurer et al. 1999; Calzetti et al. 2000; Reddy et al. 2015, 2018a; Shivaei et al. 2020), converting to $E(B - V)_{\text{stars}}$ using a reddening law, and again assuming a relation between $E(B - V)_{\text{gas}}$ and $E(B - V)_{\text{stars}}$ (as in Onodera et al. 2016).

Here, we instead use a sample of ~ 300 MOSDEF star-forming galaxies at $z \sim 2.3$ with $H\alpha$ and $H\beta$ detections to calibrate a relation between SFR and continuum reddening inferred using SED fitting and $E(B - V)_{\text{gas}}$ based on the Balmer decrement, leveraging correlations among these properties (Reddy et al. 2015; Shivaei et al. 2020). The derivation of this calibration can be found in Appendix A, and the resulting relation is

$$E(B - V)_{\text{gas}} = E(B - V)_{\text{stars}} - 0.604 + 0.538 \times [\log(\text{SFR}(\text{SED})) - 0.20 \times (z - 2.3)]. \quad (1)$$

This method reliably recovers the Balmer decrement $E(B - V)_{\text{gas}}$ with a mean offset of 0.02 magnitudes and an intrinsic scatter of 0.23 magnitudes that shows no bias as a function of M_* or SFR and outperforms the other methods discussed above (see Appendix A).¹⁴

For targets without Balmer decrement measurements (i.e., $z \sim 2.3$ galaxies with undetected $H\beta$ and all $z \sim 3.3$ galaxies), we estimate $E(B - V)_{\text{gas}}$ using Equation (1). When estimated in this way, the uncertainty on $E(B - V)_{\text{gas}}$ includes the intrinsic calibration scatter. Results at $z \sim 2.3$ are indistinguishable within the uncertainties if we limit the sample to only galaxies with $H\alpha$ and $H\beta$ detections or use the new SED-based $E(B - V)_{\text{gas}}$ method for all galaxies (including those with measured Balmer decrements). Emission-line ratios are corrected for reddening using $E(B - V)_{\text{gas}}$ and assuming a Cardelli et al. (1989) Milky Way extinction law.

2.2.4. Star Formation Rates

SFRs are derived from dust-corrected Balmer emission-line luminosities ($H\alpha$ if available, otherwise $H\beta$) using the $H\alpha$

conversion of Hao et al. (2011), renormalized to a Chabrier (2003) IMF (Shivaei et al. 2015). When $H\beta$ is the only Balmer line detected, an intrinsic ratio of $H\alpha/H\beta = 2.86$ is assumed. SFRs at $z \sim 3.3$ are derived from $H\beta$, while $H\alpha$ is used at $z \sim 2.3$. Throughout this paper, SFRs are those derived from Balmer emission lines unless specifically noted otherwise.

2.3. Galaxy Samples

2.3.1. MOSDEF Samples at $z \sim 2.3$ and $z \sim 3.3$

We selected samples of star-forming galaxies (SFGs) at $z \sim 2.3$ and $z \sim 3.3$ from the MOSDEF survey. We required a robust spectroscopic redshift as measured from the MOSFIRE spectrum. Active galactic nuclei (AGNs) were identified by their X-ray and infrared properties (Coil et al. 2015; Azadi et al. 2017, 2018; Leung et al. 2019) and rejected, and we further removed galaxies with $\log([N\text{II}]/H\alpha) > -0.3$ that have a high probability of being dominated by AGN emission. We did not make any additional cuts based on position in the $[N\text{II}]$ BPT diagram because of the evolution of the star-forming sequence at $z \sim 2$ toward the Kauffmann et al. (2003) delineation between $z \sim 0$ SFGs and AGNs (e.g., Steidel et al. 2014; Shapley et al. 2015; Sanders et al. 2016; Strom et al. 2017). The total samples of MOSDEF star-forming galaxies number 523 at $2.09 \leq z \leq 2.61$ with a median stellar mass of $\log(M_*/M_\odot) = 9.97$ and $z_{\text{med}} = 2.29$; and 245 at $2.95 \leq z \leq 3.80$ with a median stellar mass of $\log(M_*/M_\odot) = 9.89$ and $z_{\text{med}} = 3.23$.

From these parent samples of MOSDEF SFGs, we selected a sample of individual galaxies with metallicity measurements and a sample from which we will produce composite spectra. The minimum requirement to obtain a metallicity estimate using our methodology is a detection of both $[O\text{II}]$ and $[O\text{III}]\lambda 5007$ (see Section 3 for details on metallicity calculations). We thus selected individual galaxies from the SFG parent samples by requiring that both $[O\text{II}]$ and $[O\text{III}]\lambda 5007$ are detected with $S/N \geq 3$, yielding individual metallicity samples of 265 and 130 galaxies at $z \sim 2.3$ and 3.3, respectively. Galaxies that additionally have detections of $H\beta$ (68% (66%) at $z \sim 2.3$ (3.3)) and $[\text{NeIII}]$ (20% (35%) at $z \sim 2.3$ (3.3)) will have more robust metallicity determinations. The individual metallicity sample at $z \sim 2.3$ (3.3) has a median stellar mass of $\log(M_*/M_\odot) = 9.85$ (9.66) and $z_{\text{med}} = 2.27$ (3.23), where the typical stellar masses are slightly lower than in the parent SFG samples because $[O\text{III}]$ is intrinsically weak at high M_* and $[O\text{II}]$ is increasingly affected by dust as M_* increases.

The redshift and stellar mass distributions are shown in the left and middle panels of Figure 1 for the MOSDEF SFG parent sample (gray) and the individual metallicity sample (black). The sample with sufficient emission-line detections for metallicity estimates displays a similar redshift and mass distribution to that of the full sample of MOSDEF SFGs at both $z \sim 2.3$ and $z \sim 3.3$. The selection of the stacking samples is described in Section 2.4 below.

2.3.2. Sample at $z \sim 0$

For a local comparison sample, we employ measurements from the composite spectra of $\sim 200,000$ Sloan Digital Sky Survey (SDSS; York et al. 2000) galaxies at $z \sim 0.08$ from AM13, binned both in stellar mass alone and in M_* and SFR. These stacked spectra have direct-method metallicity measurements from $[O\text{III}]\lambda 4363$ and $[O\text{II}]\lambda\lambda 7320, 7330$ at $\log(M_*/M_\odot) < 10.5$, and strong-line measurements over $7.5 < \log(M_*/M_\odot) < 11.5$.

¹⁴ Note that the calibration in Equation (1) is only applicable when $E(B - V)_{\text{stars}}$ and $\text{SFR}(\text{SED})$ have been derived under the same set of assumptions for SED fitting as described in Section 2.2.2, in particular assuming a Calzetti et al. (2000) attenuation law. In Appendix A, we provide an alternate form applicable when a Small Magellanic Cloud (SMC) extinction law (Gordon et al. 2003) is instead assumed.

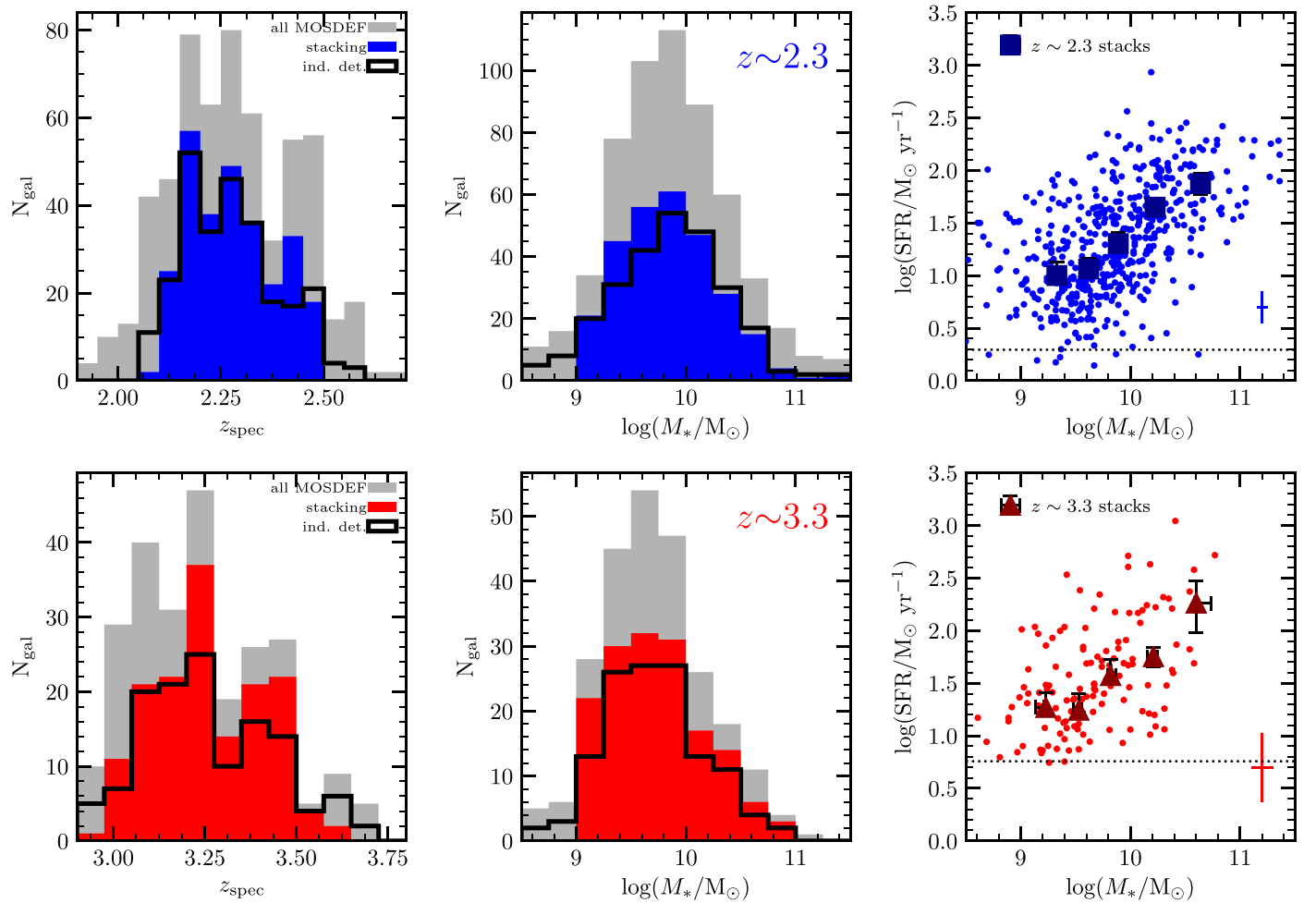


Figure 1. Redshift histogram (left), stellar mass distribution (middle), and SFR versus M_* for MOSDEF star-forming galaxies at $z \sim 2.3$ (top) and $z \sim 3.3$ (bottom). In the left and middle panels, the gray histogram represents all MOSDEF star-forming galaxies in each redshift bin, the black outline shows the subset of individual galaxies with metallicity measurements, and the filled color histogram (blue for $z \sim 2.3$, red for $z \sim 3.3$) denotes the stacking sample. In the right panel, individual galaxies are shown as colored dots, while values inferred from stacked spectra in stellar mass bins are presented as colored squares/triangles with error bars. The median uncertainty on M_* and SFR of the individual galaxies is displayed in the lower-right corner. The SFR corresponding to the MOSDEF 3σ detection limit of $\text{H}\alpha$ at $z \sim 2.3$ and $\text{H}\beta$ at $z \sim 3.3$ is shown by the dotted line in the top and bottom panels, respectively.

The stellar masses and SFRs of both the individual SDSS galaxies and AM13 stacks have been shifted to a Chabrier (2003) IMF, and the SFRs have also been renormalized to the Hao et al. (2011) $\text{H}\alpha$ calibration. SFR and M_* for stacked spectra are taken to be the median SFR and M_* of the individual galaxies in each bin.

Recent work has demonstrated the importance of accounting for contributions from diffuse ionized gas (DIG) to the total emission-line fluxes in integrated galaxy spectra at $z \sim 0$ (e.g., Sanders et al. 2017; Zhang et al. 2017; Vale Asari et al. 2019). Correcting for DIG contamination is particularly important for gas-phase metallicity studies because DIG emission enhances low-ionization lines in galaxy spectra, biasing metallicity estimates high. The AM13 stacks were corrected for DIG contamination following Sanders et al. (2017). Note that we have not corrected the $\text{H}\alpha$ -based SFRs for DIG, though this correction can significantly lower the SFR of low-sSFR ($M_*/\text{SFR} \lesssim 0.01 \text{ Gyr}^{-1}$) galaxies by a factor of ~ 2 – 3 (Vale Asari et al. 2019). High-redshift samples were not corrected for DIG because it is not expected to contribute significantly to their total line emission due to the high SFR surface densities (Σ_{SFR} ; Sanders et al. 2017; Shapley et al. 2019).

2.4. Composite Spectra

We created composite spectra in bins of stellar mass to measure sample averages in a way that includes galaxies for which not all lines of interest were detected. Stacking samples were selected from the MOSDEF SFG parent samples at $z \sim 2.3$ and $z \sim 3.3$ by further requiring detection of $[\text{O III}]\lambda 5007$ at $\text{S/N} \geq 3$ and spectral coverage of $[\text{O II}]$, $[\text{Ne III}]$, $\text{H}\beta$, and $[\text{O III}]\lambda 5007$ (the four strong lines with common coverage between $z \sim 2.3$ and $z \sim 3.3$). While not required for selection, the $z \sim 2.3$ stacks additionally have coverage of $\text{H}\alpha$, $[\text{N II}]$, and $[\text{S II}]$. We note that $[\text{Ne III}]$ is not required for a metallicity determination but provides an additional independent line ratio to improve abundance constraints. The stacking sample size increases by only 4% if $[\text{Ne III}]$ coverage is not required. A detection of $[\text{O III}]\lambda 5007$ is required in order to normalize the spectra prior to stacking to ensure that galaxies with the brightest lines (i.e., highest SFRs) do not dominate the stacks.¹⁵

¹⁵ Ideally, spectra would be normalized by a Balmer line instead because $[\text{O III}]$ flux is sensitive to both SFR and metallicity. This is not feasible because the strongest Balmer line accessible at $z \sim 3.3$ is $\text{H}\beta$, and requiring $\text{S/N} \geq 3$ for $\text{H}\beta$ reduces the $z \sim 3.3$ stacking sample size by 40%. However, we have checked that line ratios in the $z \sim 2.3$ stacks do not change significantly within the uncertainties when normalizing by $\text{H}\alpha$ instead of $[\text{O III}]$.

Table 1
Properties of Stacked Spectra in Bins of M_* for the $z \sim 2.3$ and $z \sim 3.3$ Samples

$\log \left(\frac{M_*}{M_\odot} \right)^a$	N^b	$\log \left(\frac{\text{SFR}}{M_\odot \text{ yr}^{-1}} \right)$	$\log \left(\frac{[\text{O III}]}{\text{H}\beta} \right)$	$\log \left(\frac{[\text{O II}]}{\text{H}\beta} \right)$	$\log (\text{O}_{32})$	$\log (\text{R}_{32})$	$\log \left(\frac{[\text{Ne III}]}{[\text{O II}]} \right)$	$\log \left(\frac{[\text{N II}]}{\text{H}\alpha} \right)$	$\log(\text{O3N2})$	$12 + \log \left(\frac{\text{O}}{\text{H}} \right)$
$z \sim 2.3$ Stacks in Bins of M_*										
$9.33^{+0.01}_{-0.05}$	65	$1.00^{+0.13}_{-0.01}$	$0.68^{+0.01}_{-0.04}$	$0.47^{+0.05}_{-0.03}$	$0.21^{+0.01}_{-0.08}$	$0.97^{+0.01}_{-0.03}$	$-0.79^{+0.05}_{-0.06}$	$-1.22^{+0.08}_{-0.05}$	$1.90^{+0.05}_{-0.12}$	$8.30^{+0.02}_{-0.02}$
$9.62^{+0.03}_{-0.01}$	65	$1.06^{+0.11}_{-0.05}$	$0.56^{+0.04}_{-0.01}$	$0.51^{+0.05}_{-0.03}$	$0.05^{+0.04}_{-0.04}$	$0.91^{+0.04}_{-0.02}$	$-0.95^{+0.09}_{-0.07}$	$-1.11^{+0.07}_{-0.06}$	$1.67^{+0.08}_{-0.08}$	$8.41^{+0.02}_{-0.02}$
$9.89^{+0.02}_{-0.02}$	65	$1.30^{+0.11}_{-0.03}$	$0.53^{+0.03}_{-0.04}$	$0.63^{+0.03}_{-0.04}$	$-0.11^{+0.04}_{-0.04}$	$0.95^{+0.02}_{-0.03}$	$-0.98^{+0.01}_{-0.16}$	$-0.93^{+0.04}_{-0.05}$	$1.46^{+0.06}_{-0.07}$	$8.48^{+0.02}_{-0.02}$
$10.23^{+0.02}_{-0.02}$	64	$1.65^{+0.05}_{-0.07}$	$0.39^{+0.03}_{-0.02}$	$0.64^{+0.01}_{-0.05}$	$-0.25^{+0.05}_{-0.02}$	$0.88^{+0.02}_{-0.04}$	$-1.19^{+0.13}_{-0.03}$	$-0.74^{+0.04}_{-0.03}$	$1.13^{+0.04}_{-0.05}$	$8.57^{+0.01}_{-0.01}$
$10.64^{+0.03}_{-0.06}$	21	$1.87^{+0.09}_{-0.10}$	$0.26^{+0.07}_{-0.06}$	$0.62^{+0.10}_{-0.06}$	$-0.36^{+0.10}_{-0.11}$	$0.82^{+0.07}_{-0.04}$	$-1.19^{+0.25}_{-0.23}$	$-0.63^{+0.08}_{-0.01}$	$0.89^{+0.06}_{-0.13}$	$8.64^{+0.03}_{-0.04}$
$z \sim 3.3$ Stacks in Bins of M_*										
$9.23^{+0.02}_{-0.09}$	37	$1.27^{+0.14}_{-0.06}$	$0.74^{+0.05}_{-0.04}$	$0.29^{+0.11}_{-0.10}$	$0.45^{+0.06}_{-0.10}$	$0.97^{+0.04}_{-0.02}$	$-0.66^{+0.05}_{-0.17}$	$8.19^{+0.03}_{-0.04}$
$9.52^{+0.02}_{-0.05}$	37	$1.24^{+0.16}_{-0.02}$	$0.69^{+0.06}_{-0.02}$	$0.44^{+0.08}_{-0.05}$	$0.25^{+0.06}_{-0.05}$	$0.97^{+0.06}_{-0.03}$	$-0.82^{+0.05}_{-0.15}$	$8.29^{+0.03}_{-0.02}$
$9.82^{+0.05}_{-0.03}$	36	$1.57^{+0.15}_{-0.08}$	$0.65^{+0.03}_{-0.07}$	$0.50^{+0.07}_{-0.05}$	$0.15^{+0.03}_{-0.09}$	$0.96^{+0.03}_{-0.05}$	$-0.92^{+0.09}_{-0.11}$	$8.35^{+0.03}_{-0.02}$
$10.21^{+0.04}_{-0.05}$	36	$1.75^{+0.09}_{-0.03}$	$0.53^{+0.07}_{-0.03}$	$0.65^{+0.07}_{-0.05}$	$-0.13^{+0.09}_{-0.03}$	$0.95^{+0.05}_{-0.05}$	$-1.01^{+0.09}_{-0.10}$	$8.48^{+0.02}_{-0.02}$
$10.60^{+0.13}_{-0.01}$	9	$2.26^{+0.21}_{-0.28}$	$0.35^{+0.20}_{-0.14}$	$0.62^{+0.30}_{-0.16}$	$-0.27^{+0.13}_{-0.17}$	$0.87^{+0.25}_{-0.11}$	$-0.87^{+0.21}_{-0.20}$	$8.54^{+0.03}_{-0.06}$

Notes.

^a Median stellar mass of galaxies in each bin.

^b Number of galaxies in each bin.

This requirement does not significantly bias the stacking sample because [O III] λ 5007 is one of the brightest lines in high-redshift galaxy spectra (i.e., almost always detected if a MOSDEF redshift was measured). We additionally removed objects for which one of the lines of interest is close enough to the edge of the bandpass that the continuum is not sufficiently sampled on both sides of the line centroid and targets with double-peaked or otherwise significantly non-Gaussian line profiles. This selection results in a $z \sim 2.3$ (3.3) stacking sample of 280 (155) star-forming galaxies with $z_{\text{med}} = 2.28$ (3.24) and median stellar mass of $\log(M_*/M_\odot) = 9.96$ (9.89).

We divided the stacking samples into four bins of stellar mass. The MOSDEF survey has a high spectroscopic success rate ($\sim 85\%$) at $9.0 \leq \log(M_*/M_\odot) \leq 10.5$ (Kriek et al. 2015), signifying that the MOSDEF sample is highly complete and representative of the typical galaxy population over this mass range given the rest-optical magnitude-limited nature of the parent sample. Below $\log(M_*/M_\odot) = 9.0$, both the number of targets and spectroscopic success rate drop off sharply as these low-mass galaxies are fainter than the H -band magnitude cut. At $\log(M_*/M_\odot) > 10.5$, targeted galaxies are fewer because of the rarity of such massive systems in the volume probed, but the spectroscopic success rate also drops to $\sim 60\%$. As discussed in Kriek et al. (2015), this lower success rate is at least partially caused by a significantly lower success rate for red star-forming galaxies, potentially leading to a bias against metal-rich systems at high masses.

For these reasons, we divided galaxies into four bins in M_* over the range $9.0 \leq \log(M_*/M_\odot) \leq 10.5$, separated such that an approximately equal number of galaxies falls in each bin. We created a fifth high-mass bin that contains all galaxies at $\log(M_*/M_\odot) > 10.5$. The number of galaxies in each bin are given in Table 1. We consider the four bins at $10^{9.0} - 10^{10.5} M_\odot$ to be the “core” stacking sample where MOSDEF is highly complete and representative, and focus our analysis on stacks in this mass range. We also show and discuss the high-mass ($M_* > 10^{10.5} M_\odot$) stacks, but acknowledge the potential bias against high-metallicity systems in this regime.

The composite spectra were created following the methods outlined in Sanders et al. (2018). Briefly, the individual spectra

were shifted into the rest-frame and luminosity density units using the spectroscopic redshift, dust-corrected according to their $E(B - V)_{\text{gas}}$ assuming a Cardelli et al. (1989) extinction curve (where we use $E(B - V)_{\text{gas}}$ from the Balmer decrement when available, otherwise $E(B - V)_{\text{gas}}$ from Equation (1)), normalized by the dust-corrected [O III] λ 5007 luminosity, and resampled onto a uniform wavelength grid. Individual spectra were then combined by taking the median at each wavelength element¹⁶ and multiplied by the median [O III] λ 5007 luminosity. Emission-line luminosities were measured from the stacked spectra using the same method as for the individual galaxies. Balmer absorption corrections were estimated from the median correction applied to the individual galaxies in each bin.

Uncertainties on the line luminosities and line ratios were estimated using a Monte Carlo method in which we bootstrap resampled the galaxies in the stacking sample, perturbed the masses, $E(B - V)_{\text{gas}}$, and science spectra according to their uncertainties, repopulated the mass bins using the original boundaries in M_* , stacked the perturbed spectra according to the method described above, and remeasured the line luminosities and line ratios. The uncertainties on each property measured from the stacks are inferred from the 68th percentile width of the distribution resulting from 100 realizations. In this way, errors on properties measured from the stacks include measurement errors and sample variance. Using random subsets of a sample of galaxies with detections of [O II], [Ne III], H β , and [O III], we have verified that this stacking method reproduces the median line ratios of the input samples to better than 0.05 dex. Table 1 presents the M_* , SFR, and line ratios of the $z \sim 2.3$ and $z \sim 3.3$ stacked spectra.

2.5. Representativeness of Samples

A sample that is biased in SFR relative to the mean SFR- M_* relation will yield a biased MZR because of the existence of the FMR at both $z \sim 0$ and $z > 1$ (Mannucci et al. 2010;

¹⁶ We do not apply any weighting when combining the spectra. Note that inverse-variance weighting, while maximizing S/N, gives higher weight in the emission lines to high-SFR objects and thus potentially biases results from stacks.

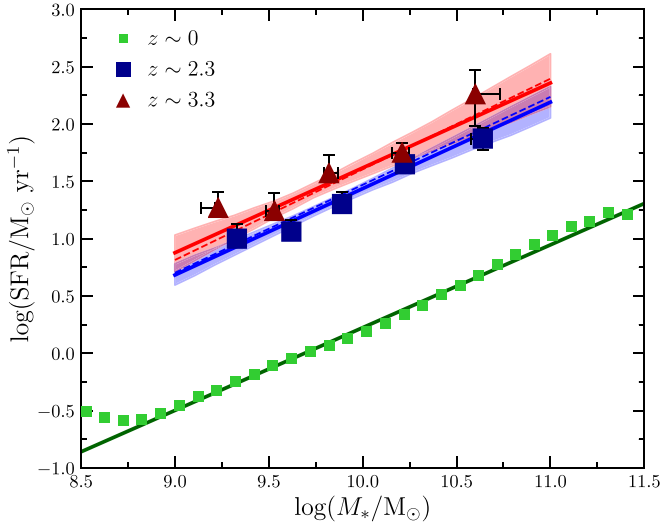


Figure 2. SFR– M_* relation at $z \sim 0$ (green), $z \sim 2.3$ (blue), and $z \sim 3.3$ (red). Squares denote values for stacked spectra in bins of stellar mass. Solid lines show the best-fit power-law relations to the stacks, color-coded by redshift. The shaded regions display the 1σ uncertainty intervals around the best-fit lines for $z \sim 2.3$ and $z \sim 3.3$. SFR– M_* relations from the parameterization of Speagle et al. (2014) at $z = 2.3$ and $z = 3.3$ are given by the dashed lines, displaying excellent agreement with our best-fit relations.

Sanders et al. 2018). At fixed M_* , if a sample has a higher than average SFR, then O/H will be lower than average, and vice versa. It is therefore imperative that samples have an SFR distribution that is representative at each stellar mass, i.e., that they lie on the “star-forming main sequence” at each redshift.

The right panels of Figure 1 display SFR versus M_* for stacked spectra and individual galaxies with $S/N \geq 3$ in at least one Balmer line at $z \sim 2.3$ (top) and $z \sim 3.3$ (bottom). A clear correlation is present among individual galaxies and stacks. The dotted lines display the SFR corresponding to the $H\alpha$ and $H\beta$ 3σ detection threshold of MOSDEF at $z \sim 2.3$ and $z \sim 3.3$, respectively. At $\log(M_*/M_\odot) > 9.5$, the distribution of individual galaxies lies above this threshold at both redshifts. Below $\log(M_*/M_\odot) = 9.5$, individual galaxies begin to fall below the Balmer line detection limit. Stacking is meant to include galaxies falling below the detection threshold. The lowest-mass bin at $z \sim 3.3$ has a slightly higher SFR than the next bin higher in mass, and at $z \sim 2.3$, the relation displays a slight flattening at the low-mass end (though not highly significant relative to the uncertainties). Assuming that the star-forming main sequence is a monotonically increasing power law, these data indicate that the $z \sim 2.3$ and $z \sim 3.3$ stacking samples are missing the lowest-SFR galaxies at $\log(M_*/M_\odot) < 9.5$ despite not requiring $H\beta$ detections, biasing the SFR high in this lowest-mass bin (see also Shivaie et al. 2015).

Figure 2 shows SFR versus M_* for the $z \sim 0$, $z \sim 2.3$, and $z \sim 3.3$ samples, with only stacks displayed at high redshifts. Visually, the relation between SFR and M_* displays a similar slope at all redshifts, with the SFR at fixed M_* increasing as a function of redshift. The $z \sim 0$ sample is biased high in SFR below $\log(M_*/M_\odot) = 8.7$, where SFR begins increasing with decreasing M_* . This bias is likely due to the emission-line selection and the depth of SDSS spectroscopy. According to the FMR, if a sample is increasingly biased in SFR with decreasing M_* , the measured slope of the MZR will be artificially steepened. This SFR bias likely explains the very steep low-mass slope of $O/H \propto M_*^{0.64}$ obtained by AM13. We only use the AM13

stacks with $\log(M_*/M_\odot) > 8.7$ in our analysis to avoid biasing the low-mass slope.

We fit a power-law of the form $SFR = C \times M_*^\beta$ to the stacks at each redshift. For the MOSDEF stacks, we exclude the highest-mass bin from the fitting due to potential bias (Section 2.4). At $z \sim 3.3$, we also exclude the lowest-mass bin that is clearly biased high in SFR. We retain the lowest-mass $z \sim 2.3$ bin because the apparent flattening is only significant at the 1σ level, but note that our results do not significantly change if this bin is also excluded from fitting. We find the following best-fit relations, displayed as solid lines in Figure 2:

$$z \sim 0: \log\left(\frac{SFR}{M_\odot \text{ yr}^{-1}}\right) = (0.72 \pm 0.01) \times m_{10} + (0.22 \pm 0.01) \quad (2)$$

$$z \sim 2.3: \log\left(\frac{SFR}{M_\odot \text{ yr}^{-1}}\right) = (0.75 \pm 0.12) \times m_{10} + (1.44 \pm 0.04) \quad (3)$$

$$z \sim 3.3: \log\left(\frac{SFR}{M_\odot \text{ yr}^{-1}}\right) = (0.74 \pm 0.20) \times m_{10} + (1.62 \pm 0.06) \quad (4)$$

where $m_{10} = \log(M_*/10^{10} M_\odot)$. The slopes of the $z > 2$ SFR– M_* relations are consistent with the results of Shivaie et al. (2015) based on early MOSDEF data at $z = 1.4$ – 2.6 .

The parameterized $SFR(M_*, z)$ of Speagle et al. (2014) at $z = 2.3$ and $z = 3.3$ is displayed in Figure 2 as dotted lines, color-coded by redshift. Our best-fit SFR– M_* relations at $z = 2.3$ and $z = 3.3$ closely match those of Speagle et al. (2014), indicating that the MOSDEF samples are representative of typical galaxies falling on the star-forming main sequence. The lowest-mass $z \sim 3.3$ stack is elevated 0.2 dex in SFR above our best-fit $z \sim 3.3$ SFR– M_* relation and that of Speagle et al. (2014). At fixed M_* , the SFR-dependence of O/H has been found to be $\Delta \log(O/H) \sim -0.15 \times \Delta \log(SFR)$ for star-forming galaxies at $z \sim 2.3$ (Sanders et al. 2018). Accordingly, the SFR bias of the lowest-mass $z \sim 3.3$ bin is expected to result in a bias of ~ 0.03 dex in O/H. The magnitude of this bias is less than the formal uncertainty in metallicity for this stack (0.04 dex). We therefore retain the lowest-mass $z \sim 3.3$ stack in our analysis of the MZR. The highest-mass stacks are fully consistent with the best-fit relations and the Speagle et al. (2014) parameterization. We conclude that the MOSDEF sample does not display any large SFR biases over $10^{9.0}$ – $10^{10.75} M_\odot$ that would significantly affect the MZR derived from these data.

3. Metallicity Derivations

The choice of metallicity calibrations is of critical importance to any metallicity scaling relation analysis. As demonstrated by Kewley & Ellison (2008), the functional form and normalization of the local MZR vary significantly based on the metallicity indicator and calibration employed, such that comparing metallicities inferred from different indicators and calibrations can introduce severe biases. In addition, the excitation properties of high-redshift star-forming galaxies suggest that metallicity calibrations evolve with redshift due to changes in the underlying physical properties of the ionized gas in H II regions (e.g., Kewley et al. 2013; Steidel et al. 2014; Shapley et al. 2015, 2019; Sanders et al. 2016, 2020a, 2020b;

Kashino et al. 2017, 2019; Strom et al. 2017, 2018). Accordingly, applying calibrations constructed for the local universe may yield biased metallicities at high redshifts and consequently bias the inferred metallicity evolution.

In this analysis, we address these issues by (1) using a uniform set of strong emission lines for samples at all redshifts and (2) employing different metallicity calibrations at $z \sim 0$ and $z > 1$, all of which are empirically calibrated to direct-method metallicities, to reflect evolving ISM conditions. At all redshifts, metallicities are estimated using line ratios of [O II], H β , [O III], and [Ne III]. This choice of emission lines is partly driven by observational limitations because these are the only strong optical emission lines that can be observed at $z > 3$ with current facilities. However, there is an advantage to using these particular lines. This set of lines only contains α -element metal species (O, Ne) that have the same production channel through core-collapse SNe and are thus more direct tracers of the gas-phase oxygen abundance than nitrogen-based metallicity indicators ([N II]/H α , [O III]/[N II]) that are sensitive to N/O and the secondary production of N.

Our analysis at $z \sim 0$ uses the composite spectra of AM13. These composites have direct-method metallicities at $\log(M_*/M_\odot) < 10.5$, but this direct-method subset does not fully sample the high-mass asymptotic metallicity region, requiring coverage up to $\log(M_*/M_\odot) \sim 11.0$. In order to cover the full AM13 mass range up to $\log(M_*/M_\odot) \sim 11.5$, we fit relations between strong-line ratios and O/H using AM13 M_* -binned stacks at $8.7 < \log(M_*/M_\odot) < 10.5$ that have direct-method metallicities, spanning $8.4 < 12 + \log(\text{O}/\text{H}) < 8.8$. While this O/H range is sufficient for establishing the $z \sim 0$ MZR over $8.7 < \log(M_*/M_\odot) < 11.5$, we need to extend to lower metallicities to cover low-mass, high-SFR galaxies in the FMR. For this purpose, we supplement the AM13 stacks with the Berg et al. (2012) “combined select” sample of dwarf galaxies from the Spitzer Local Volume Legacy survey. This sample comprises 38 galaxies falling on the star-forming main sequence, with $6.0 \lesssim \log(M_*/M_\odot) \lesssim 9.0$ and direct-method metallicities extending down to $12 + \log(\text{O}/\text{H}) = 7.5$. The dwarf galaxy sample is based on slit spectra of H II regions and thus does not require DIG correction. We calculate the median line ratios and O/H of the Berg et al. (2012) dwarfs in four bins of O/H such that each bin contains an approximately equal number of galaxies and use these binned data for fitting. Direct-method metallicities for both the AM13 and Berg et al. (2012) samples have been uniformly recalculated using PyNeb (Luridiana et al. 2015) with the default set of atomic data.

We fit the line ratios [O III] λ 5007/H β , [O II] $\lambda\lambda$ 3726,3729/H β , $\text{O}_{32} = [\text{O III}]\lambda$ 5007/[O II] $\lambda\lambda$ 3726,3729, $\text{R}_{23} = ([\text{O III}]\lambda\lambda$ 4959,5007 + [O II] $\lambda\lambda$ 3726,3729)/H β , [Ne III] λ 3869/[O II] $\lambda\lambda$ 3726,3729, [N II] λ 6584/H α , and $\text{O3N2} = ([\text{O III}]\lambda$ 5007/H β)/([N II] λ 6584/H α) as a function of O/H. Figure 3 shows the results of fitting the AM13 and binned Berg et al. (2012) samples with cubic functions of the form

$$\log(R) = c_0 + c_1x + c_2x^2 + c_3x^3, \quad (5)$$

where $x = 12 + \log(\text{O}/\text{H}) - 8.69 = \log(Z_{\text{neb}}/Z_\odot)$. Separate fits are carried out using the DIG-corrected AM13 stacks (green) and the uncorrected stacks (gray), where the proper set of calibrations is used for each case. We do not fit [Ne III]/[O II] for the DIG-corrected stacks because the impact of DIG on [Ne III] was not characterized in Sanders et al. (2017). The

best-fit coefficients are given in Table 2, and these calibrations are used for the $z \sim 0$ samples.

For the high-redshift samples, we employ the metallicity calibrations of B18¹⁷ based on local analogs of $z \sim 2$ galaxies. B18 measured direct-method metallicities of stacked spectra for a sample of SDSS galaxies selected to lie on the $z \sim 2$ star-forming galaxy sequence in the [N II] BPT diagram. Sanders et al. (2020b) found that a sample of 18 galaxies at $z \sim 2.2$ with direct-method metallicities matches the B18 high-redshift analog calibrations on average for [O III]/H β , [O II]/H β , O_{32} , R_{23} , and [Ne III]/[O II] (displayed as the black diamond in Figure 3). Note that [N II] was not covered for the majority of the $z \sim 2.2$ direct-method sample, thus Sanders et al. (2020b) were unable to test [N II]/H α and O3N2 calibrations. This comparison suggests that the B18 oxygen- and neon-based calibrations are appropriate to apply to $z > 1$ galaxy samples.

The B18 $z \sim 2$ analog calibrations typically have higher O/H at a fixed line ratio relative to the DIG-corrected $z \sim 0$ calibrations. Until the number of high-redshift galaxies with direct-method measurements is large enough to independently produce calibrations, we must rely on local analogs for which sufficiently deep spectra are more easily obtained. We note that the B18 calibration sample spans $7.8 < 12 + \log(\text{O}/\text{H}) < 8.4$, such that we must extrapolate to cover the high-mass galaxies in the MOSDEF sample (the highest-mass $z \sim 2.3$ stack has $12 + \log(\text{O}/\text{H}) \approx 8.6$). Despite the uncertainty associated with extrapolating, we consider this approach to be more robust than applying $z \sim 0$ calibrations to $z > 1$ samples. The identification of local analogs at higher metallicities should be pursued to extend these calibrations.

For comparison, we also show the calibrations of M08 (red) and C17 in Figure 3. These calibration sets are commonly employed in MZR and FMR studies at low and high redshifts (e.g., Mannucci et al. 2009, 2010; Yates et al. 2012; Troncoso et al. 2014; Onodera et al. 2016; Suzuki et al. 2017; Curti et al. 2020a, 2020b). While displaying general agreement with our new $z \sim 0$ calibrations at high metallicity ($12 + \log(\text{O}/\text{H}) \gtrsim 8.3$), the M08 and C17 calibrations diverge from our $z \sim 0$ relations at lower O/H while more closely matching the B18 calibrations. As discussed in Sanders et al. (2020b), both M08 and C17 calibration samples are composed entirely of individual SDSS galaxies with [O III] λ 4363 detections at $12 + \log(\text{O}/\text{H}) \lesssim 8.3$. Requiring detections of this weak auroral line selects a sample that is strongly biased toward high excitation, sSFR, and emission-line equivalent width. That M08 and C17 are similar to B18 at $12 + \log(\text{O}/\text{H}) \sim 8.0$ implies that these extreme $z \sim 0$ galaxies have ISM properties similar to $z \sim 2$ galaxies and are thus not suitable for constructing calibrations generally applicable in the local universe.

Patrício et al. (2018) also tested strong-line calibrations for use at high redshift using a sample of $z > 1$ galaxies with direct-method metallicities that significantly overlap with those of Sanders et al. (2020b). These authors found that, of the

¹⁷ Note that the calibration reported in B18 for [O III] λ 5007/H β in fact uses the line ratio [O III] $\lambda\lambda$ 4959,5007/H β (i.e., the sum of the two [O III] lines at 4959 and 5007 Å.; F. Bian 2021, private communication). One should either use the correct [O III] $\lambda\lambda$ 4959,5007/H β line ratio with the calibration coefficients given in B18 or else decrease the y-intercept of their Equation (17) by $\log(3.98/2.98) = 0.126$ dex if using [O III] λ 5007/H β because [O III] λ 5007/ λ 4959 = 2.98 (Storey & Zeppen 2000). We have adopted the latter correction in both Sanders et al. (2020b) and this work.

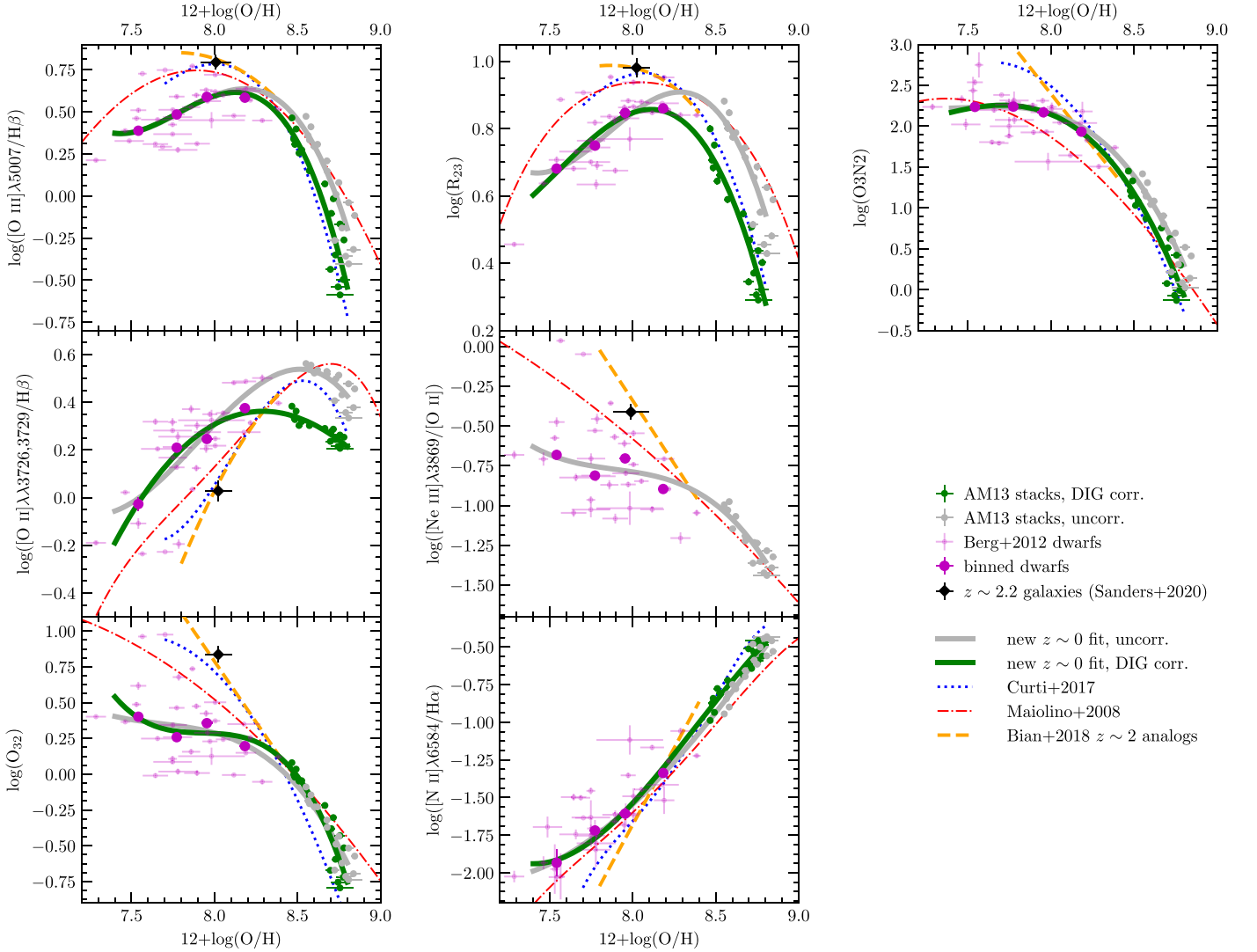


Figure 3. Calibrations between emission-line ratios and direct-method metallicity. The calibrations used at $z \sim 0$ are fit to the AM13 M_* -binned stacks of $z \sim 0$ galaxies at high metallicities (green points, corrected for DIG) and representative dwarf galaxies from Berg et al. (2012) at low metallicities (pink points). The solid green lines show the best-fit $z \sim 0$ calibrations. The gray points and solid gray lines show the form of the calibrations when the $z \sim 0$ data are not corrected for DIG emission. Best-fit coefficients are given in Table 2. Blue dotted and red dashed-dotted lines display the $z \sim 0$ calibrations of Curti et al. (2017) and Maiolino et al. (2008), respectively. The orange dashed lines denote the high-redshift analog calibrations of Bian et al. (2018, B18 hereafter) that are used to derive metallicities for the high-redshift samples. Each calibration is plotted over the range of metallicity of the empirical calibration sample. The black point shows the median values of a sample of 18 galaxies at $z \sim 2.2$ with direct-method metallicities from Sanders et al. (2020b), displaying close agreement with the high-redshift analog calibrations.

empirical strong-line calibrations they tested (M08; C17; B18; Jones et al. 2015), all performed reasonably well, with none performing better than the others. Even though all four are calibrated to $z \sim 0$ samples, these calibration sets are based on highly biased local galaxies in the metallicity range probed by the $z > 1$ sample ($12 + \log(\text{O}/\text{H}) \sim 7.7 - 8.3$), as described above (Jones et al. 2015 is also based on $[\text{O III}]\lambda 4363$ -detected galaxies in SDSS). Thus, the results of Patrício et al. (2018) agree with our conclusion that the M08, C17, and B18 calibrations appear to be more appropriate for applications at high redshifts than for typical $z \sim 0$ galaxies in the low-metallicity regime. No strong-line calibrations have been tested at $z > 1$ at higher metallicities ($12 + \log(\text{O}/\text{H}) > 8.3$), thus it is unknown which calibrations perform best for metal-rich high-redshift galaxies. Extending the dynamic range of the direct-method $z > 1$ sample may be possible by detecting the low-ionization auroral line $[\text{O II}]\lambda\lambda 7320, 7330$ that is expected to be stronger than $[\text{O III}]\lambda 4363$ at moderately high metallicities.

Because emission-line ratios are closely tied to ISM physical conditions, a crucial requirement of any set of metallicity calibrations is that the excitation sequences in line ratio versus line ratio diagrams of the calibrations match the sequences of the observed sample. In Figure 4, we show $[\text{O III}]/\text{H}\beta$ versus $[\text{N II}]/\text{H}\alpha$ (left; $[\text{N II}]$ BPT), O_{32} (middle), and $[\text{Ne III}]/[\text{O II}]$ (right). In addition to the stacks of MOSDEF $z \sim 2.3$ and $z \sim 3.3$ galaxies, we show the line ratios calculated from the new $z \sim 0$, B18 high-redshift analog, C17, and M08 calibrations over the metallicity range $12 + \log(\text{O}/\text{H}) = 8.0 - 8.7$. In each diagram, the B18 high-redshift analog calibrations match the excitation sequences of the high-redshift samples more closely than any of the $z \sim 0$ calibrations. It is not a perfect match, however. While the B18 calibrations show excellent agreement in $[\text{O III}]/\text{H}\beta$ versus $[\text{Ne III}]/[\text{O II}]$, they predict 0.1 dex higher O_{32} and 0.15 dex higher $[\text{N II}]/\text{H}\alpha$ at fixed $[\text{O III}]/\text{H}\beta$ than the high-redshift stacks on average. The offset between the B18 calibrations and MOSDEF stacks in the $[\text{N II}]$

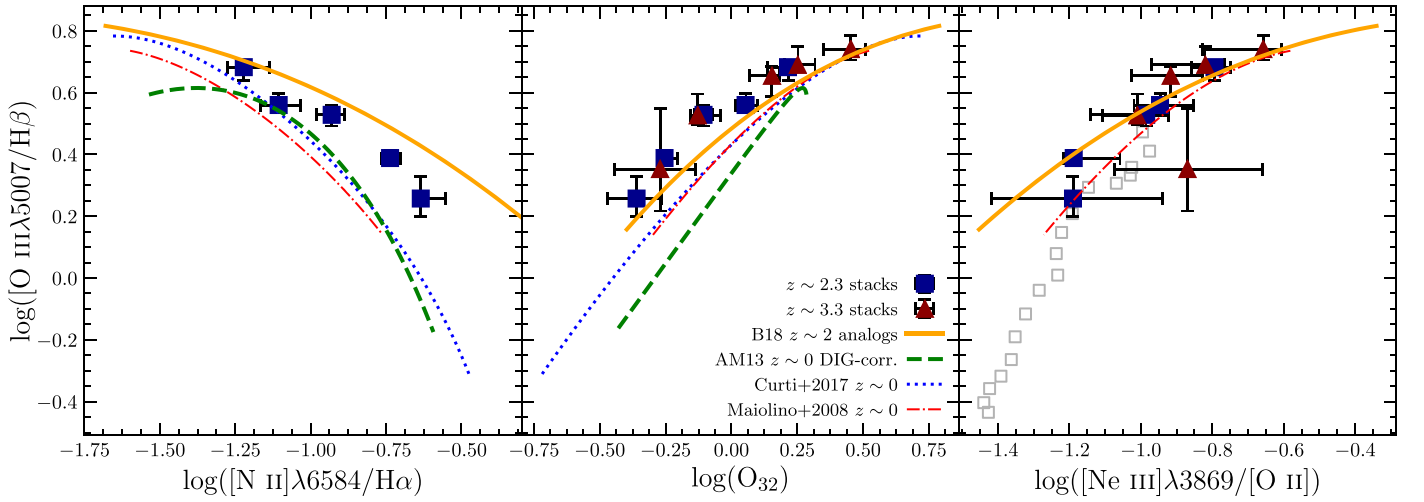


Figure 4. Excitation diagrams of $[\text{O III}]\lambda 5007/\text{H}\beta$ versus $[\text{N II}]\lambda 6584/\text{H}\alpha$ ($[\text{N II}]$ BPT, left), O_{32} (middle), and $[\text{Ne III}]\lambda 3869/[\text{O II}]\lambda\lambda 3726,3729$ (right). Stacked spectra of $z \sim 2.3$ and $z \sim 3.3$ galaxies (dark blue and red, respectively) are compared to the excitation sequences of strong-line calibrations evaluated over $12 + \log(\text{O}/\text{H}) = 8.0\text{--}8.7$. The new DIG-corrected $z \sim 0$ calibrations of this work are shown as green dashed lines. The $z = 0$ calibrations of Maiolino et al. (2008) and Curti et al. (2017) are presented in red dashed-dotted and blue dotted lines, respectively. The B18 high-redshift analog calibrations are shown in solid orange, providing the closest match to the high-redshift stacks. The new $z \sim 0$ calibrations are not shown in the $[\text{Ne III}]/[\text{O II}]$ diagram because DIG corrections for $[\text{Ne III}]$ were not calibrated in Sanders et al. (2017). We instead display the uncorrected $z \sim 0$ AM13 stacks as gray squares. DIG emission is expected to affect $[\text{O II}]$ more strongly than $[\text{Ne III}]$ such that the DIG-corrected $[\text{Ne III}]/[\text{O II}]$ ratios should be larger at fixed O/H .

BPT diagram is a result of the B18 selection, requiring galaxies to fall within 0.1 dex of the $[\text{N II}]$ BPT sequence defined by the $z \sim 2.3$ Keck Baryonic Structure Survey (KBSS) sample (Steidel et al. 2014) that is known to have a larger offset from the $z \sim 0$ sequence than $z \sim 2.3$ MOSDEF galaxies (Shapley et al. 2015). Until strong-line metallicity diagnostics directly calibrated to $z \sim 2$ samples are available, it is worthwhile to refine methods of selecting local analogs that more closely match high-redshift galaxy properties. In the meantime, we find that the B18 high-redshift calibrations provide a reasonable match to the $z > 2$ data in all three panels. We note that the B18 high-redshift calibrations provide a better match to the $z > 2$ samples than all of the $z \sim 0$ calibrations in the middle panel of Figure 4 displaying $[\text{O III}]/\text{H}\beta$ versus O_{32} . Because the metallicities in this work are derived primarily from these two line ratios (see below), this agreement strongly suggests that the B18 calibrations are the most appropriate for our high-redshift samples.

Metallicities are calculated via a χ^2 minimization over multiple line ratios simultaneously. The best-fit metallicity is that which minimizes the expression

$$\chi^2 = \sum_i \frac{(R_{\text{obs},i} - R_{\text{cal},i}(x))^2}{(\sigma_{\text{obs},i}^2 + \sigma_{\text{cal},i}^2)}, \quad (6)$$

where the sum over i denotes the set of line ratios used, $R_{\text{obs},i}$ is the logarithm of the i th observed line ratio, $R_{\text{cal},i}(x)$ is the logarithmic i th line ratio of the calibration at $x = 12 + \log(\text{O}/\text{H})$, $\sigma_{\text{obs},i}$ is the uncertainty in the i th observed line ratio, and $\sigma_{\text{cal},i}$ is the uncertainty in i th line ratio at fixed O/H of the calibration. Because our calibrations at both $z \sim 0$ and $z > 1$ are fit to stacked spectra, we cannot evaluate σ_{cal} directly. We instead take σ_{cal} to be the average of the values reported for calibrations by M08, C17, and Jones et al. (2015), noting that these three works find similar scatter for each line ratio. Our adopted values of σ_{cal} are given in Table 2. When fitting stacks, σ_{cal} is divided by \sqrt{N} , where N is the number of galaxies in the stack. Uncertainties on metallicity are estimated by perturbing

Table 2
Best-fit Calibrations between Strong-line Ratios and Direct-method Metallicities (Figure 3)

Line Ratio (R)	c_0	c_1	c_2	c_3
DIG-corrected $z \sim 0$ Data				
$[\text{O III}]\lambda 5007/\text{H}\beta$	-0.143	-3.16	-4.06	-1.49
$[\text{O II}]\lambda 3727/\text{H}\beta$	0.270	-0.452	-0.520	0.0831
O_{32}	-0.413	-2.70	-3.52	-1.55
R_{23}	0.469	-1.51	-1.75	-0.508
$[\text{N II}]\lambda 6584/\text{H}\alpha$	-0.606	1.28	-0.435	-0.485
O3N2	0.461	-4.40	-3.37	-0.761
Uncorrected $z \sim 0$ Data				
$[\text{O III}]\lambda 5007/\text{H}\beta$	0.111	-2.39	-3.30	-1.24
$[\text{O II}]\lambda 3727/\text{H}\beta$	0.498	-0.479	-1.55	-0.654
O_{32}	-0.388	-1.91	-1.74	-0.570
R_{23}	0.698	-1.17	-1.90	-0.758
$[\text{Ne III}]\lambda 3869/[\text{O II}]\lambda 3727$	-1.19	-1.29	-1.44	-0.601
$[\text{N II}]\lambda 6584/\text{H}\alpha$	-0.663	1.47	0.215	-0.102
O3N2	0.772	-3.86	-3.33	-0.939
Ratio	$\frac{[\text{O III}]}{\text{H}\beta}$	$\frac{[\text{O II}]}{\text{H}\beta}$	O_{32}	R_{23}
σ_{cal}^a	0.10	0.13	0.19	0.08
Ratio	$\frac{[\text{Ne III}]}{[\text{O II}]}$	$\frac{[\text{N II}]}{\text{H}\alpha}$	O3N2	
σ_{cal}^a	0.20	0.15	0.16	

Notes. Coefficients are given for the cubic function of Equation (5).

^a Adopted logarithmic scatter in line ratio at fixed O/H .

the observed line ratios by their uncertainties and refitting 200 times, where the 1σ uncertainty is derived from the 68th percentile width of the resulting distribution.

As explained above, we only utilize line ratios of $[\text{O II}]$, $\text{H}\beta$, $[\text{O III}]$, and $[\text{Ne III}]$ to derive metallicities at all redshifts. This set of emission lines allows for three independent line ratios for fitting. Here, we use O_{32} , $[\text{O III}]/\text{H}\beta$, and $[\text{Ne III}]/[\text{O II}]$. This set of line ratios is advantageous because it minimizes the

number of line ratios that require dust correction. We obtain similar results if we use different sets of independent ratios within the chosen set of emission lines (i.e., when using $[\text{O II}]/\text{H}\beta$ or R_{23} instead of $[\text{O III}]/\text{H}\beta$ or O_{32}). Because the calibrations between O_{32} and O/H are monotonic, the minimum requirement to calculate metallicity is a detection of $[\text{O III}]$ and $[\text{O II}]$, while adding $\text{H}\beta$ and $[\text{Ne III}]$ when available reduces uncertainties and improves the estimate.

Metallicities are determined for MOSDEF galaxies and stacked MOSDEF spectra using the B18 high-redshift analog calibrations. We note that the stacked spectra have all four lines detected in every mass bin, thus three line ratios are used to infer metallicities for all high-redshift stacks. For the $z \sim 0$ samples, we use the new calibrations fit to the AM13 M_* -binned stacks and given in Table 2. Because DIG corrections have not been calculated for $[\text{Ne III}]$, we do not use $[\text{Ne III}]/[\text{O II}]$ to derive metallicities for the AM13 stacks, basing the metallicities on O_{32} and $[\text{O III}]/\text{H}\beta$ only.

4. Results

4.1. Trends between Line Ratios and Stellar Mass

We first investigate empirical trends between optical emission-line ratios and M_* . Figure 5 presents $[\text{O III}]/\text{H}\beta$, O_{32} , R_{23} , and $[\text{Ne III}]/[\text{O II}]$ versus M_* for the MOSDEF $z \sim 2.3$ (left) and $z \sim 3.3$ (right) samples and composite spectra. At both $z \sim 2.3$ and $z \sim 3.3$, we find that all four line ratios decrease with increasing M_* , although R_{23} is relatively flat over most of the mass range covered by these samples. These trends are consistent with increasing metallicity as M_* increases, with most galaxies lying on the higher-metallicity “upper branch” of $[\text{O III}]/\text{H}\beta$ and R_{23} that are double-valued with O/H . R_{23} is known to saturate at metallicities of $7.8 \lesssim 12 + \log(\text{O}/\text{H}) \lesssim 8.5$ (Figure 3; see also, e.g., Kewley & Dopita 2002; Tremonti et al. 2004; Maiolino et al. 2008). Thus, the flatness of R_{23} (especially at $z \sim 3.3$) suggests that much of our sample falls in this metallicity regime. Trends are similar for individual galaxies and stacked spectra, although individual galaxies with $[\text{Ne III}]$ detections fall almost entirely above the stacks in $[\text{Ne III}]/[\text{O II}]$ because of the faintness of this line and the associated selection effects.

In Figure 6, we show the same four line ratios as a function of M_* for samples at $z \sim 0$, $z \sim 2.3$, and $z \sim 3.3$ (only composites are displayed for the high-redshift samples). The trends of decreasing $[\text{O III}]/\text{H}\beta$, O_{32} , R_{23} , and $[\text{Ne III}]/[\text{O II}]$ with increasing M_* are present in all samples, again suggesting that O/H increases with increasing M_* at each redshift. At fixed M_* , all four line ratios are significantly higher at $z \sim 2.3$ than at $z \sim 0$. In contrast, the line ratios only slightly increase at fixed M_* from $z \sim 2.3$ to $z \sim 3.3$. Collectively, these empirical trends represent a significant increase in excitation, implying a large decrease in O/H at fixed M_* between $z \sim 0$ and $z \sim 2.3$, but only a small change in O/H at fixed M_* between $z \sim 2.3$ and $z \sim 3.3$. At $z \sim 0$, all line ratios flatten at high masses, pointing toward a saturation in O/H at high M_* . No saturation at high M_* is observed in the high-redshift samples, except for $[\text{Ne III}]/[\text{O II}]$ of the highest-mass bins that may indicate low-level AGN activity is present in addition to star formation. These empirical trends provide a qualitative picture of the MZR and its evolution, regardless of which strong-line metallicity calibrations are employed.

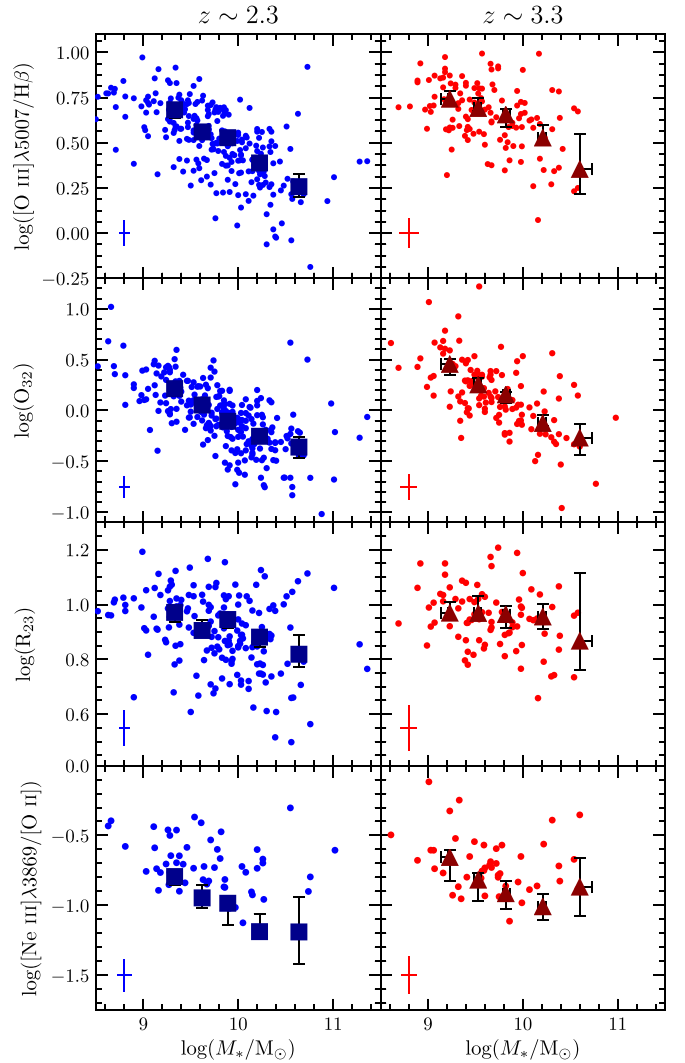


Figure 5. Reddening-corrected emission-line ratios vs. M_* for $z \sim 2.3$ (left) and $z \sim 3.3$ (right) individual galaxies (small circles) and stacked spectra in bins of M_* (large squares/triangles). Individual galaxies with $S/N \geq 3$ for each line in a particular ratio are shown. The error bar in the lower-left corner of each panel displays the median uncertainty of the individual galaxies.

4.2. The Mass–Metallicity Relation at $z = 0$ – 3.3

We present the MZR at $z \sim 2.3$ (left) and $z \sim 3.3$ (right) in Figure 7, with O/H estimated as described in Section 3. We find a clear correlation between O/H and M_* for both individual galaxies and composite spectra. The $z \sim 2.3$ and $z \sim 3.3$ individual galaxy samples have Spearman correlation coefficients of 0.68 and 0.56, respectively, with the p value $\ll 10^{-5}$ at both redshifts, indicating that the correlations between M_* and metallicity are highly significant. No obvious curvature in the relation is apparent at either redshift. The $z \sim 3.3$ sample displays slightly lower metallicity at fixed M_* than the $z \sim 2.3$ sample.

The MZRs for stacked spectra at $z \sim 0$, $z \sim 2.3$, and $z \sim 3.3$ are shown in Figure 8. Over the range of masses covered by our samples, we find a monotonic evolution toward lower metallicity with increasing redshift. The evolution from $z \sim 0$ to $z \sim 2.3$ is markedly larger than the evolution from $z \sim 2.3$ to $z \sim 3.3$. Because the high-redshift data do not obviously display a flattening at high mass, we fit the $z \sim 2.3$ and

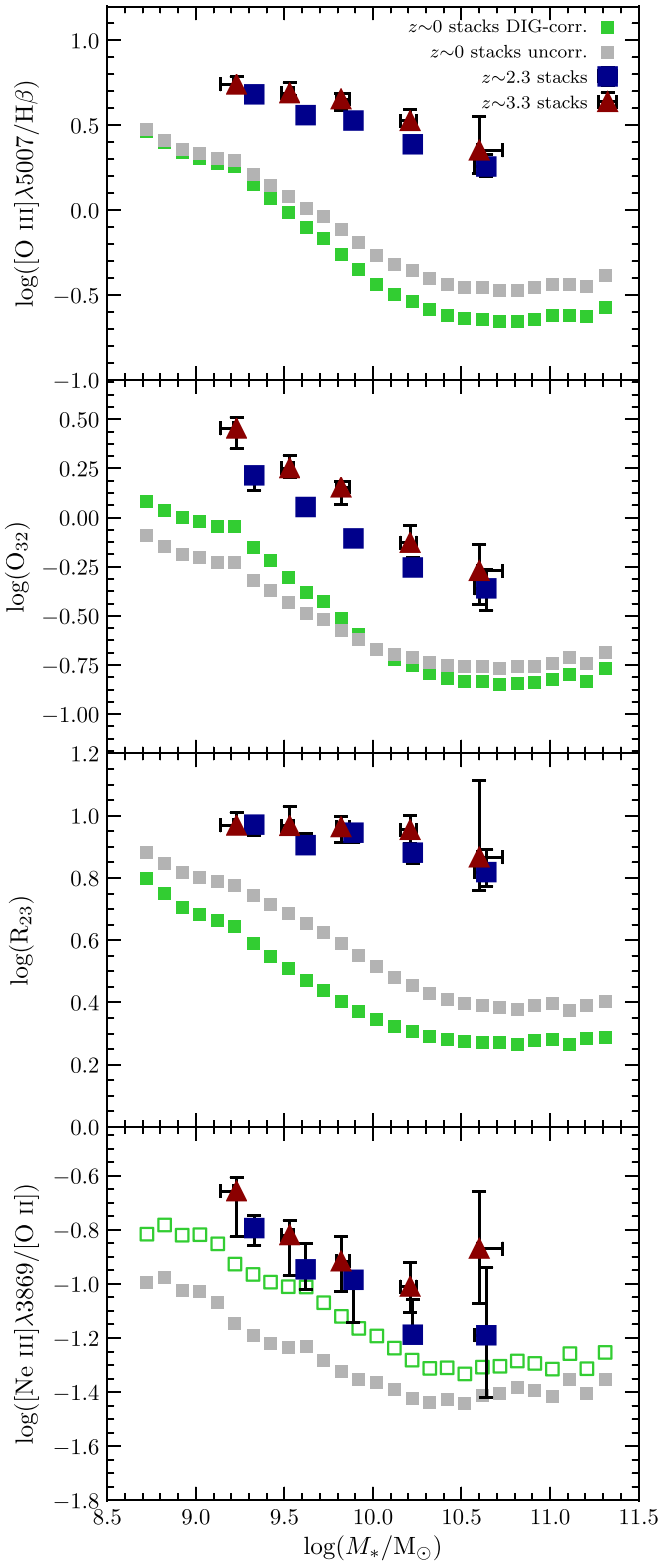


Figure 6. Reddening-corrected emission-line ratios vs. M_* for stacked spectra at $z \sim 0$, $z \sim 2.3$ (blue), and $z \sim 3.3$ (red). Both DIG-corrected (green) and uncorrected (gray) stacks at $z \sim 0$ are displayed. The open green squares in the lower panel display the $[\text{Ne III}]/[\text{O II}]$ ratios at $z \sim 0$ after correcting only $[\text{O II}]$ for DIG emission because a DIG correction for $[\text{Ne III}]$ was not calibrated by Sanders et al. (2017), thus representing an upper limit on the DIG-corrected $[\text{Ne III}]/[\text{O II}]$ ratio.

$z \sim 3.3$ stacks with a single power law of the form

$$12 + \log(\text{O}/\text{H}) = \gamma \times m_{10} + Z_{10}, \quad (7)$$

where $m_{10} = \log(M_*/10^{10} M_\odot)$ and Z_{10} is the metallicity at $10^{10} M_\odot$. We exclude the highest-mass bins at each redshift from this power-law fit because of incompleteness in the MOSDEF sample at these masses (Section 2.4; Kriek et al. 2015). Accordingly, these fits are good over $9.0 \leq \log(M_*/M_\odot) \leq 10.5$, though we extend the lines in Figure 8 to $10^{11} M_\odot$ for comparison to the highest-mass bins. The best-fit relations and 1σ uncertainties are shown in Figure 8, and the best-fit parameters are given in Table 3.

We fit the $z \sim 0$ MZR with the parameterization of Curti et al. (2020b). This function is a smoothly broken power law that approaches a constant slope γ at masses below the turnover mass, M_{TO} , and asymptotes to a constant metallicity Z_0 above M_{TO} . The functional form is

$$12 + \log(\text{O}/\text{H}) = Z_0 - \gamma/\Delta \times \log \left[1 + \left(\frac{M_*}{M_{\text{TO}}} \right)^{-\Delta} \right], \quad (8)$$

where Δ is a smoothness parameter that dictates how sharp the transition between the two mass regimes is at M_{TO} . The transition region becomes smaller (i.e., higher curvature) as Δ increases. Unlike earlier works that employed similar functional forms of the MZR that had a fixed curvature (e.g., Moustakas et al. 2011; AM13; Zahid et al. 2014a), Equation (8) allows for the curvature to be fit along with M_{TO} , Z_0 , and γ . The best-fit parameters to both the DIG-corrected and uncorrected $z \sim 0$ stacks are presented in Table 3 and shown in Figure 8 by the green and gray lines, respectively. The MZR shape is very similar between the two cases, but the normalization is ≈ 0.05 dex higher without correcting for DIG. We consider the DIG-corrected data to be more accurate (Section 2.3.2) and therefore adopt this as the fiducial case at $z \sim 0$. Our best-fit $z \sim 0$ MZR is very similar to the best-fit relation of Curti et al. (2020b), fit to median values of individual SDSS galaxies binned by stellar mass instead of stacked spectra. These authors find $\gamma = 0.28 \pm 0.02$, $\log(M_{\text{TO}}/M_\odot) = 10^{10.02 \pm 0.09} M_\odot$, and $Z_0 = 8.793 \pm 0.005$, consistent with our values, although they infer a smaller curvature ($\Delta = 1.2 \pm 0.2$).

4.2.1. Low-mass Slope, Normalization, and Scatter

At all redshifts, we find that the low-mass behavior of the MZR is consistent with a power law, with no evidence of the MZR slope either increasing or decreasing toward $10^9 M_\odot$. The best-fit low-mass MZR slopes are remarkably consistent to high precision across all three redshifts, with $\gamma = 0.28 \pm 0.01$ at $z \sim 0$, 0.30 ± 0.02 at $z \sim 2.3$, and 0.29 ± 0.02 at $z \sim 3.3$. This invariance of the MZR slope over 12 Gyr of cosmic time suggests that the same process sets the slope of the MZR over $z = 0-3.3$.

At $10^{10} M_\odot$, the metallicities of the best-fit relations are $12 + \log(\text{O}/\text{H}) = 8.77 \pm 0.01$ at $z \sim 0$, 8.51 ± 0.02 at $z \sim 2.3$, and 8.41 ± 0.03 at $z \sim 3.3$. Thus, at $\log(M_*/M_\odot) = 10.0$, we find an evolution of -0.26 ± 0.02 dex in O/H from $z \sim 0$ to $z \sim 2.3$, and -0.10 ± 0.03 between $z \sim 2.3$ and $z \sim 3.3$. Because the low-mass slopes are almost identical, the offset in metallicity at fixed M_* between $z \sim 2.3$ and $z \sim 3.3$ is nearly constant below $10^{10.5} M_\odot$. Likewise, the O/H offset at fixed M_* between the $z \sim 0$ stacks and the high-redshift samples is constant below $\sim 10^{10.2} M_\odot$, decreasing at higher masses as the $z \sim 0$ MZR flattens. Given the median redshifts of our samples ($z_{\text{med}} = [0.08,$

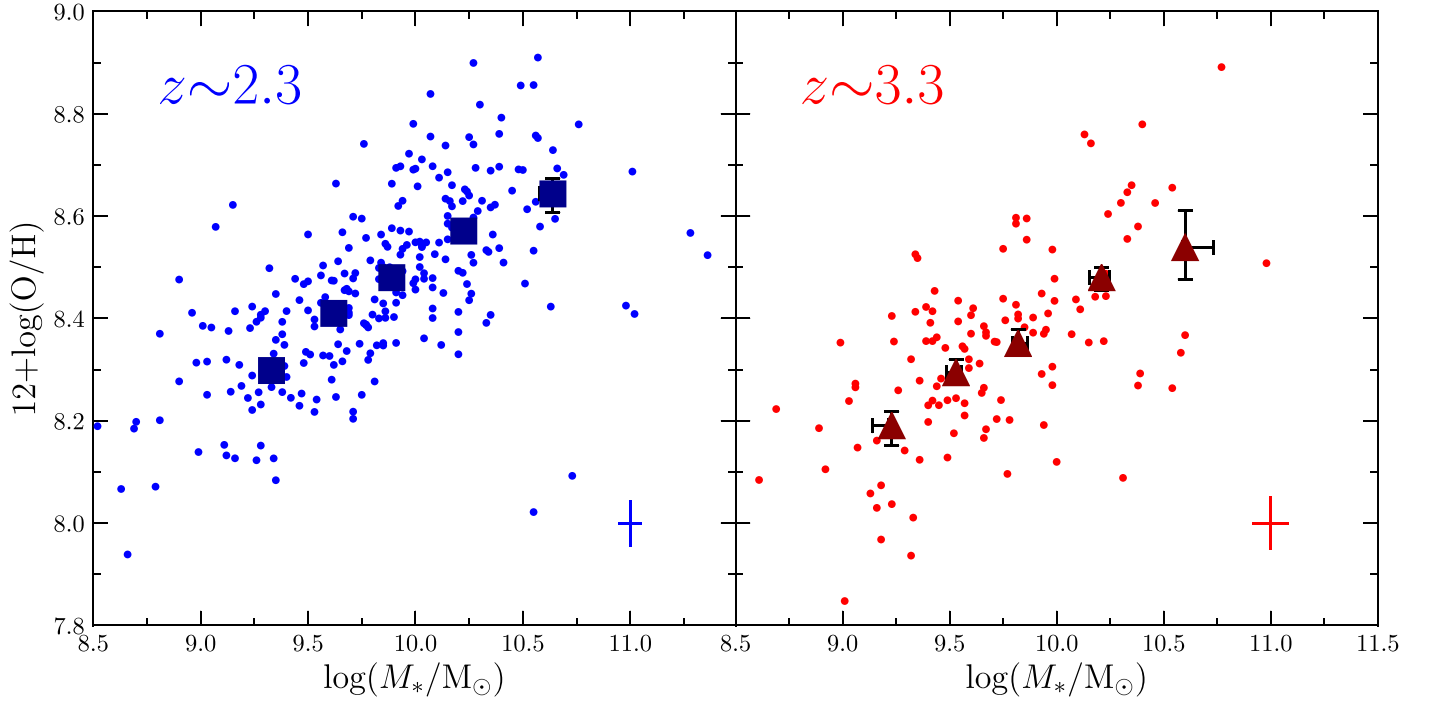


Figure 7. The MZR at $z \sim 2.3$ (left) and $z \sim 3.3$ (right) for individual galaxies (small circles) and stacked spectra in bins of M_* (large squares/triangles). The error bar in the lower-right corner of each panel displays the median uncertainty of the individual galaxies.

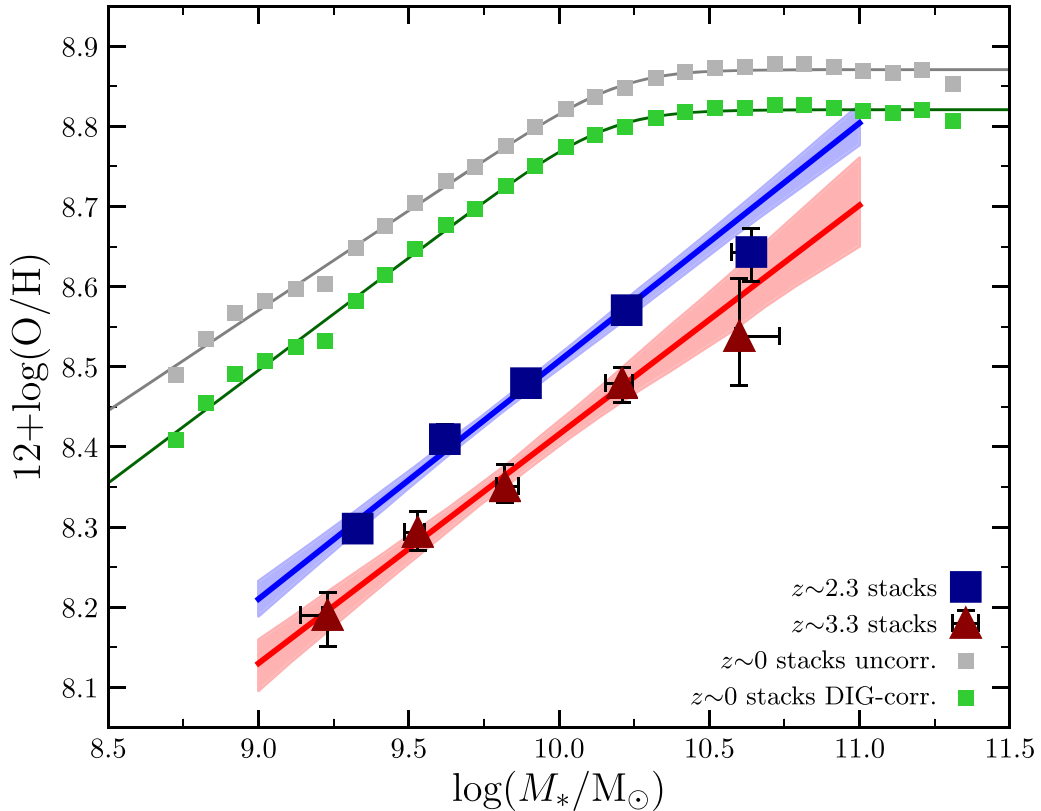


Figure 8. MZR for stacked spectra at $z \sim 0$, $z \sim 2.3$ (blue), and $z \sim 3.3$ (red). Both DIG-corrected (green) and uncorrected (gray) values are shown for the $z \sim 0$ stacks. The formal uncertainty in O/H for the $z \sim 0$ stacks is typically smaller than the size of the points. The solid lines represent the best-fit relations at each redshift, while the shaded regions display the 1σ uncertainties of the fits at $z \sim 2.3$ and $z \sim 3.3$. The $z \sim 0$ data are fit using a smoothly broken power law (Equation (8)). At $z \sim 2.3$ and $z \sim 3.3$, the stacks (excluding the highest-mass bin) are fit with a power law (Equation (7)).

2.28, 3.24]), the data are consistent with a uniform metallicity evolution of $d\log(O/H)/dz = -0.11 \pm 0.02$ below $10^{10.2} M_\odot$ (the turnover mass at $z \sim 0$).

We utilize the formal measurement uncertainties (σ_{meas}) on the metallicities and the scatter in the calibrations (σ_{cal}) to estimate the intrinsic scatter (σ_{int}) of the MZR at $z \sim 2.3$ and $z \sim 3.3$, assuming

Table 3Best-fit Mass–Metallicity Relations to $z \sim 0$, $z \sim 2.3$, and $z \sim 3.3$ Composite Spectra

$z \sim 2.3$ and $z \sim 3.3$ Fits Using Equation (7)				
Sample	γ	Z_{10}		
$z \sim 2.3$	0.30 ± 0.02	8.51 ± 0.02		
$z \sim 3.3$	0.29 ± 0.02	8.41 ± 0.03		
$z \sim 0$ Fits Using Equation (8)				
	Z_0	$\log\left(\frac{M_{\text{TO}}}{M_{\odot}}\right)$	γ	Δ
$z \sim 0$ DIG corr.	8.82 ± 0.01	10.16 ± 0.03	0.28 ± 0.01	3.43 ± 0.92
$z \sim 0$ uncorr.	8.87 ± 0.01	10.20 ± 0.03	0.25 ± 0.01	3.66 ± 1.16

the observed scatter is $\sigma_{\text{obs}}^2 = \sigma_{\text{int}}^2 + \sigma_{\text{meas}}^2 + \sigma_{\text{cal}}^2$. Individual MOSDEF galaxies (Figure 7) have an observed scatter of 0.14 (0.17) dex in O/H at fixed M_* around the best-fit $z \sim 2.3(3.3)$ MZR. The mean O/H measurement uncertainty is 0.04(0.05) dex at $z \sim 2.3(3.3)$. The B18 calibrations are based on stacked spectra and thus do not have measured calibration scatters. We instead assume the same scatter in line ratio at fixed O/H as for the $z \sim 0$ calibrations (Table 2), convert to scatter in O/H at a fixed line ratio using the slope of the calibrations at $12 + \log(\text{O}/\text{H}) = 8.4$ (the mean metallicity of the MOSDEF samples), and take the average of the calibration scatters among the set of line ratios used to derive the metallicities. In this way, we estimate the calibration scatter to be 0.11 dex in O/H. We infer the intrinsic 1σ scatter of the MZR to be 0.08 dex at $z \sim 2.3$ and 0.11 dex at $z \sim 3.3$, consistent with the intrinsic scatter of the $z = 0$ MZR of ≈ 0.1 dex (Tremonti et al. 2004; Kewley & Ellison 2008; Mannucci et al. 2010; Yates et al. 2012; Curti et al. 2020b).

4.2.2. Turnover Mass and Asymptotic Metallicity

The $z \sim 0$ MZR clearly flattens and approaches an asymptotic O/H at high masses. Our best-fit $z \sim 0$ MZR has a turnover mass of $\log(M_{\text{TO}}/M_{\odot}) = 10.16 \pm 0.03$ and a high-mass asymptotic metallicity of $Z_0 = 8.82 \pm 0.01$. The high-mass flattening reflects the underlying physics that govern ISM metallicity, such that the differing behavior of the MZR at high M_* implies some fundamental change in metal production, dilution, and/or retention/removal (e.g., Tremonti et al. 2004; Zahid et al. 2014a; Torrey et al. 2019). The turnover mass has been found to increase with increasing redshift out to $z \sim 1.5$, while Z_0 displays little evolution over this range (Zahid et al. 2014a, 2014b). It is of interest to see if these trends continue at $z > 2$.

The highest-mass bins at $z \sim 2.3$ and $z \sim 3.3$ fall below the best-fit MZR at each redshift, suggesting a possible flattening of the high-redshift MZR beginning at $\sim 10^{10.5} M_{\odot}$. However, both highest-mass bins are $< 2\sigma$ consistent with the single power-law fits. These bins have the largest O/H uncertainties because they contain the lowest number of galaxies (see Table 1). Furthermore, the highest-mass bins are potentially biased against red, dusty, metal-rich galaxies (see Section 2.4), which may explain why they fall below the power law that fits the lower-mass composites. Due to these uncertainties and biases, we cannot place quantitative constraints on the value of M_{TO} or Z_0 at $z \sim 2.3$ – 3.3 . We can however say with confidence that the turnover mass at $z > 2$ must be larger than M_{TO} at $z \sim 0$ ($10^{10.2} M_{\odot}$) because we find no flattening in the four MOSDEF bins where the sample is complete that span up to $\log(M_*/M_{\odot}) = 10.5$. Our data suggest that the

turnover mass at $z \sim 2.3$ is larger than the value found at $z \sim 1.4$ of $\log(M_{\text{TO}}/M_{\odot}) \approx 10.1$ by Zahid et al. (2014a) and is thus consistent with their finding that M_{TO} increases with increasing redshift.

Constraining the high-mass behavior of the MZR at $z > 2$ and confirming whether the MZR flattens at all at these redshifts will require significantly larger and more complete samples of galaxies at $\log(M_*/M_{\odot}) > 10.5$. If the single power laws hold with no flattening, then the $z \sim 2.3(3.3)$ MZR would reach $Z_0(z=0)$ at $\log(M_*/M_{\odot}) \approx 11.0(11.5)$. A robust investigation of the high-mass behavior should thus be well sampled up to at least $10^{11.0} M_{\odot}$. Given the rarity of such massive star-forming systems at high redshifts, assembling a sufficient sample will require a very wide area search exceeding that of existing deep legacy fields (e.g., CANDELS). Constraining the high-mass MZR is crucial to understanding whether there are two regimes of metal processing in galaxies at high redshifts as at $z \sim 0$.

4.3. The Fundamental Metallicity Relation at $z = 0$ – 3.3

We now investigate the three-dimensional relation among M_* , O/H, and SFR (i.e., the FMR), and whether this relation evolves with redshift. We show O/H versus M_* color-coded by SFR at $z \sim 0$ (circles), $z \sim 2.3$ (squares), and $z \sim 3.3$ (triangles) in the left panel of Figure 9, where the $z \sim 0$ stacks are now those of AM13 binned in both M_* and SFR. We limit the $z \sim 0$ sample to those M_* –SFR bins containing at least five galaxies to ensure the stacks still represent a sample average. This cut primarily limits the stacks at $< 10^{10.0} M_{\odot}$ with $\log(\text{SFR}/M_{\odot} \text{ yr}^{-1}) > 1.5$ because of the rarity of galaxies with such extreme sSFRs in the local universe. The high-redshift samples appear to show good agreement in O/H with the $z \sim 0$ stacks where low-redshift stacks matched in M_* and SFR exist. There are no $z \sim 0$ stacks closely matched to the highest-mass $z \sim 2.3$ bin or the three highest-mass $z \sim 3.3$ bins. We note that the high-redshift stacks remain in close agreement with matched $z \sim 0$ stacks without DIG correction because the DIG corrections to these high-sSFR $z \sim 0$ stacks are small due to their large H α surface brightnesses. However, the agreement is closer when a DIG correction is performed.

We parameterize the $z \sim 0$ FMR using the method of Mannucci et al. (2010), where the value of α is identified that minimizes the scatter in O/H at fixed μ_{α} , where

$$\mu_{\alpha} \equiv \log(M_*/M_{\odot}) - \alpha \times \log\left(\frac{\text{SFR}}{M_{\odot} \text{ yr}^{-1}}\right). \quad (9)$$

While this simplistic functional form of the FMR can fail to capture the detailed flattening and turnover behavior at very high masses and low sSFRs (Yates et al. 2012; Curti et al. 2020b), we find that it is sufficient to describe the behavior over the range of masses and SFRs spanned by the $z \sim 0$ stacks. For a range of α , we fit $12 + \log(\text{O}/\text{H})$ versus μ_{α} of the $z \sim 0$ stacks with a cubic function and calculate the residuals about the best-fit function. We find that the scatter of the $z \sim 0$ stacks is minimized at a value of $\alpha = 0.60$ (right panel inset in Figure 9). This best-fit α is in close agreement with the values inferred using direct-method metallicities alone ($\alpha = 0.55$ – 0.70 ; AM13; Sanders et al. 2017) and is also close to best fit for individual SDSS galaxies of $\alpha = 0.55$ found by Curti et al. (2020b). The best-fit $z \sim 0$ FMR is shown by the black line in the right panel of Figure 9, with a

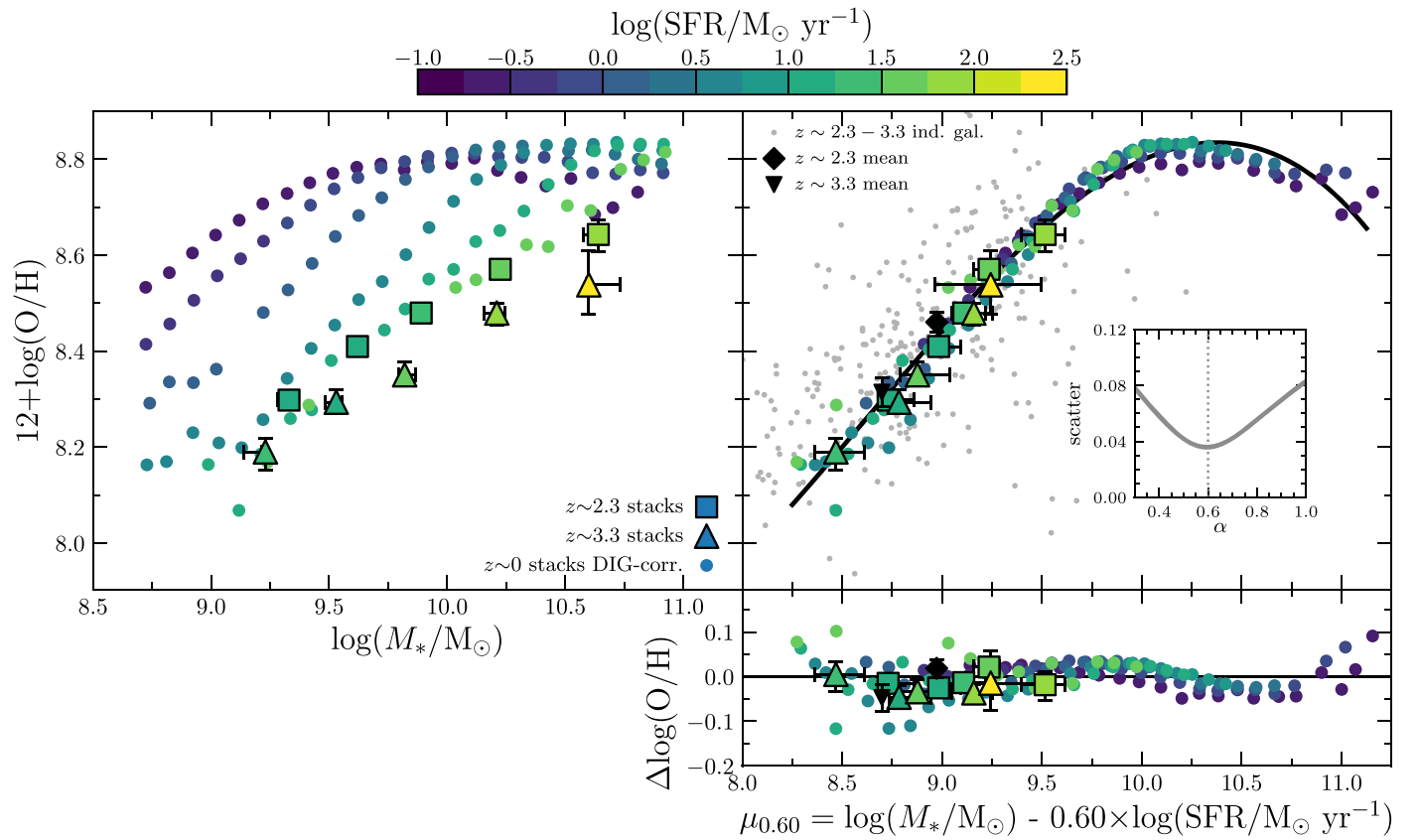


Figure 9. Left: O/H vs. M_* for stacked spectra of galaxies at $z \sim 0$ (circles), $z \sim 2.3$ (squares), and $z \sim 3.3$ (triangles). Points are color-coded by SFR, where the SFR is determined using dust-corrected H α or H β for all samples. Upper right: projection of the FMR as O/H vs. $\mu_{0.60} = \log(M_*/M_\odot) - 0.60 \times \log(\text{SFR}/M_\odot \text{ yr}^{-1})$, where the coefficient of the SFR, $\alpha = 0.60$, is that which minimizes the scatter of the $z \sim 0$ M_* +SFR binned stacks. The inset panel presents the $z \sim 0$ scatter in O/H at fixed μ_α as a function of α . The black line displays the best-fit cubic function to the $z \sim 0$ stacks, given in Equation (10). Gray circles show $z \sim 2.3$ and $z \sim 3.3$ individual galaxies with metallicity measurements, while the black diamond and triangle show the mean values of these galaxies at $z \sim 2.3$ and $z \sim 3.3$, respectively. Lower right: residuals in O/H around the best-fit $z \sim 0$ FMR projection (black line, upper right). The high-redshift galaxies show excellent agreement with the $z \sim 0$ FMR.

functional form of

$$12 + \log(\text{O}/\text{H}) = 8.80 + 0.188y - 0.220y^2 - 0.0531y^3, \quad (10)$$

where $y = \mu_{0.60} - 10$. In this parameter space, the $z \sim 2.3$ and $z \sim 3.3$ stacks fall directly on the best-fit $z \sim 0$ FMR, despite the high-redshift stacks not being included in the fitting process.

The lower panel of Figure 9 displays the metallicity residuals at fixed $\mu_{0.60}$ about the best-fit $z \sim 0$ FMR. Collectively, the weighted-mean offset of all high-redshift stacks is $\Delta \log(\text{O}/\text{H}) = -0.01 \pm 0.02$ dex, where the uncertainty reported here is the error of the weighted mean. The individual MOSDEF galaxies with both metallicity and SFR detections (gray points, Figure 9) have a mean offset in O/H of 0.04 ± 0.02 at $z \sim 2.3$ and 0.02 ± 0.03 at $z \sim 3.3$ (black points, Figure 9). We thus find that a single relation among M_* , SFR, and O/H can describe the mean properties of galaxy samples over $z = 0$ – 3.3 with high precision. In other words, the FMR does not evolve out to $z \sim 3.3$.

The observed scatter of the O/H residuals of the individual galaxies, taken to be the standard deviation, is 0.16 dex at $z \sim 2.3$ and 0.22 dex at $z \sim 3.3$. We perform the same scatter analysis as for the MZR (Section 4.2.1), except here measurement errors account for uncertainty in both O/H and SFR because $\mu_{0.60}$ depends on SFR and the SFRs carry significant errors (typically

~ 0.2 – 0.3 dex). After removing the measurement uncertainty in $\Delta \log(\text{O}/\text{H})$ at fixed $\mu_{0.60}$ ($\sigma_{\text{meas}} = 0.10$ (0.18) dex at $z \sim 2.3$ (3.3)) and the metallicity calibration scatter of $\sigma_{\text{cal}} = 0.11$ dex, we find an intrinsic scatter around the best-fit FMR of 0.06 dex at both $z \sim 2.3$ and $z \sim 3.3$. This intrinsic FMR scatter is lower than the intrinsic MZR scatter at $z \sim 2.3$ (3.3) of 0.08 (0.12) dex (Section 4.2.1), indicating a second parameter dependence on SFR is present in the high-redshift data. At $z = 0$, the intrinsic scatter of the FMR is ≈ 0.05 dex (e.g., Mannucci et al. 2010; Cresci et al. 2019; Curti et al. 2020b), where the inclusion of SFR as an additional parameter has decreased the scatter from the value of 0.1 dex found for the MZR. We thus find that the addition of SFR as a secondary parameter to the MZR results in a similar decrease in the intrinsic scatter in O/H at $z \sim 2.3$ and $z \sim 3.3$, from ≈ 0.10 dex around the MZR to 0.06 dex around the FMR.

The FMR projection in the right panel of Figure 9 displays a flattening above $\mu_{0.60} = 10.0$ where O/H has no dependence on SFR at fixed M_* . This flattening behavior at high mass and low SFR is a feature on which there is a consensus in the literature (e.g., Mannucci et al. 2010; Yates et al. 2012; AM13; Telford et al. 2016; Cresci et al. 2019; Curti et al. 2020b). The highest-mass $z \sim 2.3$ stack has $\mu_{0.60} = 9.5$, below the regime where the $z \sim 0$ stacks begin to flatten. Even at $\log(M_*/M_\odot) = 11.0$, $z \sim 2.3$ galaxies would only have $\mu_{0.60} \approx 9.7$ assuming our best-fit SFR– M_* relation holds (Equation (3)), making it impractical to probe $\mu_{0.60} > 10.0$ with samples at $z > 2$. It is of

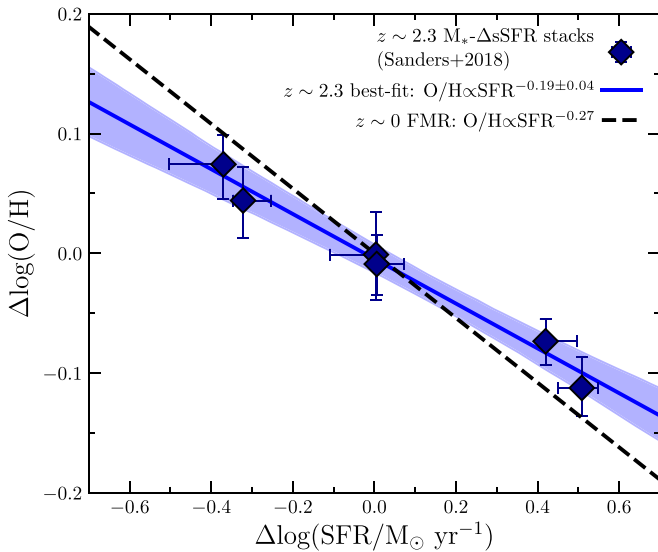


Figure 10. Residuals around the best-fit MZR ($\Delta\log(\text{O}/\text{H})$) vs. residuals around the best-fit SFR- M_* relation ($\Delta\log(\text{SFR})$) for the $z \sim 2.3$ M_* - ΔsSFR stacks of Sanders et al. (2018, blue diamonds). The metallicities of these stacks have been rederived using the methods in this work (Section 3). The blue line and shaded region show the best-fit relation to the $z \sim 2.3$ stacks, while the black dashed line displays the dependence of O/H on SFR at fixed M_* predicted by the best-fit $z \sim 0$ FMR.

interest to more extensively test the FMR using high-mass and low-SFR galaxies at intermediate redshifts ($z \sim 0.5$ – 1.5) to confirm whether the flattening at high $\mu_{0.60}$ remains beyond the local universe.

At $\mu_{0.60} < 9.5$, the best-fit FMR can be described as a power law of the form $\text{O}/\text{H} \propto \mu_{0.60}^{0.45}$. Accordingly, $\text{O}/\text{H} \propto \text{SFR}^{-0.27}$ at fixed M_* in the best-fit FMR, based on the definition of $\mu_{0.60}$ (Equation (9)). For $\text{O}/\text{H} \propto \text{SFR}^\nu$, Sanders et al. (2018) found $\nu = -0.11$ to -0.27 for MOSDEF star-forming galaxies at $z \sim 2.3$, where the strength of the SFR dependence varied with the choice of metallicity indicator and calibration. We rederived metallicities for the Sanders et al. (2018) stacks that were binned in M_* and offset from the $z \sim 2.3$ SFR- M_* relation (the “ M_* - ΔsSFR ” stacks) using the reported O_{32} and $[\text{O III}]/\text{H}\beta$ ratios ($[\text{Ne III}]$ was not covered in these stacks) and the B18 high-redshift analog calibrations. The $z \sim 2.3$ sample in this work has $\sim 80\%$ overlap with that of Sanders et al. (2018), thus the stacks of Sanders et al. (2018) should be a fair representation of our sample.

In Figure 10, we compare the residuals around the MZR at fixed M_* ($\Delta\log(\text{O}/\text{H})$) to the residuals around the SFR- M_* relation at fixed M_* ($\Delta\log(\text{SFR})$) for the M_* - ΔsSFR stacks. The best-fit power law to the $z \sim 2.3$ stacks has $\nu = -0.19 \pm 0.04$ (blue line). This relation is shallower than what is expected from the best-fit $z \sim 0$ FMR ($\nu = -0.27$), but the offset is not statistically significant (2σ). We thus find that the dependence of O/H on SFR at fixed M_* internal to the $z \sim 2.3$ sample is consistent with the expectation from the best-fit $z \sim 0$ FMR. Because of the smaller sample size and larger uncertainties on O/H and SFR, performing this exercise with stacks of the $z \sim 3.3$ sample does not produce any useful constraints. In summary, the secondary dependence of O/H on SFR is significantly detected at $z \sim 2.3$ and is consistent at 2σ with the dependence measured at $z \sim 0$.

Potential systematic biases remain in the comparison of the $z \sim 0$ and $z > 2$ FMR. Based on the correlation between high

sSFR and extreme ISM conditions (see discussion in Section 3), a different metallicity calibration may be needed for $z \sim 0$ high-sSFR galaxies relative to $z \sim 0$ main-sequence galaxies. This approach will affect the comparison of low- and high-redshift galaxies in the FMR plane. For example, if we apply the B18 calibrations to the $z \sim 0$ M_* -SFR stacks with $\log(\text{sSFR}/\text{Gyr}^{-1}) > -0.5$, it introduces a small offset of -0.05 dex in O/H between the $z > 2$ stacks and the $z \sim 0$ stacks most closely matched in M_* and SFR. More accurate derivations of the FMR and its evolution require a move beyond simple one-dimensional metallicity calibrations to multidimensional calibrations that take into account variations in ISM conditions across the galaxy population. Such relations may be able to unify high-redshift and local calibrations into a single framework. Brown et al. (2016) investigated the possibility of sSFR-dependent metallicity calibrations but did not include corrections for contributions from DIG emission that are highly sSFR dependent (e.g., Sanders et al. 2017; Vale Asari et al. 2019). The combination of high-quality spectra and large sample sizes at $z > 2$ has reduced the measurement uncertainties to a level where these finely detailed systematic effects need to be addressed in future FMR studies.

4.4. Systematic Effects on the High-redshift MZR

We now investigate how assumptions for determining stellar masses and deriving metallicities from strong-line ratios systematically affect the shape and normalization of the MZR of the $z \sim 2.3$ and $z \sim 3.3$ samples. Figure 11(a) displays the case for our fiducial assumptions for SED fitting to estimate stellar masses (Section 2.2.2) and the B18 high-redshift analog calibrations to infer metallicities from $[\text{O II}]$, $[\text{Ne III}]$, $[\text{O III}]$, and $\text{H}\beta$ (Section 3). In this and the following panels of Figure 11, we display the high-redshift stacks, power-law fits to the stacks (excluding the highest-mass bin) and print the best-fit slope of the MZR (γ_2 (γ_3) at $z \sim 2.3$ (3.3)) as well as the O/H offset at $\log(M_*/M_\odot) = 10.0$ from $z \sim 0$ to $z \sim 2.3$ ($\Delta\log(\text{O}/\text{H})_{0 \rightarrow 2}^{10.0}$) and from $z \sim 2.3$ to $z \sim 3.3$ ($\Delta\log(\text{O}/\text{H})_{2 \rightarrow 3}^{10.0}$). The best-fit MZRs at $z \sim 0$, $z \sim 2.3$, and $z \sim 3.3$ under our fiducial set of assumptions are shown by the gray lines in all panels. We only show MZR variations for the high-redshift samples as the uncertainties pertaining to metallicity derivations and SED fitting are considerably larger at high redshift than at $z \sim 0$.

We first vary our SED-fitting assumptions for determining stellar masses in panels (b)–(d) of Figure 11. For each SED-fitting case, we remake the stacks according to the methods in Section 2.4 using the new stellar masses to populate the mass bins. In Figure 11(b), we show the effect when the photometry is not corrected for the contribution from emission lines, resulting in a slightly steeper $z \sim 2.3$ MZR with slightly lower normalization. This effect arises because low-mass galaxies have higher emission-line equivalent widths (Reddy et al. 2018b) that contribute more strongly to the rest-optical photometry leading to an overestimate of M_* , while at high mass, the equivalent widths are lower and do not significantly change the masses. At $z \sim 3.3$, galaxies have higher emission-line equivalent widths at fixed M_* than at $z \sim 2.3$ such that even the high- M_* $z \sim 3.3$ galaxy masses are biased by emission-line contaminated photometry, leading to a similar slope but systematically lower normalization compared to our fiducial case.

We assume a Small Magellanic Cloud (SMC) extinction law (Gordon et al. 2003) and subsolar metallicity ($Z_* = 0.0031$) in

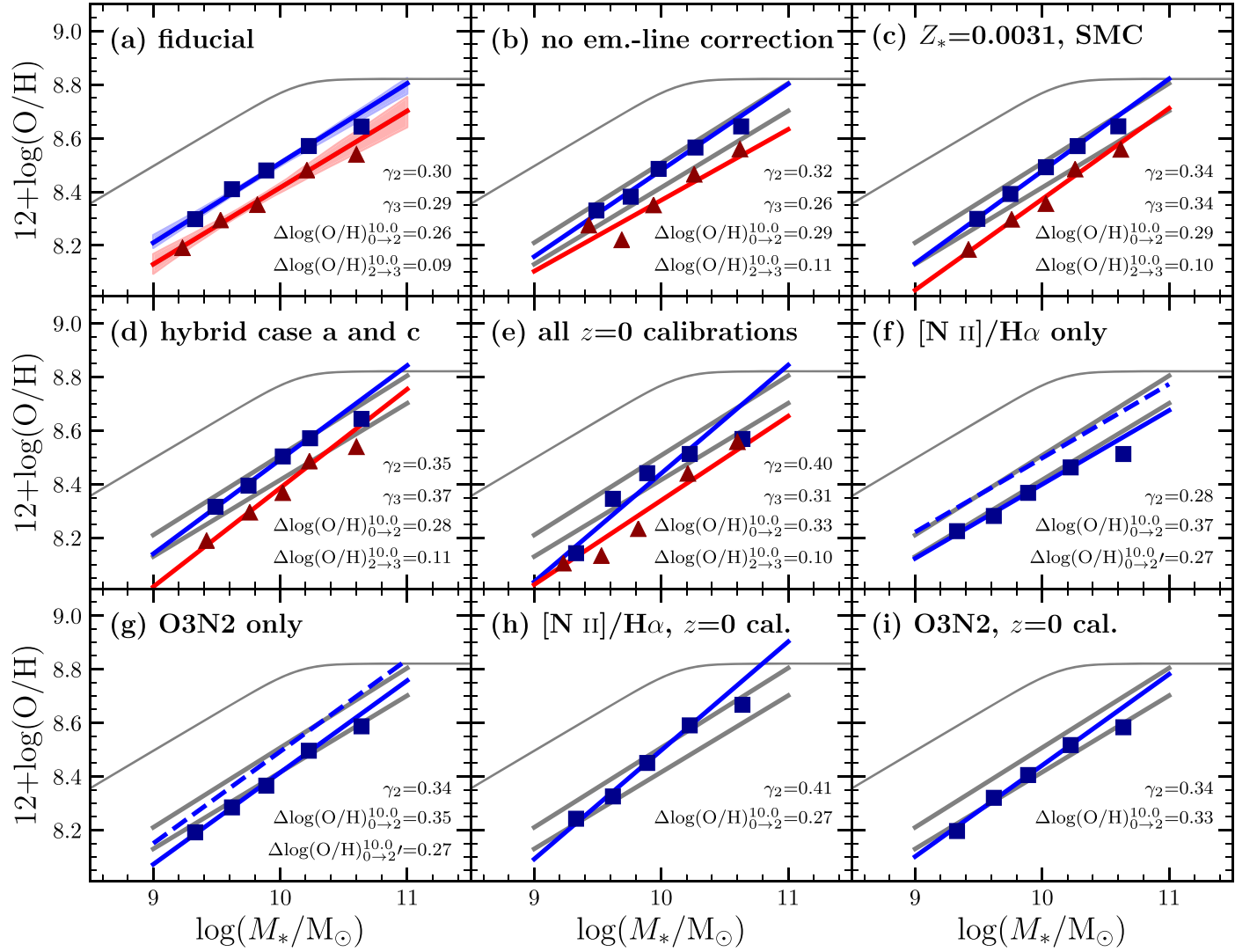


Figure 11. Each panel shows stacks and fits to the $z \sim 2.3$ (blue) and $z \sim 3.3$ (red) MZR, where assumptions regarding SED fitting for stellar masses or calibrations for metallicity derivation are varied in each panel as described by the text at the top of each panel. Panel (a) presents the $z \sim 2.3$ and $z \sim 3.3$ MZRs under our fiducial set of assumptions. In each panel, the fiducial best-fit MZRs at $z \sim 0$, $z \sim 2.3$, and $z \sim 3.3$ are shown as gray lines for comparison. The text in the lower-right corner gives the best-fit MZR slopes at $z \sim 2.3$ (γ_2) and $z \sim 3.3$ (γ_3), as well as the offset in O/H at $10^{10} M_\odot$ from $z \sim 0$ to $z \sim 2.3$ ($\Delta \log(\text{O}/\text{H})_{0 \rightarrow 2.3}^{10.0}$) and from $z \sim 2.3$ to $z \sim 3.3$ ($\Delta \log(\text{O}/\text{H})_{2.3 \rightarrow 3}^{10.0}$). In panels (f) and (g), the dashed blue line displays the MZR inferred when shifting the B18 high-redshift analog calibrations 0.15 dex lower in $[\text{N II}]/\text{H}\alpha$ and higher in O3N2 such that the B18 excitation sequences match those of the MOSDEF $z \sim 2.3$ sample in the $[\text{N II}]$ BPT diagram.

Figure 11(c), as suggested to be appropriate for high-redshift galaxies by some works (Capak et al. 2015; Reddy et al. 2015, 2018a; Shivaee et al. 2020), finding slightly steeper slopes and lower normalizations that only differ from our fiducial case by $\sim 2\sigma$. Recent studies at $z \sim 2$ have suggested that the stellar attenuation curve steepens with decreasing M_* and metallicity (Reddy et al. 2018a; Shivaee et al. 2020). Motivated by these results, we show a hybrid of our fiducial case (a) and the SMC/subsolar metallicity case (c) in Figure 11(d), where we assume the fiducial assumptions (Calzetti et al. (2000) curve, solar metallicity) at $\log(M_*/M_\odot) > 10.0$ and the SMC curve and subsolar metallicity at $\log(M_*/M_\odot) < 10.0$. The result is that the two highest-mass bins have not changed compared to the fiducial case, while the lower-mass bins have slightly higher M_* , again resulting in only slightly steeper slopes and marginally lower normalizations.

In panels (e)–(i) of Figure 11, we vary the metallicity calibration used to convert strong-line ratios to O/H. Figure 11(e) shows the results when we use the same set of emission lines but apply the

normal $z = 0$ calibrations from this work (Figure 3, Table 2) to the $z \sim 2.3$ and $z \sim 3.3$ samples. We find overall lower normalization by 0.05 dex at both redshifts and some change to the slope at $z \sim 2.3$, but the relative offset between $z \sim 2.3$ and $z \sim 3.3$ remains unchanged. Though not shown here, we found that the $z > 2$ MZR normalization was slightly lower when using the $z \sim 0$ M08 and C17 calibrations as well. The relative offset between $z \sim 2.3$ and $z \sim 3.3$ was unchanged when employing C17 but was larger than our fiducial case when using M08. Further discussion of discrepancies between our results and past studies that used M08 can be found in Section 6.1.

To maintain a uniform set of emission lines over all redshifts, we have used only ratios of $[\text{O II}]$, $[\text{Ne III}]$, $\text{H}\beta$, and $[\text{O III}]$ to estimate metallicities. In panels (f)–(i), we investigate the use of calibrations based on ratios involving $[\text{N II}]$ ($[\text{N II}]/\text{H}\alpha$ and $\text{O3N2} = ([\text{O III}]/\text{H}\beta)/([\text{N II}]/\text{H}\alpha)$) and only show the $z \sim 2.3$ sample because $[\text{N II}]$ and $\text{H}\alpha$ are not covered at $z > 3$. Panels (f) and (g) show the $z \sim 2.3$ MZR using the $[\text{N II}]/\text{H}\alpha$ and O3N2 calibrations of the B18 high-redshift analogs. We find almost the

same slope as for the fiducial case but an offset 0.1 dex lower in normalization. We chose to use the B18 calibrations because direct-method metallicities at $z \sim 2$ match these calibrations on average (Sanders et al. 2018), but the $z \sim 2$ direct-method sample did not have sufficient coverage to test [N II]-based indicators. B18 selected high-redshift analogs to lie along the [N II] BPT sequence defined by the KBSS $z \sim 2.3$ sample (Steidel et al. 2014), which displays a larger offset from the $z \sim 0$ sequence in the [N II] BPT diagram (Figure 4; Shapley et al. 2015). The dashed blue line in panels (f) and (g) shows the resulting MZR if we shift the B18 calibration 0.15 dex lower (higher) in [N II]/H α (O3N2) at fixed O/H to match the [N II] BPT sequence of the MOSDEF $z \sim 2.3$ stacks.¹⁸ After shifting the B18 calibrations to match the MOSDEF [N II] BPT sequence, we find a good match between our fiducial MZRs and those based on [N II] indicators.

The final two panels, (h) and (i), show the $z \sim 2.3$ MZR derived using [N II]-based indicators and normal $z = 0$ calibrations. Similarly to case (e), we find slightly steeper slopes and a normalization that is 0.05–0.1 dex lower than the fiducial case. Panels (e), (h), and (i) collectively suggest that the primary effect of applying local calibrations to high-redshift samples is to underestimate O/H by 0.05–0.1 dex relative to calibrations that are appropriate for the ISM conditions at $z \sim 2$. Applying typical local calibrations to high-redshift samples thus leads to larger inferred evolution of O/H at fixed M_* and would also lead us to infer an offset of ~ 0.1 between $z > 2$ galaxies and the $z \sim 0$ FMR, as was reported using such methods in earlier works (Sanders et al. 2015, 2018).

In summary, we find that assumptions regarding how stellar masses are derived and how metallicities are inferred from strong-line ratios can affect the inferred slope and normalization of the high-redshift MZR. However, these systematic effects are not severe, with the slope varying between $\gamma = 0.28$ –0.41 ($\gamma = 0.30$ in the fiducial case) and the normalization varying no more than 0.05 dex in most cases, though offsets of up to 0.1 dex are possible when applying $z = 0$ calibrations to high-redshift samples. The latter effect carries important implications for the invariance of the FMR with redshift. Of particular note is the fact that the relative offset in O/H at fixed M_* between $z \sim 2.3$ and $z \sim 3.3$ is immune to the assumptions tested here, varying over only 0.10–0.12 dex. The evolution of the MZR slope and the relative offset in O/H between $z \sim 0$ and high redshift are somewhat affected by these systematics, but typically at $\lesssim 2\sigma$ relative to our fiducial case. As high-redshift measurements improve, a careful treatment of SED fitting and metallicity calibration choices will become increasingly important to produce robust evolutionary studies of metallicity scaling relations.

5. Analytic Chemical Evolution Modeling

We now turn to analytic galaxy evolution models to understand what physical processes set the slope and govern the evolution of the MZR over $z = 0$ –3.3. We model our measured metallicities using the formalism of PS11, which is more flexible than that of other models because it includes both

mass and metal loading of accretion and outflows (i.e., accreting material need not be pristine, and outflowing material may have a metallicity different from that of the ISM). In contrast, the gas-regulator model of Lilly et al. (2013) assumes that the outflowing material has the same metallicity as the ISM, while the equilibrium model of Davé et al. (2012) also assumes $Z_{\text{out}} = Z_{\text{ISM}}$ and that the rate of change of the gas reservoir mass is zero such that galaxy metallicities have no explicit dependence on the gas fraction or SFR (i.e., the FMR is not explicit in this formalism, as noted by Torrey et al. 2019).

In the PS11 model, the metallicity of the ISM is expressed as

$$Z_{\text{ISM}} = \frac{y}{\zeta_{\text{out}} - \zeta_{\text{in}} + \alpha \mu_{\text{gas}} + 1}, \quad (11)$$

where y is the nucleosynthetic stellar yield and $\mu_{\text{gas}} \equiv M_{\text{gas}}/M_*$ is the gas fraction. The coefficient to the gas fraction is

$$\alpha \equiv (1 - R) \left(\frac{d \log M_{\text{gas}}}{d \log M_*} + \frac{d \log Z_{\text{ISM}}}{d \log M_*} \right), \quad (12)$$

where R is the fraction of newly formed stellar mass that is returned to the ISM over time through stellar evolution processes, and α depends on the slope of $\mu_{\text{gas}}(M_*)$ and the MZR. The other terms in the denominator of Equation (11) are the metal loading factors of the outflowing galactic winds and inflowing gas accretion:

$$\zeta_{\text{out}} \equiv \frac{Z_{\text{out}}}{Z_{\text{ISM}}} \times \frac{\dot{M}_{\text{out}}}{\text{SFR}} \quad (13)$$

$$\zeta_{\text{in}} \equiv \frac{Z_{\text{in}}}{Z_{\text{ISM}}} \times \frac{\dot{M}_{\text{in}}}{\text{SFR}}, \quad (14)$$

where Z_{out} and Z_{in} are the metallicities of the outflows and inflows, and \dot{M}_{out} and \dot{M}_{in} are the mass rates of the outflows and inflows. The mass rates of gas flows are often parameterized as a ratio of the SFR in the mass-loading factors: $\eta_{\text{out}} = \dot{M}_{\text{out}}/\text{SFR}$ and $\eta_{\text{in}} = \dot{M}_{\text{in}}/\text{SFR}$.

In the PS11 framework, if the gas fraction and ISM metallicity are known (i.e., if $\mu_{\text{gas}}(M_*)$ and the MZR have been measured) and a return fraction and stellar yield are assumed, then the metal loading factors of the outflows and inflows can be solved for. As is common, we make the simplifying assumption that ζ_{in} is negligible so that we can uniquely solve for ζ_{out} . This assumption does not require the inflows to be pristine, but simply that $Z_{\text{in}} \ll Z_{\text{out}}$.¹⁹ If this criterion is not true of real galaxies, then our determinations of ζ_{out} represent lower limits. If $y/Z_{\text{ISM}} < 1 + \alpha \mu_{\text{gas}}$ (ignoring the ζ_{in} term), then ζ_{out} is unphysically negative. Thus, models with a low stellar yield cannot accommodate very high gas fractions.

There are only two terms in Equation (11) that serve to increase metallicity: y , representing nucleosynthetic production through star formation; and ζ_{in} , pertaining to accreted metals.

¹⁸ We could shift the B18 calibrations 0.1 dex lower in [O III]/H β to bring them into agreement with the MOSDEF [N II] BPT sequence, but such a shift would result in a worse agreement in the [O III]/H β versus O₃₂ and [Ne III]/[O II] diagrams (Figure 4) and with the $z \sim 2.2$ direct-method metallicities (Figure 3). For these reasons, we favor shifting [N II] alone, which could reflect differences in N/O between the two samples.

¹⁹ Note that, because launching sites of star formation driven outflows are also production sites of elements and Type II SNe ejecta are highly enriched ($Z_{\text{ej}} \sim 7Z_{\odot}$; Woosley & Weaver 1995; Nomoto et al. 2006; Romano et al. 2010; Nomoto et al. 2013), $Z_{\text{out}} \geq Z_{\text{ISM}}$. The case of $Z_{\text{out}} = Z_{\text{ISM}}$ is only reached if the outflow mass is dominated by entrained material over pure SNe ejecta.

Ignoring ζ_{in} , the stellar yield effectively sets a maximum ISM metallicity that is only reached if a system has no outflows and very little gas mass. The actual ISM metallicity is set by the other two terms (ζ_{out} and μ_{gas}) that serve to reduce metallicity through two distinct physical mechanisms. The μ_{gas} term represents the dilution mechanism whereby metals already present in the ISM and new metals from SNe are mixed into a larger hydrogen gas reservoir. The ζ_{out} term encapsulates the metal removal mechanism in which metals are removed from the galaxy ISM by outflows. Assuming y does not strongly depend on M_* and redshift, the slope and evolution of the MZR are determined by the dependence of both ζ_{out} and μ_{gas} on M_* and redshift.

In the following subsections, we apply the PS11 model to interpret our measurements of the MZR over $z=0\text{--}3.3$. We first solve for ζ_{out} and constrain its scaling with M_* by assuming a stellar yield, empirically motivated gas fractions, and $\zeta_{\text{in}}=0$. We then investigate the relative importance of dilution and metal removal in setting the slope of the MZR at each redshift and governing the evolution of the MZR with redshift.

5.1. Modeling the MZR at $z=0\text{--}3.3$

We model the MZR at $z=0\text{--}3.3$ under the following fiducial set of assumptions. We assume a stellar oxygen yield of $y_{\text{O}}=0.015$ as a mass fraction ($12 + \log(\text{O}/\text{H})_{\text{y}}=9.2$ as a number fraction) and a return fraction of $R=0.30$,²⁰ values appropriate for a Salpeter (1955) IMF with an upper mass cutoff of $100 M_{\odot}$ (Vincenzo et al. 2016). Both y_{O} and R are assumed to be constant with M_* and redshift. At $z \sim 0$, gas fractions as a function of M_* are derived from the empirical $\mu_{\text{gas}}(M_*, \text{SFR})$ relation of Saintonge et al. (2016) evaluated with our best-fit $z \sim 0$ SFR- M_* relation (Equation (2)). At $z > 1$, we adopt the $\mu_{\text{gas}}(M_*, z)$ calibration of Tacconi et al. (2018) evaluated on the star-forming main sequence ($\delta\text{MS}=0$) at $z=2.3$ and $z=3.3$. The Saintonge et al. (2016) μ_{gas} relation includes the sum of the atomic and molecular gas masses, while the Tacconi et al. (2018) relation includes only molecular gas (see Section 5.5 for further discussion). With these assumptions, we invert Equation (11) and solve for ζ_{out} for the stacked spectra, where α is calculated according to slopes of the best-fit MZR and assumed $\mu_{\text{gas}}(M_*)$ at each redshift. This calculation allows us to examine the implications of the observed MZR for metal loss via outflows.

The derived values of ζ_{out} versus M_* are shown in the top panel of Figure 12. The displayed errors on ζ_{out} take into account the measurement uncertainty in O/H but do not include systematic uncertainty associated with the μ_{gas} scaling relations. The uncertainties in μ_{gas} for the $z \sim 0$ bins of Saintonge et al. (2016) result in an uncertainty in our derived $z \sim 0$ ζ_{out} values of <0.01 dex and are thus negligible. The μ_{gas} relation of Tacconi et al. (2018) has an error budget that is dominated by the uncertainty in the normalization of 0.15 dex, corresponding to a 1σ systematic uncertainty of 0.06 dex in ζ_{out} at $z \sim 2.3$ and $z \sim 3.3$. We have not included this uncertainty in the errors shown in Figure 12 because it would shift the $z \sim 2.3$ and $z \sim 3.3$ ζ_{out} values relative to $z \sim 0$ while keeping the offset between the $z \sim 2.3$ and $z \sim 3.3$ points the same. The uncertainty associated with the redshift and M_* dependence

²⁰ $R=0.25\text{--}0.45$ for standard IMFs (Vincenzo et al. 2016). In practice, the derived ζ_{out} is not sensitive to R over this range.

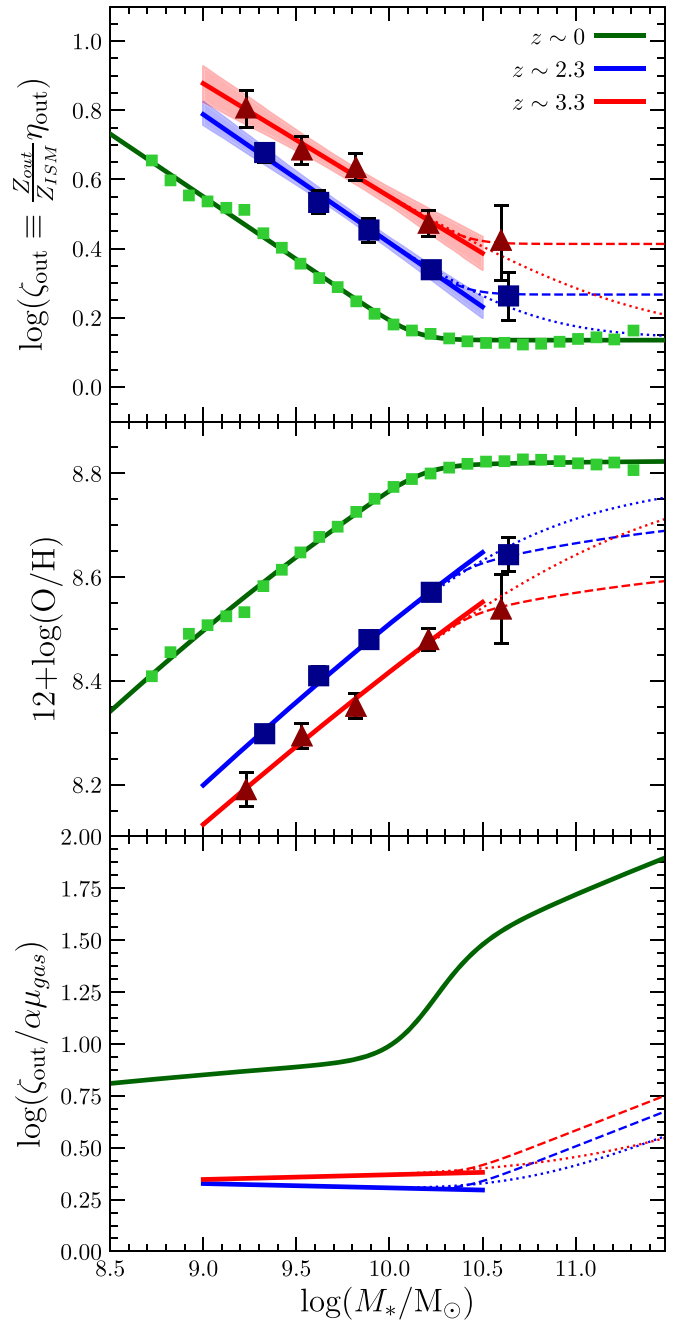


Figure 12. Top: outflow metal loading factor, ζ_{out} , vs. M_* for stacks of star-forming galaxies at $z \sim 0$ (green squares), $z \sim 2.3$ (blue squares), and $z \sim 3.3$ (red triangles). Best-fit relations are shown and given in Equations (15) and (16) for $z \sim 2.3$ and $z \sim 3.3$, respectively. The dashed line shows an extrapolation to high masses assuming ζ_{out} at $z=2.3\text{--}3.3$ turns over as quickly as the $z \sim 0$ relation, while the dotted line displays an extrapolation assuming ζ_{out} asymptotes to the same $\zeta_{\text{out},0}$ as the $z \sim 0$ sample. Middle: MZR at $z=0\text{--}3.3$, where the lines show the MZR inferred by applying the best-fit $\zeta_{\text{out}}(M_*)$ and assumed $\mu_{\text{gas}}(M_*)$ relations in Equation (11), which match the observations by design. Bottom: ratio of ζ_{out} to $\alpha\mu_{\text{gas}}$ at $z \sim 0$, $z \sim 2.3$, and $z \sim 3.3$. When $\log(\zeta_{\text{out}}/\alpha\mu_{\text{gas}}) > 0$, the scaling of outflow efficiency with M_* is more important for shaping the MZR than the scaling of gas fraction with M_* .

of the Tacconi et al. (2018) relation has a much smaller effect on our inferred ζ_{out} values.

At all redshifts, we find that ζ_{out} decreases with increasing M_* , with a significant flattening at high M_* present at $z \sim 0$. At fixed M_* , ζ_{out} increases with increasing redshift. We fit the $z \sim 2.3$ and $z \sim 3.3$ stacks (excluding the highest-mass bin)

with power laws, obtaining

$$z \sim 2.3: \log(\zeta_{\text{out}}) = (-0.37 \pm 0.04) \times m_{10} + (0.42 \pm 0.02) \quad (15)$$

$$z \sim 3.3: \log(\zeta_{\text{out}}) = (-0.33 \pm 0.06) \times m_{10} + (0.55 \pm 0.02) \quad (16)$$

where $m_{10} = \log(M_*/10^{10} M_\odot)$.

We fit ζ_{out} at $z \sim 0$ with a smoothly broken power law of the form

$$\log(\zeta_{\text{out}}) = \log(\zeta_{\text{out},0}) - \gamma/\Delta \times \log \left[1 + \left(\frac{M_*}{M_{\text{TO}}} \right)^{-\Delta} \right]. \quad (17)$$

The best-fit parameters to the $z \sim 0$ data are $[\log(\zeta_{\text{out},0}), \gamma, \log(M_{\text{TO}}/M_\odot), \Delta] = [0.14 \pm 0.01, -0.36 \pm 0.01, 10.14 \pm 0.03, 5.17 \pm 2.82]$. Similar to the best-fit MZR, we find that the best-fit $\zeta_{\text{out}}(M_*)$ displays a consistent slope across all three redshifts, with $\gamma = -0.36 \pm 0.01, -0.37 \pm 0.04$, and -0.33 ± 0.06 at $z \sim 0, 2.3$, and 3.3 , respectively. Taking the average of these slopes yields a universal scaling of $\zeta_{\text{out}} \propto M_*^{-0.35 \pm 0.02}$.

Outflow mass and metal loading factors are often expressed as a function of the circular velocity, v_{circ} , which is more closely related to the gravitational potential than M_* . Using the technique described in PS11 and the stellar mass–halo mass relation of Moster et al. (2013) yields $\zeta_{\text{out}} \propto v_{\text{circ}}^{-1.96 \pm 0.01}$ at $z \sim 0$, $\zeta_{\text{out}} \propto v_{\text{circ}}^{-1.82 \pm 0.17}$ at $z \sim 2.3$, and $\zeta_{\text{out}} \propto v_{\text{circ}}^{-1.59 \pm 0.15}$ at $z \sim 3.3$. If we instead resample our average result of $\zeta_{\text{out}} \propto M_*^{-0.35 \pm 0.02}$ into v_{circ} using a stellar-mass Tully–Fisher relation (sTFR) of $M_* \propto v_{\text{circ}}^{3.75}$ (Lelli et al. 2016), then we find $\zeta_{\text{out}} \propto v_{\text{circ}}^{-1.31 \pm 0.08}$, assuming the sTFR slope does not evolve. The evolution of the sTFR zero point leads to a larger evolution in ζ_{out} at fixed v_{circ} than at fixed M_* . As demonstrated here, the inferred dependence of ζ_{out} on v_{circ} depends on the method used to translate M_* into v_{circ} .

The middle panel of Figure 12 displays the model MZR (solid lines) resulting from applying the assumed μ_{gas} and best-fit ζ_{out} relations in Equation (11), which match the observations by design because we have derived ζ_{out} from the observed metallicities. While we cannot constrain whether ζ_{out} flattens at high masses at $z \sim 2.3$ and $z \sim 3.3$, we show for demonstration purposes two examples where ζ_{out} turns over quickly such that $\zeta_{\text{out},0}$ evolves with redshift (dashed line) or ζ_{out} asymptotes to the same value of $\zeta_{\text{out},0}$ as at $z \sim 0$ (dotted line).

5.2. What Sets the Slope of the MZR at $z \sim 0, 2.3$, and 3.3 ?

We first address the question of what process governs the slope of the MZR at each redshift. According to Equation (11), if ζ_{in} is negligible, the functional form of the MZR is primarily set by the scaling of either ζ_{out} or μ_{gas} with M_* , representing cases where lower-mass galaxies have lower metallicities because metals are more efficiently removed from low- M_* galaxies by outflows or the high gas fractions of low- M_* galaxies lead to stronger dilution of metals in the ISM. If $\zeta_{\text{out}} \gg \alpha\mu_{\text{gas}}$, then metal-enriched outflows determine the slope of the MZR, and the low-mass behavior of the MZR is approximately $\text{O}/\text{H} \propto \zeta_{\text{out}}^{-1}$. If $\alpha\mu_{\text{gas}} \gg \zeta_{\text{out}}$, then the MZR is shaped by changing gas fractions and the low-mass slope is instead $\text{O}/\text{H} \propto \mu_{\text{gas}}^{-1}$. If $\alpha\mu_{\text{gas}}$ and ζ_{out} are approximately equal, then both outflows and gas fractions

contribute significantly to the functional dependence of Z_{ISM} on M_* .

The lower panel of Figure 12 presents $\log(\zeta_{\text{out}}/\alpha\mu_{\text{gas}})$ versus M_* . We find that $\zeta_{\text{out}} \gg \alpha\mu_{\text{gas}}$ at $z \sim 0$ across $\log(M_*/M_\odot) \sim 8.5\text{--}11.5$, indicating that the slope of the local MZR is set by the action of metal-enriched outflows, whereby metals are more efficiently removed from low-mass galaxies. The dominance of outflows at $z \sim 0$ arises because the gas fractions are not large enough to drive the metallicities sufficiently low with our assumed oxygen yield (or indeed for any y_{O} in the range produced by standard IMFs, $y_{\text{O}} = 0.008\text{--}0.045$). PS11 reached the same conclusion for the $z \sim 0$ MZR, and many previous analyses have also concluded that outflows primarily shape the local MZR while gas fractions have a negligible effect (e.g., Tremonti et al. 2004; Dalcanton 2007; Lilly et al. 2013; Chisholm et al. 2018). Because gas fractions are especially low in $z \sim 0$ high-mass galaxies, the flattening of the local MZR at high masses ($M_* \gtrsim 10^{10.2} M_\odot$) requires $\zeta_{\text{out}}(M_*)$ to flatten to an asymptotic value at high M_* as seen in the top panel of Figure 12, implying that there is a lower boundary to the global metal removal efficiency of star formation driven outflows that is only reached at high mass at $z \sim 0$.

At high redshifts, we find that $\zeta_{\text{out}}/\alpha\mu_{\text{gas}}$ is approximately constant over the range of M_* probed by the samples, with $\zeta_{\text{out}} \approx 2\text{--}3 \times \alpha\mu_{\text{gas}}$, with no significant difference between $z \sim 2.3$ and $z \sim 3.3$ when considering the uncertainties in ζ_{out} and μ_{gas} . We thus find that outflows remain the dominant mechanism that sets the MZR slope at $z \sim 2.3$ and $z \sim 3.3$. While the gas fraction carries more relative importance at high redshifts than at $z \sim 0$ due to the increase in μ_{gas} at fixed M_* with increasing redshift, it still has only a minor effect on the MZR slope. While keeping the normalization fixed at $10^{10} M_\odot$, changing the power-law slope of $\mu_{\text{gas}}(M_*)$ by ± 0.1 results in a change of the model MZR slope of only ± 0.02 at $z \sim 2.3$ and $z \sim 3.3$. Thus, in this model, the reason why the slope of the MZR does not significantly change with redshift is because the slope of $\zeta_{\text{out}}(M_*)$ does not significantly change with redshift. The scaling of ζ_{out} with M_* appears to be redshift invariant out to at least $z \sim 3.3$, resulting in a constant low-mass MZR slope over the past 12 Gyr.

It is perhaps not surprising that the same mechanism sets the MZR slope in all three samples because the observed MZR slope is tightly constrained to be the same over $z = 0\text{--}3.3$ with good precision. If the parameter governing the MZR slope transitions from ζ_{out} to μ_{gas} at some higher redshift, we expect to also observe a shift in the MZR slope unless ζ_{out} and μ_{gas} have the same scaling with M_* .

5.3. What Drives the Evolution of the MZR Normalization Over $z = 0\text{--}3.3$?

We now turn to the question of what process drives the evolution of the MZR normalization, leading to decreasing O/H at fixed M_* with increasing redshift. Gas fractions are observed to increase significantly at fixed M_* with increasing redshift, with a scaling of $\mu_{\text{gas}} \sim (1+z)^{1.5}$ (e.g., Tacconi et al. 2013, 2018; Scoville et al. 2017; Liu et al. 2019). One possibility is thus that the evolution of the MZR normalization is caused by the underlying evolution in gas fractions, such that ISM metals are more heavily diluted at fixed M_* with increasing redshift. However, we have shown above that ζ_{out} also increases at fixed M_* with increasing redshift (Figure 12),

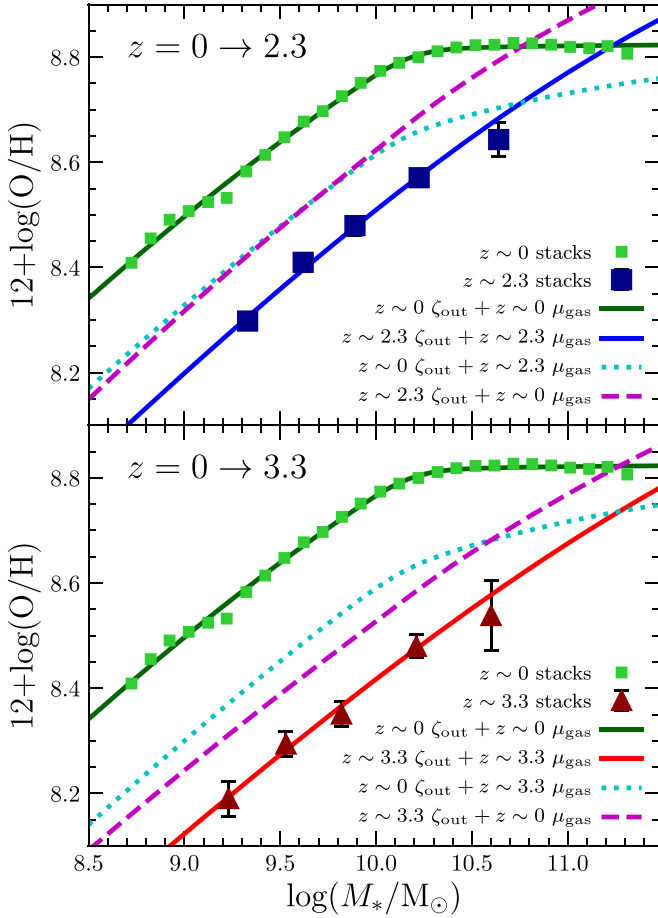


Figure 13. Models of MZR evolution from $z \sim 0$ to $z \sim 2.3$ (top) and $z \sim 3.3$ (bottom), where the effects of evolving μ_{gas} and ζ_{out} have been separated. The solid lines represent our best-fit models at each redshift. The cyan dotted line shows a model assuming the best-fit $z \sim 0$ ζ_{out} and $\mu_{\text{gas}}(M_*)$ of $z \sim 2.3$ (3.3), isolating the contribution of evolving gas fractions to MZR evolution. The magenta dashed line instead displays a model in which the high-redshift $\zeta_{\text{out}}(M_*)$ is assumed while adopting $z \sim 0$ gas fractions, isolating the impact of ζ_{out} evolution on MZR evolution. Evolving μ_{gas} and ζ_{out} each account for roughly half of the observed evolution in O/H at fixed M_* over $z = 0$ – 3.3 .

such that more efficient removal of metals by outflows may be the cause of lower metallicities at high redshifts.

In Figure 13, we show the relative importance of evolving μ_{gas} and ζ_{out} to the total MZR evolution between $z \sim 0$ and $z \sim 2.3$ (top panel) or $z \sim 3.3$ (bottom panel). In each panel, the dotted line shows the resulting MZR from a model with the best-fit $z \sim 0$ $\zeta_{\text{out}}(M_*)$ and high-redshift $\mu_{\text{gas}}(M_*)$ (i.e., only evolving the gas fraction with redshift), while the dashed line shows the MZR modeled with the best-fit high-redshift $\zeta_{\text{out}}(M_*)$ and $z \sim 0$ $\mu_{\text{gas}}(M_*)$ (i.e., only evolving the outflow metal loading factor with redshift). We find that models evolving only ζ_{out} or only μ_{gas} from $z \sim 0$ yield metallicities that are ~ 0.1 – 0.15 dex higher at fixed M_* than the observed MZR at $z \sim 2.3$ and 3.3 , indicating that MZR evolution is not predominantly driven by evolution in either parameter alone. Instead, evolution toward higher μ_{gas} and higher ζ_{out} contribute roughly equally to the decreasing normalization of the MZR with increasing redshift. This result indicates that high-redshift galaxies have lower metallicities than local galaxies at fixed M_* because metals are more diluted due to their higher gas content and metals are more efficiently removed from the ISM by

outflows. Both mechanisms remain important to MZR evolution out to $z \sim 3.3$.

In Section 5.2, we showed that the slope of the MZR is primarily set by the functional form of $\zeta_{\text{out}}(M_*)$ for samples at all three redshifts. A natural question is how μ_{gas} can be important to MZR normalization evolution when it has a subdominant effect on the slope at a given redshift. At fixed $\log(M_*/M_\odot) = 10.0$, the outflow metal loading factor is $\log(\zeta_{\text{out}}) = 0.20 \pm 0.01$, 0.43 ± 0.05 , and 0.56 ± 0.05 at $z \sim 0$, 2.3 , and 3.3 , respectively. Thus, we find that $d\log(\zeta_{\text{out}})/dz = 0.10 \pm 0.03$ at fixed M_* , or roughly $\zeta_{\text{out}} \sim (1+z)^{0.5}$. This evolution of ζ_{out} is weaker than that of $\mu_{\text{gas}} \sim (1+z)^{1.5}$ at fixed M_* (Tacconi et al. 2018). While ζ_{out} carries more weight at fixed redshift than μ_{gas} , the relative importance of μ_{gas} for setting Z_{ISM} grows with increasing redshift, as reflected by the lower $\zeta_{\text{out}}/\alpha\mu_{\text{gas}}$ at $z \sim 2.3$ – 3.3 in the bottom panel of Figure 12. If μ_{gas} and ζ_{out} continue to evolve at these rates out to $z > 4$, it implies that dilution of metals according to μ_{gas} will become the dominant mechanism that controls the MZR slope and normalization at $z \gtrsim 5$ – 6 . Rest-optical spectroscopy of $z > 4$ galaxies from JWST will enable the characterization of the MZR at these redshifts and test whether there is indeed a shift in the dominant physical mechanism.

5.4. Can Accreted Metals Be Ignored?

In the models above, we have assumed that the metal loading of inflows, ζ_{in} , is negligible compared to ζ_{out} . This may not be true because some fraction of outflowing metals is believed to be reaccreted through galactic fountain (Oppenheimer & Davé 2008; Ford et al. 2014; Anglés-Alcázar et al. 2017; Muratov et al. 2017), and a significant amount of metals resides in the CGM (Steidel et al. 2010; Peebles et al. 2014; Rudie et al. 2019). In the PS11 framework, the inflow and outflow mass-loading factors are related according to the expression

$$\eta_{\text{in}} - \eta_{\text{out}} = (1 - R)\mu_{\text{gas}} \left(1 - \frac{d \log \mu_{\text{gas}}}{d \log M_*} \right) - R + 1. \quad (18)$$

For reasonable ranges of the return fraction ($R \sim 0.25$ – 0.45) and the range of power-law slopes of $\mu_{\text{gas}} (\sim 0.3$ – $0.5)$, and over the entire mass range at $z \sim 0$ and above $\sim 10^{9.5} M_\odot$ at $z \sim 2$ – 3 , all terms on the right-hand side are of order unity. In the scenario where outflow mass is predominantly entrained ISM such that $Z_{\text{out}} \approx Z_{\text{ISM}}$, η_{out} is always greater than 1 based on the constraints on ζ_{out} presented in this work. Accordingly, $\eta_{\text{in}} \approx \eta_{\text{out}}$ to first order and the relative importance of ζ_{in} compared to that of ζ_{out} is simply determined by the ratio $Z_{\text{in}}/Z_{\text{out}}$. Thus, if $Z_{\text{in}} \ll Z_{\text{out}}$, then ζ_{in} can be safely ignored.

In general, including accreted metals increases the inferred ζ_{out} and would thus strengthen our conclusion that the slope of the MZR is set by metal-enriched outflows (not by gas fractions) and increase the relative importance of ζ_{out} to the evolving MZR normalization. However, if ζ_{in} increases significantly at fixed M_* toward lower redshifts, then part of the MZR evolution could be explained by the changing importance of accreted metals. Indeed, an increase in $Z_{\text{in}}/Z_{\text{ISM}}$ with decreasing redshift was found to be the primary driver of MZR evolution in the models of Davé et al. (2011); this effect can be understood as a result of gas recycling via galactic fountains.

With a large-enough evolution of $Z_{\text{in}}/Z_{\text{ISM}}$, it is possible that the observed MZR evolution can be explained without any change in ζ_{out} with redshift. This scenario requires a rough scaling of $(1 - Z_{\text{in}}/Z_{\text{ISM}}) \propto (1+z)^{0.5}$. Assuming accreted

gas is nearly pristine at $z \sim 3.3$ (i.e., $Z_{\text{in}}/Z_{\text{ISM}} \approx 0$), this scaling predicts $Z_{\text{in}}/Z_{\text{ISM}} \approx 0.5$ at $z=0$, a lower limit because accretion at high redshift may not be pristine due to vigorous outflow recycling (e.g., Anglés-Alcázar et al. 2017). Detections of Mg II absorption in gas thought to be inflowing onto $z \approx 0.2$ galaxies suggests that low-redshift accreting gas is metal enriched at some level (Ho et al. 2017; Martin et al. 2019). High-velocity H I clouds around the Milky Way that are thought to be accreting onto the Galaxy have typical metallicities of $\sim 0.1 Z_{\text{ISM}}$ (Sancisi et al. 2008). If $Z_{\text{in}}/Z_{\text{ISM}} \approx 0.1$ is typical at $z=0$, then accreted metals cannot play a major role in MZR evolution.

We conclude that the observed evolution of the MZR over $z=0-3.3$ is well explained by the redshift evolution of both the outflow metal loading factor and gas fraction at fixed M_* , but a significant effect from accreting metals cannot be ruled out. There are currently insufficient observational constraints on the metallicity of accreting gas to stringently distinguish the influence that metal accretion has on metallicity scaling relations. Constraints on the recycling timescales and importance of galactic fountains relative to IGM accretion are needed to evaluate the contribution of accreted metals to MZR evolution.

5.5. Systematic Effects of the Assumed Gas Fractions

The scaling of total gas mass ($M_{\text{gas}} = M_{\text{H I}} + M_{\text{H}_2}$) of local star-forming galaxies with M_* and SFR is well characterized through extensive H I 21 cm and CO emission surveys (e.g., Bothwell et al. 2014; Ciccone et al. 2017; Saintonge et al. 2017; Catinella et al. 2018). The gas fractions at $z \sim 0$ thus are not a source of significant systematic uncertainty in our models due to these robust empirical constraints.

The scaling of μ_{gas} with M_* is much more uncertain at high redshifts due to uncertainties in factors that convert CO or dust continuum measurements to molecular gas masses: α_{CO} and the dust-to-gas ratio, both of which are metallicity dependent and may evolve; the CO excitation ladder; and dust temperature. With current facilities, samples are limited to massive galaxies ($\log(M_*/M_\odot) \gtrsim 10.0$) at $z > 1$ and thus do not span a wide dynamic range in mass. Furthermore, the contribution by neutral hydrogen is unknown at high redshift, though there is observational evidence that H I is not the dominant gas component at high redshift (see Tacconi et al. 2018 and references therein), unlike in the local universe where $M_{\text{H I}}/M_{\text{H}_2} = 3-10$ for $z \sim 0$ star-forming galaxies (Saintonge et al. 2016, 2017; Catinella et al. 2018). Accordingly, the total gas mass is taken to be equivalent to M_{H_2} at high redshift. Below, we test high-redshift μ_{gas} scaling relations from the literature against observations of our $z \sim 2.3$ and $z \sim 3.3$ samples, where M_{gas} has been estimated using the Kennicutt-Schmidt (KS; Schmidt 1959; Kennicutt 1998) relation.

We estimate M_{gas} for the high-redshift samples using dust-corrected SFR($\text{H}\alpha$), rest-optical effective radii (R_{eff}) from the catalog of van der Wel et al. (2014), and the $z \sim 1.5$ molecular KS relation of Tacconi et al. (2013) derived from high-redshift CO measurements. We assume $M_{\text{gas}} = M_{\text{H}_2}$ at $z > 1$. The median R_{eff} of galaxies in each M_* bin was used in the calculation for the stacks. The left panels of Figure 14 display μ_{gas} for the $z \sim 2.3$ and $z \sim 3.3$ galaxies and stacks. The blue and red solid lines show the relations resulting from combining our best-fit SFR- M_* relations (Equations (3) and (4)) with the

$R_{\text{eff}}(M_*, z)$ relation of van der Wel et al. (2014), of the form

$$z \sim 2.3: \log(\mu_{\text{gas}}) = -0.25 m_{10} + 0.31, \quad (19)$$

$$z \sim 3.3: \log(\mu_{\text{gas}}) = -0.27 m_{10} + 0.50, \quad (20)$$

where $m_{10} = \log(M_*/10^{10} M_\odot)$. If we were to use the $z=0$ molecular KS relation instead, we would infer μ_{gas} values that are ~ 0.3 dex higher at fixed M_* .

In the right panels of Figure 14, we compare to gas fraction scaling relations of $\mu_{\text{gas}}(M_*, z)$ for main-sequence galaxies from the literature (Scoville et al. 2017; Tacconi et al. 2018; Liu et al. 2019). The scaling relation of Tacconi et al. (2018), employed in our fiducial model, is in closest agreement with our estimates at $z \sim 2.3$ and $z \sim 3.3$ using the KS relation across the full mass range of our samples.²¹ Accordingly, there is no significant change in our results if we instead use the KS relation gas fractions for the $z \sim 2.3$ and $z \sim 3.3$ stacks.

Both the Scoville et al. (2017) and Liu et al. (2019) relations are steep (power-law slope of -0.7) such that the gas fractions are extremely high at low masses, leading to a large disagreement with the KS μ_{gas} values at $\log(M_*/M_\odot) \lesssim 10.0$. In contrast to our fiducial case, models using these $\mu_{\text{gas}}(M_*)$ relations yield a constant ζ_{out} with no M_* dependence, and the MZR slope and normalization are predominantly set by the gas fractions due to the steep slope and high normalization of $\mu_{\text{gas}}(M_*)$. However, such steep $\mu_{\text{gas}}(M_*)$ relations are not observed in numerical simulations across this mass and redshift range, which have power-law slopes of ~ -0.2 to -0.5 (Lagos et al. 2016; Davé et al. 2019; Torrey et al. 2019). As mentioned earlier, CO and dust continuum samples at $z > 1$ are entirely composed of galaxies at $\log(M_*/M_\odot) \gtrsim 10.0$, with the majority at $\log(M_*/M_\odot) > 10.5$. We thus rely on extrapolations to compare to the low-mass half of our high-redshift samples. The extreme gas fractions predicted at low masses by Scoville et al. (2017) and Liu et al. (2019) suggest that extrapolations of these relations below $10^{10} M_\odot$ are not reliable.

Because the high-redshift μ_{gas} does not include neutral hydrogen, it is possible that the true gas fractions at $z \sim 2.3-3.3$ are larger than our estimates. However, dynamical mass constraints do not allow for a large H I contribution at $z \sim 2$. Price et al. (2016) found that the median ratio of the dynamical and stellar masses for $z = 1.4-2.6$ MOSDEF star-forming galaxies is 0.36 dex, such that the typical μ_{gas} can be at most 2–2.5. Wuyts et al. (2016) found a similar dynamical-to-stellar mass ratio at $z \sim 2$ using data from the KMOS^{3D} survey. At $z \sim 2.3$ and $10^{10.0} M_\odot$ (the median mass of our stacking sample), the typical molecular gas fraction using either the KS relation or the Tacconi et al. (2018) scaling relation is 2.0. Accordingly, H I can make up at most $\sim 20\%$ of the total gas mass on average, assuming dark matter is negligible within the baryonic disk. Our results do not change significantly unless gas masses are $\gtrsim 40\%$ ($\gtrsim 0.15$ dex) higher at fixed M_* compared to our fiducial case.

²¹ Note that the Tacconi et al. (2018) scaling relation is not independent of the data set used to calibrate the Tacconi et al. (2013) $z \sim 1.5$ KS relation because the PHIBSS1 CO measurements are included in Tacconi et al. (2018). However, the Tacconi et al. (2013) CO measurements make up $< 25\%$ of the $z > 1$ sample used by Tacconi et al. (2018), such that the agreement of the Tacconi et al. (2018) relation with our KS-based gas fractions is not entirely by construction.

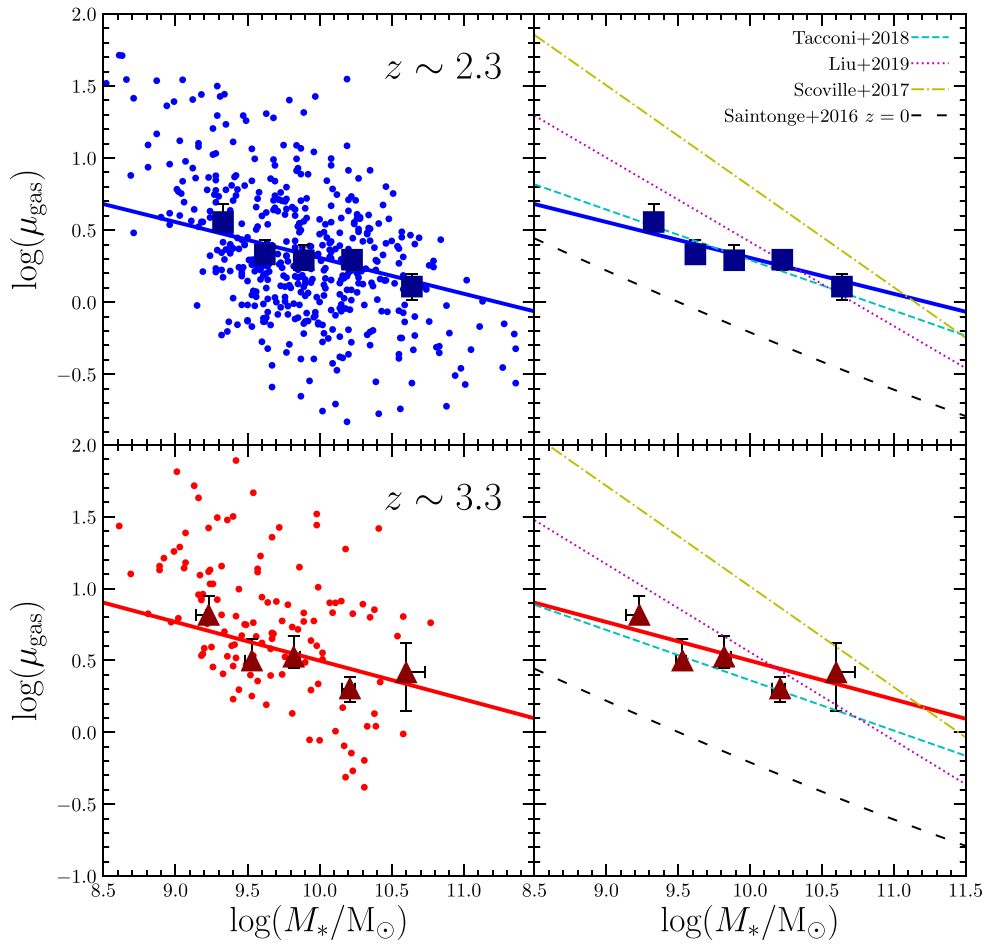


Figure 14. Gas fraction versus M_* for $z \sim 2.3$ (top) and $z \sim 3.3$ (bottom). Left: gas fraction for individual galaxies and stacked spectra (small circles and large squares/triangles, respectively) where the gas fraction has been estimated using the SFR from dust-corrected Balmer lines, rest-optical effective radii (van der Wel et al. 2014), and the $z \sim 1.5$ KS relation of Tacconi et al. (2013). The solid blue (red) line denotes $\mu_{\text{gas}}(M_*)$ found by combining our best-fit SFR– M_* relation at $z \sim 2.3$ (3.3) with the $R_{\text{eff}}(M_*, z)$ relation of van der Wel et al. (2014) and the Tacconi et al. (2013) $z \sim 1.5$ KS relation. The resulting $\mu_{\text{gas}}(M_*)$ relations are given in Equations (19) and 20. Right: comparison of the stacks and $\mu_{\text{gas}}(M_*)$ relations from the left panels to μ_{gas} scaling relations from the literature. The relations of Tacconi et al. (2018, cyan dashed line), Liu et al. (2019, purple dotted line), and Scoville et al. (2017, yellow dashed–dotted line) evaluated for main-sequence galaxies at $z = 2.3$ and $z = 3.3$ are shown. The $z = 0$ $\mu_{\text{gas}}(M_*)$ relation from Saintonge et al. (2016) for main-sequence galaxies is presented as the loosely dashed black line.

5.6. Systematic Effects of the Assumed Stellar Yield

We now address how assumptions about stellar yield affect our conclusions about ζ_{out} and the mechanisms controlling the slope and evolution of the MZR. We have assumed the oxygen yield is $y_{\text{O}} = 0.015$ ($12 + \log(\text{O}/\text{H})_{\text{y}} = 9.2$), appropriate for a Salpeter (1955) IMF with a $100 M_{\odot}$ high-mass cutoff. However, the yield depends strongly on the IMF: the oxygen yields assuming the IMF of Salpeter (1955), Kroupa et al. (1993), Kroupa (2001), or Chabrier (2003) span $y_{\text{O}} = 0.008 - 0.035$ ($12 + \log(\text{O}/\text{H})_{\text{y}} = 9.0 - 9.6$; Vincenzo et al. 2016). If the yield is higher than our assumed value (i.e., $y_{\text{O}} \approx 0.030 - 0.035$ for a Chabrier 2003 or Kroupa 2001 IMF), then the inferred $\zeta_{\text{out}}(M_*)$ would be larger at fixed M_* than in our fiducial model but with a similar slope. In this high-yield case, our conclusion that metal-enriched outflows set the slope of the MZR would be strengthened ($\zeta_{\text{out}}/\alpha \mu_{\text{gas}}$ would be larger at all redshifts), while the evolution of ζ_{out} at fixed M_* would be the dominant driver of MZR evolution, in contrast to our fiducial model in which ζ_{out} and μ_{gas} contribute roughly equally to MZR evolution. If we instead assume the lowest yield for a standard IMF ($y_{\text{O}} = 0.008$ for the Kroupa et al. 1993 IMF), ζ_{out} would be lower at each redshift such that gas fractions have an increased relative importance. In the low-yield case, ζ_{out} still dominates the MZR slope at $z \sim 0$, ζ_{out} and μ_{gas} contribute equally

to the MZR slope at $z \sim 2.3$ – 3.3 , and MZR evolution is primarily driven by evolving gas fractions at fixed M_* .

We have assumed that the stellar yield is redshift invariant, but it is possible that the oxygen yield evolves. In particular, the yield will evolve if the high-mass slope and/or upper mass cutoff of the IMF changes with redshift such that decreasing the slope or increasing the cutoff mass increases y_{O} . There are theoretical expectations that the IMF may have both a higher upper mass cutoff and shallower high-mass slope in low-metallicity and high-SFR environments (Jeřábková et al. 2018; Schneider et al. 2018; Gutcke & Springel 2019), suggesting that oxygen yield increases with redshift due to the evolution of the MZR and the SFR– M_* relation. If oxygen yields are higher at high redshifts than at $z \sim 0$, then a larger ζ_{out} is required at $z \sim 2.3$ – 3.3 to drive metallicities down toward the observed values compared to our fiducial model. Consequently, ζ_{out} becomes even more dominant over μ_{gas} in setting the high-redshift MZR slope, and ζ_{out} would be the dominant driver of MZR evolution. A scenario in which yields decrease with increasing redshift is not expected.

Observational constraints on the high-mass IMF at $z > 1$ are needed to improve chemical evolution models of early galaxies. The non-ionizing rest-UV contains features that are

sensitive to the high-mass slope and upper mass cutoff of the IMF, including stellar wind features such as N V and C IV and nebular emission features such as He II that are sensitive to ionization from the most massive stars (Steidel et al. 2016; Sencynha et al. 2017). A systematic analysis of such IMF-sensitive rest-UV features for large samples at $z \sim 2\text{--}3$ could determine whether the high-mass IMF changes appreciably at high redshift and thus reduce uncertainties in stellar yields at $z > 1$.

6. Discussion

6.1. Comparison to Past Studies

6.1.1. Past Studies of the MZR at $z \sim 2.3$

Our results do not differ drastically from past studies of the MZR at $z \sim 2.3$, with a generally similar slope but smaller evolution in O/H at fixed M_* relative to the local MZR than literature results (Erb et al. 2006a; Wuyts et al. 2012, 2016; Belli et al. 2013; Henry et al. 2013; Kulas et al. 2013; Cullen et al. 2014; Maier et al. 2014; Steidel et al. 2014; Kacprzak et al. 2015, 2016; Sanders et al. 2015, 2018, 2020b; Hunt et al. 2016). The smaller evolution is due to our use of different calibrations at $z \sim 0$ and $z > 1$ to account for evolving ISM conditions. If we apply local calibrations at high redshifts, as has been done by all previous studies, we find a ~ 0.1 dex larger decrease in O/H at fixed M_* (~ -0.33 dex), in agreement with past work.

Using stacked spectra of 87 $z \sim 2.3$ galaxies, Erb et al. (2006a) found a sharp drop off in metallicity between $10^{10.0} M_\odot$ and $10^{9.5} M_\odot$, yielding a low-mass slope much steeper than our value. The steepness of the Erb et al. (2006a) MZR can be attributed to a sample bias where their low-mass bins are populated by galaxies falling up to ~ 1 dex above the $z \sim 2.3$ star-forming main sequence (Cullen et al. 2014), resulting in below-average O/H at low M_* . Our more representative $z \sim 2.3$ sample does not display such a steep low-mass slope.

Steidel et al. (2014) investigated the MZR at $z = 2.3$ using a sample of 242 star-forming galaxies from KBSS, inferring a much flatter MZR than ours, with a low-mass slope of 0.20 ± 0.02 . This shallow MZR could be a result of a bias in the KBSS sample against metal-rich, red, dusty galaxies at high masses. The KBSS sample is primarily rest-UV selected, which could result in such a bias, although it is supplemented with galaxies meant to fill in the high-mass, red star-forming population (Steidel et al. 2014; Strom et al. 2017). In contrast, MOSDEF is rest-optical selected (Kriek et al. 2015). A full comparison of the properties of the MOSDEF and KBSS samples would be useful in elucidating the origin of differing results in both the MZR and [N II] BPT diagram offset at $z \sim 2.3$.

The $z \sim 2.3$ MZR has been measured for MOSDEF data using a range of metallicity indicators and $z \sim 0$ calibrations (Sanders et al. 2015, 2018). Using a simple power-law form, these early studies found the slope of the MZR at $z \sim 2.3$ to be $0.26\text{--}0.34$ depending on the indicator used, generally consistent with the slope in this work (0.30 ± 0.02). Most of the indicators considered were nitrogen-based, but when inferring metallicities from O_{32} , a line ratio that overlaps with this work, Sanders et al. (2018) found an evolution of -0.3 dex in O/H at fixed M_* over $z = 0\text{--}2.3$ at $10^{10} M_\odot$, slightly larger than in the present work. Though the sample in Sanders et al. (2018) has

approximately 80% overlap with the $z \sim 2.3$ sample in this work, the results in this work are more robust because we account for evolving ISM conditions in our choice of metallicity calibrations.

Sanders et al. (2020b) investigated the MZR using a sample of ~ 20 galaxies at $z \sim 2.2$ with direct-method metallicities, finding a low-mass slope of -0.37 ± 0.08 . This value is consistent with our $z \sim 2.3$ slope. It is imperative to increase the number of $z > 1$ galaxies with direct-method metallicities in order to improve constraints on metallicity calibrations appropriate for galaxies in the early universe.

6.1.2. Past Studies of the MZR at $z > 3$

While our results show reasonable agreement with past studies of the $z \sim 2.3$ MZR, we find that they differ significantly from earlier work at $z > 3$. Maiolino et al. (2008), Mannucci et al. (2009), and Troncoso et al. (2014) analyze the AMAZE+LSD sample of 40 galaxies at $z \sim 3.4$, deriving metallicities using the same set of emission lines as in this work ([O II], [Ne III], H β , and [O III]). For both individual galaxies and composite spectra, all three works find a large evolution in O/H at $10^{10} M_\odot$ of ~ -0.7 to -0.8 dex from $z \sim 0$ to $z \sim 3.4$. By comparing to the Erb et al. (2006a) $z \sim 2.3$ MZR, these authors find that the metallicity evolution from $z \sim 2.3$ to $z \sim 3.4$ ($0.3\text{--}0.4$ dex over only 1 Gyr) is as large as the evolution from $z \sim 0$ to $z \sim 2.3$ (0.3 dex over ~ 10 Gyr). These authors interpreted this sharp decrease in metallicity at fixed mass between $z \sim 2.3$ and $z \sim 3.4$ as an indication that the mode of galaxy growth changed rapidly over this short time period. They suggested that either galaxies at $z > 3$ assemble from unevolved subcomponents and chemical enrichment mostly proceeds after merging into larger systems (Maiolino et al. 2008); have significantly larger gas inflow rates (from the IGM or gas-rich mergers) than galaxies at $z \sim 2$, rapidly building up the gas reservoir while driving metallicities down (Mannucci et al. 2009) and potentially indicating a gas accumulation phase where gas flows are out of equilibrium (Davé et al. 2012); or both gas inflow and outflow rates sharply rise from $z \sim 2$ to $z > 3$ while maintaining equilibrium (Troncoso et al. 2014).

Onodera et al. (2016) investigated the MZR at $z \sim 3.3$ using a sample of 41 galaxies at $z = 3.0\text{--}3.7$ with MOSFIRE spectroscopy, and Suzuki et al. (2017) expanded this sample with 10 [O III]-selected galaxies at the same redshifts. Similar to the AMAZE+LSD studies, these authors find that the MZR normalization decreases by 0.7 dex between $z \sim 0$ and $z \sim 3.3$. By applying analytic chemical evolution models (Lilly et al. 2013), Onodera et al. (2016) find the low metallicities at $z > 3$ can be explained by a scenario in which the star formation efficiency ($\epsilon \equiv \text{SFR}/M_{\text{gas}}$) evolves weakly with redshift at fixed M_* , with a nonevolving ϵ providing a reasonable fit to their data.

These interpretations are in tension with recent observations and theoretical expectations. Star formation efficiency (the inverse of the depletion timescale) is observed to increase fairly strongly with increasing redshift as $\epsilon \propto (1+z)^{0.5\text{--}1.0}$ (e.g., Tacconi et al. 2013, 2018; Scoville et al. 2017; Liu et al. 2019), though Genzel et al. (2015) found a weaker $\epsilon \propto (1+z)^{0.34}$ that Onodera et al. (2016) found plausible based on their data. Furthermore, constant or weakly evolving ϵ models underpredict observed metallicities at $z \sim 1.5\text{--}2.5$ and predict stronger SFR dependence in the FMR than is observed at

$z \sim 0$ and $z \sim 2.3$ (Mannucci et al. 2010; Sanders et al. 2018; Curti et al. 2020b). Modern numerical simulations of galaxy formation do not predict a break in the metallicity evolution above $z = 3$ but instead find the MZR evolves smoothly up to very high redshifts ($z \gtrsim 6$) at a rate of $d\log(\text{O}/\text{H})/dz \approx -0.05$ to -0.15 (Okamoto et al. 2014; Ma et al. 2016; Davé et al. 2017; De Rossi et al. 2017; Davé et al. 2019; Torrey et al. 2019), with the evolutionary rate actually slowing at $z \gtrsim 3$ in some cases. In this work, we find an approximately constant evolution at fixed M_* of $d\log(\text{O}/\text{H})/dz = -0.11$ out to $z \sim 3.3$, in close agreement with simulations based on hierarchical galaxy formation and consistent with models where star formation efficiency increases with redshift.

It is of interest to understand why our results differ from earlier MZR studies at $z > 3$. We present a comparison of the sample properties of the MOSDEF, AMAZE+LSD, and Onodera et al. (2016) $z > 3$ samples in Appendix B. Briefly, we find that the AMAZE+LSD and Onodera et al. (2016) samples are not biased in SFR compared to the MOSDEF $z \sim 3.3$ sample, but the AMAZE+LSD sample displays a significant bias toward higher excitation (thus, lower O/H) manifested as higher $[\text{O III}]/\text{H}\beta$ and O_{32} ratios at fixed M_* . The Onodera et al. (2016) sample is not obviously biased in excitation. We have shown that the dust correction methods used in Onodera et al. (2016) based on either β_{UV} or assuming $E(B - V)_{\text{gas}} = E(B - V)_{\text{stars}}$ underestimates the true nebular reddening (see Appendix A), biasing line ratios and leading to lower inferred metallicities. In the stacking method of Onodera et al. (2016), they both normalize spectra by $[\text{O III}]\lambda 5007$ and apply inverse-variance weighting when combining spectra. Including both of these steps gives high-SFR galaxies more weight in the stacked emission lines, which biases the metallicities of stacks low according to the FMR.

A major difference between this work and the analyses of Maiolino et al. (2008), Mannucci et al. (2009), Troncoso et al. (2014), and Onodera et al. (2016) is the set of metallicity calibrations used to derive metallicities. All four of these earlier studies use the calibrations of Maiolino et al. (2008) that are based on theoretical photoionization models at high metallicities ($12 + \log(\text{O}/\text{H}) \gtrsim 8.3$) and empirical direct-method metallicities at low metallicities. Theoretical calibrations are known to yield metallicities that are ~ 0.25 dex higher than direct-method calibrations (e.g., Kewley & Ellison 2008). The $z \sim 0$ samples lie almost entirely in the high-metallicity regime calibrated to photoionization models, while the $z > 3$ samples lie in the direct-method calibration regime for the Maiolino et al. (2008) relations. The mixing of theoretical and empirical metallicities in the Maiolino et al. (2008) calibration sample thus artificially introduces ~ 0.25 dex of additional MZR evolution at $z > 3$. In this work, we use calibrations based purely on the direct method at all redshifts.

In Section 4.4, we found that $z = 0$ calibrations underestimate the metallicities of high-redshift galaxies by ~ 0.1 dex. Thus, the use of $z = 0$ calibrations at all redshifts in past studies also contributes to the larger observed evolution over $z = 0 - 3.3$. An additional systematic effect may arise from mixing different metallicity indicators at different redshifts, where in past studies metallicities at $z \lesssim 2.5$ primarily depended on nitrogen-based indicators while metallicities at $z > 3$ are based solely on oxygen-based indicators. The redshift evolution of the star-forming sequence in the BPT diagram suggests that nitrogen- and oxygen-based $z = 0$ calibrations will not

produce consistent metallicities when applied at $z \gtrsim 2$ (Steidel et al. 2014; Sanders et al. 2015; Shapley et al. 2015).

We thus find that earlier studies of the MZR at $z > 3$ were impacted by a combination of effects that bias metallicity low, including biases in sample excitation properties, reddening correction, stacking techniques, and metallicity calibrations. This analysis supersedes these earlier works with a sample that is representative of typical $z \sim 3.3$ galaxies and a factor of 4 times larger, a dust correction method that is more robust, and metallicity derivations that use a uniform set of lines across all redshifts while properly accounting for evolving ISM conditions.

6.1.3. Past Studies of the FMR at $z > 2$

Early investigations of the FMR at high redshifts yielded conflicting results regarding whether O/H secondarily depends on SFR at $z > 1$ and whether the FMR evolves (e.g., Christensen et al. 2012; Wuyts et al. 2012, 2014, 2016; Belli et al. 2013; Henry et al. 2013; Stott et al. 2013; Cullen et al. 2014; Maier et al. 2014; Steidel et al. 2014; Zahid et al. 2014b; Salim et al. 2015; Sanders et al. 2015; Yabe et al. 2015). More recent work based on larger samples and more uniform analyses of metallicity and SFR have demonstrated that O/H does carry a secondary dependence on SFR at fixed M_* at $z \sim 2$ (Sanders et al. 2018) and ruled out a strong evolution of the FMR, with O/H evolving ≤ 0.1 dex at fixed M_* and SFR out to $z \sim 2.5$ (Sanders et al. 2018; Cresci et al. 2019; Curti et al. 2020b). The strength of the SFR dependence in high-redshift samples remains poorly constrained ($\text{O}/\text{H} \propto \text{SFR}^{-0.1 \text{ to } -0.3}$; Sanders et al. 2018), and larger samples spanning a wide dynamic range in sSFR are needed to improve this measurement.

In Sanders et al. (2015, 2018), we found that $z \sim 2.3$ galaxies have ~ 0.1 dex lower O/H compared to $z \sim 0$ galaxies matched in M_* and SFR. We used local metallicity calibrations for both the low- and high-redshift samples in those works. In the present analysis, we now use an appropriate calibration at $z > 2$ that yields $\sim 0.05 - 0.1$ dex higher metallicities than local calibrations (Section 4.4), effectively eliminating the 0.1 dex offset from the $z = 0$ FMR observed in earlier MOSDEF studies. We now find excellent agreement with the $z \sim 0$ FMR out to $z \sim 3.3$, with $\Delta\log(\text{O}/\text{H}) < 0.04$ dex on average. While earlier works found that $z > 3$ galaxies fell $\sim 0.3 - 0.6$ dex below the local FMR (Mannucci et al. 2010; Troncoso et al. 2014; Onodera et al. 2016), improvements in sample size, representativeness, and metallicity derivation techniques have seen this offset from the FMR at $z > 3$ disappear (see Section 6.1.2).

In Section 4.3, we fit a new parameterization of the $z \sim 0$ FMR using our new direct-method $z \sim 0$ calibrations (Figure 3). Curti et al. (2020b) have recently fit the $z \sim 0$ FMR using SDSS data and the $z \sim 0$ direct-method calibrations of C17. We find that our high-redshift samples do not display significant evolution relative to the $z \sim 0$ total SFR FMR parameterization of Curti et al. (2020b), with both the $z \sim 2.3$ and $z \sim 3.3$ stacks and means of the individual galaxies offset by < 0.05 dex in O/H. Note that this result is based on applying the high-redshift B18 metallicity calibrations to our $z > 2$ samples. If we instead use the $z \sim 0$ C17 calibrations (the same set used by Curti et al. 2020b), we find that the $z > 2$ galaxies are offset ≈ 0.10 dex lower in O/H than the Curti et al. (2020b) FMR. This comparison again emphasizes the importance of accounting for evolving metallicity calibrations when studying MZR and FMR evolution over a wide redshift range. Insofar as

the relation among M_* , SFR, and O/H reflects the interplay of gas flows and star formation, the nonevolution of the FMR suggests that galaxies remain near the equilibrium condition through the smooth baryonic growth process since $z \sim 3.3$.

6.2. The Evolution of the Outflow Mass-loading Factor over $z = 0-3.3$

In Section 5.1, we constrained the mass scaling of the outflow metal loading factor, $\zeta_{\text{out}} \propto M_*^{-0.35 \pm 0.02}$, and found that this scaling holds over $z = 0-3.3$ while the normalization increases with increasing redshift. We now consider the implications for the scaling and normalization of the outflow mass-loading factor, $\eta_{\text{out}} \equiv \dot{M}_{\text{out}}/\text{SFR}$. ζ_{out} is the product of η_{out} and the ratio of the outflow metallicity to that of the ISM ($Z_{\text{out}}/Z_{\text{ISM}}$). If outflows are predominantly composed of entrained ISM material such that swept up ISM gas dominates the outflow mass over pure SNe ejecta, then $Z_{\text{out}}/Z_{\text{ISM}} \approx 1$ and is constant with M_* . Consequently, $\zeta_{\text{out}} \approx \eta_{\text{out}}$. Thus, based on the scaling we found between ζ_{out} and M_* , $\eta_{\text{out}} \propto M_*^{-0.35 \pm 0.02} \sim v_{\text{circ}}^{-1.3 \text{ to } -1.8}$ at all redshifts, $\eta_{\text{out}} > 1$ at all masses and redshifts, the MZR slope is set by $\eta_{\text{out}}(M_*)$ at all redshifts, and MZR evolution is partially driven by an increase in η_{out} at fixed M_* with increasing redshift.

6.2.1. Scaling of η_{out} with M_*

Our inferred $\eta_{\text{out}} \propto M_*^{-0.35 \pm 0.02}$ scaling is in good agreement with observational constraints. Chisholm et al. (2017) find $\eta_{\text{out}} \propto M_*^{-0.43 \pm 0.07}$ and $\eta_{\text{out}} \propto v_{\text{circ}}^{-1.56 \pm 0.25}$ using measurements of rest-UV absorption lines for seven $z = 0$ galaxies spanning $\log(M_*/M_\odot) \sim 7-10.5$. Heckman et al. (2015) find $\eta_{\text{out}} \propto v_{\text{circ}}^{-0.98} (\sim M_*^{-0.3})$ for the “strong outflow” subset of their $z \sim 0$ sample using similar techniques, though their data are consistent with $\eta_{\text{out}} \propto v_{\text{circ}}^{-1 \text{ to } -2} (\sim M_*^{-0.3 \text{ to } -0.6})$ when including the “weak outflow” objects as well.²² Cullen et al. (2019) measured the stellar mass–stellar metallicity relation (MZ_*) for star-forming galaxies at $z \sim 3.5$ (well matched in redshift to our sample at $z \sim 3.3$) and found an MZ_* slope that is similar to that of our $z \sim 3.3$ gas-phase relation. These authors found that models with $\eta_{\text{out}} \propto M_*^{-0.4}$ provide a good fit to the $z \sim 3.5$ MZ_* , consistent with our findings. Leethochawalit et al. (2019) model the MZ_* for quiescent galaxies at $z \sim 0.5$, tracing α elements via $[\text{Mg}/\text{H}]_{\text{stars}}$, and infer $\eta_{\text{out}} \propto M_*^{-0.21 \pm 0.09}$. Förster Schreiber et al. (2019) find $\eta_{\text{out}} \propto M_*^{-0.1 \pm 0.2}$ from broadened emission lines in stacked spectra of 600 galaxies at $z = 0.6-2.7$, consistent with our scaling within the large uncertainty.

We also find good agreement with η_{out} scalings in cosmological hydrodynamic simulations. In the FIRE cosmological zoom-in simulations, Muratov et al. (2015) find $\eta_{\text{out}} \propto M_*^{-0.35 \pm 0.02}$ and $\eta_{\text{out}} \propto v_{\text{circ}}^{-1.0}$. These authors do not find any strong redshift evolution in $\eta_{\text{out}}(M_*)$, but likely would be unable to resolve the weak evolution of $d\log(\eta_{\text{out}})/dz \approx 0.10$ implied by the constant $Z_{\text{out}}/Z_{\text{ISM}}$ scenario because of the small number of low-redshift galaxies in FIRE. Outflow metallicities

probed in FIRE at 25% of the virial radius are found to be a constant near-unity fraction of the ISM metallicity, $Z_{\text{out}} \approx 1.2Z_{\text{ISM}}$ with no M_* dependence (Muratov et al. 2017), in agreement with our assumption that outflows are almost entirely composed of entrained material. In IllustrisTNG, Nelson et al. (2019) find that $\eta_{\text{out}} \approx 50$ at $10^{7.5} M_\odot$ and 4 at $10^{10.5} M_\odot$ for outflowing material with $v_{\text{rad}} > 0 \text{ km s}^{-1}$ at 10 kpc galactocentric radius, implying $\eta_{\text{out}} \propto M_*^{-0.37}$. These authors also find that $Z_{\text{out}} \approx Z_{\text{ISM}}$. Mitchell et al. (2020) find $\eta_{\text{out}} \propto v_{\text{circ}}^{-1.5}$ for stellar feedback in the EAGLE simulations, and $\eta_{\text{out}} \propto M_*^{-0.3 \text{ to } -0.4}$ at $z \sim 2-3$.

6.2.2. Normalization of η_{out}

We showed in Figure 12 that the normalization of $\zeta_{\text{out}}(M_*)$ increases with increasing redshift as $d\log(\zeta_{\text{out}})/dz = 0.10 \pm 0.03$ at fixed M_* , while its slope remains constant over $z = 0-3.3$. With $Z_{\text{out}} \approx Z_{\text{ISM}}$ and $\zeta_{\text{out}} \approx \eta_{\text{out}}$, the outflow mass-loading factor at $10^{10} M_\odot$ ($\eta_{\text{out},10}$) is $\log(\eta_{\text{out},10}) = 0.20 \pm 0.01$ at $z \sim 0$, 0.43 ± 0.05 at $z \sim 2.3$, and 0.56 ± 0.05 at $z \sim 3.3$ in our fiducial model. As discussed in Section 5.6, the normalization of ζ_{out} is sensitive to the assumed stellar yield, which varies by a factor of ~ 2 lower or higher than our assumed value of $y_O = 0.015$ over the range of standard IMFs. Increasing (decreasing) the assumed yield by a factor of 2 results in an increase (decrease) of ζ_{out} normalization by a factor of ~ 3 , such that the systematic uncertainty in our inferred η_{out} values associated with the stellar yield is ± 0.5 dex. Note that changing the yield has no significant effect on the inferred slope of $\zeta_{\text{out}}(M_*)$ or $\eta_{\text{out}}(M_*)$.

The η_{out} normalization above agrees well with results from recent cosmological numerical simulations. Nelson et al. (2019) find $\log(\eta_{\text{out},10}) \approx 0.7$ at $z \sim 0$ in IllustrisTNG. This value is a factor of 3 larger than our $\eta_{\text{out},10}$ at $z \sim 0$, but IllustrisTNG has a higher stellar yield ($y_Z = 0.050$, corresponding to $y_O \approx 0.30-0.35$; Torrey et al. 2019) than we assume by a factor of ~ 2 that accounts for the difference in η_{out} normalization. In the EAGLE simulations, $\log(\eta_{\text{out},10}) \approx 0.1$ at $0.0 < z < 0.3$ and $\log(\eta_{\text{out},10}) \approx 0.35$ at $2.4 < z < 3.4$, in reasonable agreement with our results considering uncertainties in supernova yields (Mitchell et al. 2020). Using cosmological zoom-in simulations, Christensen et al. (2016) find $\log(\eta_{\text{out},10}) \approx 0.2$ with little change over $z = 0-2$, in good agreement with our results at $z \sim 0$ but slightly lower than we find at $z \sim 2.3$. Muratov et al. (2015) find $\log(\eta_{\text{out},10}) = 0.55$ in the FIRE simulations for a sample of galaxies predominantly at $2.0 < z < 4.0$, in excellent agreement with our values at $z \sim 2.3-3.3$.

Studies observationally constraining η_{out} normalization generally find $\eta_{\text{out},10} \sim 0.1-1$ at $z \sim 1-2$ for the low-ionization or warm ionized outflow phases (Martin et al. 2013; Jones et al. 2018; Davies et al. 2019; Förster Schreiber et al. 2019). These values represent lower limits because they are based on measurements of only one phase of the multiphase outflowing gas. As such, these observational constraints are consistent with both our inferred η_{out} normalization and those found in simulations and suggest that mass outflow rates are not orders of magnitude different from galaxy SFRs.

We thus find that our inferred $\eta_{\text{out}}(M_*)$ agrees well with numerical simulations in both normalization and slope (Section 6.2.1). Because the physics of SN energy injection occur on subgrid scales, the IllustrisTNG and EAGLE simulations input mass loading and velocity scalings at injection that depend on v_{circ} or M_* . Both simulations are in reasonable agreement with our results, such that we cannot

²² Outflow properties inferred from observations of low-ionization rest-UV absorption lines or broad rest-optical emission lines only probe the warm ionized phase of outflows, while outflows are thought to additionally comprise neutral, molecular, and hot phases. Comparing η_{out} as inferred from chemical evolution models or numerical simulations to observational constraints on η_{out} for the warm ionized phase implicitly assumes that η_{out} scales similarly with M_* across all outflow phases.

distinguish between their different feedback prescriptions. Out of these simulations, only FIRE (with which we find the closest agreement) has sufficient resolution to implement ISM-scale stellar feedback models including stellar winds, radiation pressure, photoionization and photoelectric heating, and Type Ia and core-collapse SNe such that the loading of outflows is entirely emergent from these physical processes (Hopkins et al. 2014). Our close agreement with FIRE suggests that their simulations capture the most important physical mechanisms for star-formation-driven outflows.

6.2.3. Redshift Evolution of η_{out}

A key feature of our fiducial model is that ζ_{out} , and consequently η_{out} , increases at fixed M_* with increasing redshift. In EAGLE, Mitchell et al. (2020) find that η_{out} increases at fixed M_* with redshift by ~ 0.2 – 0.4 dex between $z \sim 0$ and $2.4 < z < 3.4$, in good agreement with our inferred evolution of $d\log(\eta_{\text{out}})/dz = 0.10 \pm 0.03$. In contrast, η_{out} is constant or slightly declining with redshift at fixed M_* in IllustrisTNG (Nelson et al. 2019). Understanding why EAGLE and IllustrisTNG display this differing behavior in the evolution of η_{out} may yield insight into which subgrid feedback prescriptions are more realistic. Muratov et al. (2015) do not report any redshift dependence of $\eta_{\text{out}}(M_*)$ for FIRE, but likely would not be able to resolve the slow η_{out} evolution that we infer because their sample is primarily made up of simulated galaxies at $2.0 < z < 4.0$ with only a handful of galaxies at $z < 0.5$ to set an evolutionary baseline.

There is empirical evidence that η_{out} may be larger in typical high-redshift galaxies than in $z \sim 0$ galaxies at the same M_* . Observations suggest η_{out} positively correlates with Σ_{SFR} (e.g., Newman et al. 2012; Arribas et al. 2014; Davies et al. 2019), such that $z \sim 2$ – 3 galaxies may have larger η_{out} than similar-mass $z \sim 0$ galaxies because of their ~ 2 orders of magnitude larger Σ_{SFR} (Shapley et al. 2019). Seemingly in conflict with this trend is the finding that η_{out} and SFR are anticorrelated in local samples (e.g., Heckman et al. 2015). However, at fixed redshift, the trend between η_{out} and SFR carries an imprint of the anticorrelation between η_{out} and M_* or v_{circ} due to the SFR– M_* relation. Our model can be explained if instead η_{out} increases with SFR at fixed stellar mass.

To search for this trend, we use samples of $z \sim 0$ galaxies with η_{out} derivations based on rest-UV absorption profiles from Heckman et al. (2015) and Chisholm et al. (2017, 2018). We take η_{out} and SFR(UV) values as tabulated in these sources and calculate the offset in SFR from the $z = 0$ star-forming main sequence, $\Delta\text{SFR}_{\text{MS}(z=0)}$, using the $z = 0$ SFR(UV)– M_* relation of Cook et al. (2014). In Figure 15, we show η_{out} versus offset from the star-forming main sequence for these galaxies. We find a loose but 3σ significant correlation between η_{out} and $\Delta\text{SFR}_{\text{MS}(z=0)}$, with a Spearman correlation coefficient of 0.46 and a p value of 0.003. This trend implies that η_{out} increases with increasing SFR at fixed M_* . Because SFR increases at fixed M_* with increasing redshift, this trend is qualitatively consistent with the results of our modeling.

At fixed M_* in our models, η_{out} increases by 0.23 ± 0.05 dex between $z \sim 0$ and $z \sim 2.3$, and by 0.36 ± 0.05 dex over $z = 0$ – 3.3 . Likewise, at fixed M_* , SFR increases by 1.22 dex and 1.4 dex over these same redshift intervals, respectively (Figure 2 and Equations (2)–(4)). If we operate under the assumption that η_{out} is connected to SFR independent of redshift, our models predict a rough scaling of $\eta_{\text{out}} \propto \Delta\text{SFR}_{\text{MS}(z=0)}^{0.25 \pm 0.05}$, shown by the red line in

Figure 15. This scaling is consistent with binned means of the individual galaxies (black squares). If this relation between η_{out} and SFR at fixed M_* is redshift invariant, then it can explain the increasing normalization of $\zeta_{\text{out}}(M_*)$ and $\eta_{\text{out}}(M_*)$ with increasing redshift. Thus, a redshift-invariant relation between η_{out} and SFR at fixed M_* can explain the increasing normalization of $\zeta_{\text{out}}(M_*)$ and $\eta_{\text{out}}(M_*)$ with increasing redshift.

Theoretical work is required to understand why η_{out} increases with SFR at fixed M_* . One clear difference in the ISM of low- and high-SFR galaxies of the same mass is the gas fraction: $\mu_{\text{gas}} \propto \text{SFR}^{0.5}$ at fixed M_* (e.g., Genzel et al. 2015; Saintonge et al. 2016; Tacconi et al. 2018). A higher η_{out} with increasing $\Delta\text{SFR}_{\text{MS}(z=0)}$ implies that a larger mass of ISM gas is swept into outflows per unit SFR (i.e., per SN) in high-SFR, gas-rich galaxies. This scenario agrees with the analytic theory work of Hayward & Hopkins (2017), in which larger gas fractions correspond to higher mass-loading factors in a turbulent ISM. In their framework, turbulence creates gas patches with a range of surface densities, where low-density patches are more easily blown out of the galaxy by SN feedback to form large-scale outflows. The fraction of the ISM below the critical escape density increases with increasing μ_{gas} , leading to more efficient winds and larger η_{out} at higher gas fractions. For simplicity, we have treated the actions of gas fraction (metal dilution) and outflows (metal removal) as two independent mechanisms, but this theoretical work demonstrates that μ_{gas} and η_{out} (and, in turn, ζ_{out}) are not decoupled but are instead physically linked. This connection is natural because gas content and SFR are tightly linked (e.g., the KS relation; Kennicutt 1998), and star formation is the source of energy injection to drive outflows.

6.3. On the Nonevolution of the FMR

In Section 4.3, we found that the FMR shows no sign of evolving out to $z \sim 3.3$ with good precision (Figure 9). That is, galaxies with the same M_* and SFR have the same O/H on average at all redshifts over $z = 0$ – 3.3 . In our model framework, a simple way to produce a nonevolving FMR is to have $\mu_{\text{gas}}(M_*, \text{SFR})$ and $\eta_{\text{out}}(M_*, \text{SFR})$ be redshift invariant. We can test this scenario by seeing whether $z \sim 0$ galaxies matched in M_* and SFR to $z \sim 2$ galaxies also have gas fractions similar to those of the high-redshift sample. Because we have shown that such a matched set of galaxies have similar O/H, the PS11 theoretical framework then implies that ζ_{out} and, by extension, η_{out} are also the same.

Empirically, gas fraction scales approximately as $\mu_{\text{gas}} \propto \text{SFR}^{0.5}$ at fixed M_* at $z \sim 0$ (Genzel et al. 2015; Saintonge et al. 2016; Tacconi et al. 2018). At fixed M_* , SFR increases by 1.22 dex between $z \sim 0$ and $z \sim 2.3$ (Figure 2). Accordingly, local galaxies matched in M_* and SFR to our $z \sim 2.3$ sample have μ_{gas} that is ~ 0.6 dex higher than that of $z \sim 0$ main-sequence galaxies of the same mass. At $\log(M_*/M_\odot) = 10.5$ (the mass of the $z > 1$ μ_{gas} calibration samples) and for galaxies on the main sequence, the difference in μ_{gas} between $z \sim 2.3$ and $z \sim 0$ is 0.53 dex based on our assumed scaling relations (Figure 14). Thus, galaxies matched in M_* and SFR at both redshifts have similar gas fractions. Because they have nearly the same metallicity, they consequently must have similar η_{out} based on our models.

The theoretical picture of the FMR is usually explained by variations in gas fraction based on gas accretion rates: at fixed M_* , high-SFR galaxies have low metallicities because recent accretion of metal-poor gas has increased the gas fraction and

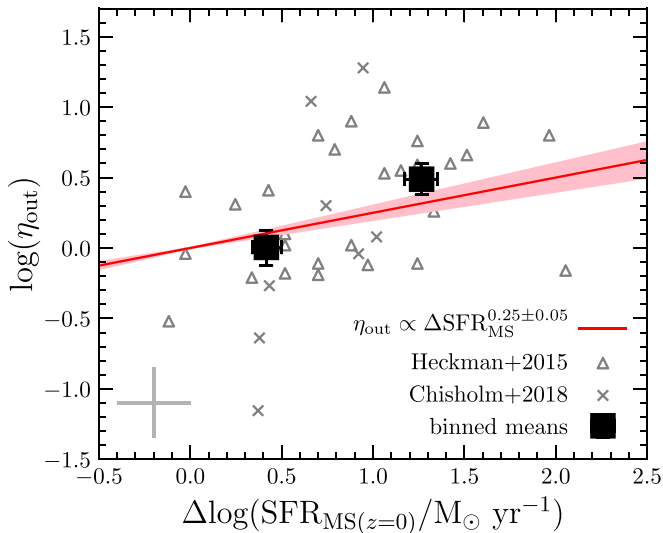


Figure 15. The outflow mass-loading factor as a function of offset from the $z = 0$ star-forming main sequence. Gray points display the $z \sim 0$ samples of Heckman et al. (2015, triangles) and Chisholm et al. (2017, 2018, x-shaped points), while the gray error bar shows the mean uncertainty. Black squares denote median values in two bins of main-sequence offset. The red line and shading represent the relation required to match the evolution of η_{out} with redshift in our models based on the offset of the $z \sim 2.3$ and $z \sim 3.3$ samples from the $z = 0$ SFR- M_* relation, arbitrarily normalized for comparison to the $z \sim 0$ data.

diluted the metals in the ISM while driving up the SFR (e.g., Mannucci et al. 2010; Yates et al. 2012; Dayal et al. 2013). Our results instead suggest that changes in μ_{gas} alone cannot fully account for the observed O/H variation in the FMR. At fixed M_* , galaxies with higher SFR must also have larger η_{out} to explain their lower O/H. In Figure 15, we showed that measurements of η_{out} in local star-forming galaxies positively correlate with SFR at fixed M_* , supporting this scenario.

We thus find that the FMR is not only driven by metal dilution due to variations in gas fractions that reflect accretion rates but also requires variations in metal removal efficiency as a function of SFR. To explain the observed $z \sim 0$ FMR, galaxies above the local star-forming main sequence must have both higher gas fractions and more efficient metal removal through winds (i.e., higher ζ_{out} and η_{out}) than main-sequence galaxies at the same M_* . At fixed M_* , the lower O/H of $z \sim 2.3$ and $z \sim 3.3$ galaxies relative to the $z \sim 0$ MZR reflects their larger μ_{gas} and higher ζ_{out} , in accordance with their higher SFRs, than local main-sequence galaxies. The reason that the FMR does not evolve is because galaxies that have the same M_* and SFR have both similar μ_{gas} and η_{out} over $z = 0$ – 3.3 , consequently yielding similar ISM metallicity. Stated another way, the FMR is redshift invariant out to $z \sim 3.3$ because $\mu_{\text{gas}}(M_*, \text{SFR})$ and $\eta_{\text{out}}(M_*, \text{SFR})$ do not significantly evolve over this redshift range.

6.4. A Constant Z_{out} with M_* is Disfavored

In the discussion above, we have assumed that outflows are dominated by entrained ISM material such that $Z_{\text{out}} \approx Z_{\text{ISM}}$. In contrast, Chisholm et al. (2018) find that Z_{out} is roughly solar metallicity ($Z_{\text{out}} = 1.0 \pm 0.6 Z_{\odot}$) and independent of M_* over 10^7 – $10^{10.5} M_{\odot}$ in the same seven local galaxies analyzed in Chisholm et al. (2017), such that $Z_{\text{out}}/Z_{\text{ISM}} \propto Z_{\text{ISM}}^{-1} \propto M_*^{-0.4}$. Combined with their scaling of $\eta_{\text{out}} \propto M_*^{-0.4}$ (Chisholm et al. 2017), this leads to $\zeta_{\text{out}} \propto M_*^{-0.8}$ ($v_{\text{circ}}^{-3.4}$), much steeper than our

best-fit $z \sim 0$ $\zeta_{\text{out}}(M_*)$ and unable to fit the observed $z \sim 0$ MZR with a low-mass slope of -0.3 . The steep $\zeta_{\text{out}}(M_*)$ of Chisholm et al. (2018) may be due to the properties of the lowest-mass galaxies in their sample. The mass dependence is anchored by two galaxies at $10^7 M_{\odot}$ that both lie ~ 1 dex above the $z = 0$ star-forming main sequence (Cook et al. 2014) and thus may have unrepresentative outflow properties that lead to a steep inferred $\zeta_{\text{out}}(M_*)$. PS11 inferred a similarly steep $\zeta_{\text{out}} \propto v_{\text{circ}}^{-3.5}$ and argued for a relatively flat $Z_{\text{out}}-M_*$ relation in order to explain observed MZRs with steep low-mass slopes (e.g., Tremonti et al. 2004; Kewley & Ellison 2008). However, modern determinations of the $z \sim 0$ MZR yield shallower low-mass slopes that are inconsistent with this scenario (e.g., this work; Blanc et al. 2019; Curti et al. 2020b).

If we assume Z_{out} is a constant $1.0 Z_{\odot}$ with no dependence on M_* or redshift, then $Z_{\text{out}}/Z_{\text{ISM}} \propto Z_{\text{ISM}}^{-1} \propto M_*^{-0.30}$ for our best-fit MZR. Because $\zeta_{\text{out}} \propto M_*^{-0.35 \pm 0.02}$ (Figure 12), this then implies that η_{out} is nearly constant with very little M_* dependence ($\eta_{\text{out}} \propto M_*^{-0.05}$). Neither observations nor theory supports a scenario in which η_{out} is nearly constant with M_* . Theoretically, momentum- and energy-driven winds are expected to have η_{out} scale as $v_{\text{circ}}^{-1} \sim M_*^{-1/3}$ and $v_{\text{circ}}^{-2} \sim M_*^{-2/3}$, respectively (Dekel & Silk 1986; Murray et al. 2005). A scenario where Z_{out} is roughly independent of M_* is therefore disfavored because it requires η_{out} to be nearly independent of M_* or v_{circ} , in conflict with observations and theoretical models of star-formation-driven winds.

7. Summary and Conclusions

We have investigated the evolution of the MZR and the FMR using representative samples of ~ 300 galaxies at $z \sim 2.3$ and ~ 150 galaxies at $z \sim 3.3$ from the MOSDEF survey. Our analysis improves upon past studies by utilizing a larger and more representative high-redshift sample, employing a dust correction method calibrated to H α /H β measurements at $z \sim 2$ for improved SFRs and dereddened line ratios for galaxies lacking either H α or H β detections and applying a uniform metallicity derivation that accounts for evolving ISM conditions. Specifically, we use the same set of emission lines ([O II], [Ne III], H β , and [O III]) to estimate metallicities at all redshifts and apply different calibrations at $z \sim 0$ and $z > 1$, where the $z \sim 0$ relations are calibrated to typical $z \sim 0$ star-forming galaxies while the calibrations used at high redshifts are calibrated to local analogs of high-redshift galaxies that have similar ionization conditions to those in galaxies observed at $z \sim 2$. Despite this careful approach, there is still a nonnegligible systematic uncertainty associated with the choice of metallicity calibration which can be addressed by future work. Larger samples of galaxies at $z > 1$ with direct-method metallicities and multidimensional approaches at $z \sim 0$ capable of taking into account the wide dynamic range of galaxy properties (e.g., sSFR) are needed to make further progress. Our main conclusions are summarized as follows.

1. The line ratios [O III]/H β , O $_{32}$, R $_{23}$, and [Ne III]/[O II] decrease with increasing M_* (Figure 5), as expected if O/H is positively correlated with M_* . These four line ratios evolve significantly from $z \sim 0$ to $z \sim 2.3$ at fixed M_* , but only show a small change from $z \sim 2.3$ to $z \sim 3.3$ (Figure 6), suggesting that the evolution in O/H at fixed M_* is smaller over $z = 2.3$ – 3.3 than over $z = 0$ – 2.3 .

2. Stellar mass and O/H are significantly correlated at $z \sim 2.3$ and $z \sim 3.3$ (Figure 7). Individual galaxies follow a tight sequence around the mean MZR defined by stacked spectra with an intrinsic scatter of ≈ 0.1 dex in O/H, similar to the scatter of the $z \sim 0$ MZR.
3. The low-mass power-law slope of the MZR does not evolve out to $z \sim 3.3$, with a value of $\gamma = 0.28 \pm 0.01$ at $z \sim 0$, 0.30 ± 0.02 at $z \sim 2.3$, and 0.29 ± 0.02 at $z \sim 3.3$ (Figure 8). This remarkable invariance of the MZR slope suggests that the same physical process (i.e., the scaling of ζ_{out} with M_* , see point 7 below) controls the slope of the MZR at low and high redshifts.
4. At fixed M_* , O/H smoothly decreases with increasing redshift as $d\log(\text{O}/\text{H})/dz = -0.11 \pm 0.02$ out to $z \sim 3.3$. This evolution rate is consistent over $\log(M_*/M_\odot) = 9.0$ – 10.5 . The offsets in O/H at $10^{10} M_\odot$ are -0.26 ± 0.02 dex from $z \sim 0$ to $z \sim 2.3$, and -0.10 ± 0.03 dex between $z \sim 2.3$ and $z \sim 3.3$. This gradual metallicity evolution that is uniform across M_* is consistent with MZR evolution in modern cosmological numerical simulations.
5. The FMR does not evolve out to $z \sim 3.3$ (Figure 9). Galaxies at $z \sim 2.3$ and $z \sim 3.3$ fall on the FMR defined by $z \sim 0$ galaxies, with an average offset of < 0.04 dex in O/H for stacked spectra and individual galaxies. The intrinsic scatter of individual $z > 2$ galaxies around the FMR is 0.06 dex in O/H, smaller than the MZR scatter and comparable to the FMR scatter at $z \sim 0$.
6. Using analytic chemical evolution models (Peeples & Shankar 2011), we infer the outflow metal loading factor, $\zeta_{\text{out}} \equiv \frac{Z_{\text{out}}}{Z_{\text{ISM}}} \times \frac{M_{\text{out}}}{\text{SFR}}$, which parameterizes the efficiency with which winds remove metals from the ISM (Figure 12). At all redshifts, ζ_{out} decreases with increasing M_* . The scaling of ζ_{out} with M_* is consistent across $z = 0$ – 3.3 , with $\zeta_{\text{out}} \propto M_*^{-0.35 \pm 0.02}$. At fixed M_* , ζ_{out} increases with increasing redshift as $d\log(\zeta_{\text{out}})/dz = 0.10 \pm 0.03$.
7. The slope of the MZR is primarily set by the scaling of ζ_{out} with M_* at all redshifts over $z = 0$ – 3.3 . Increasing gas fractions with decreasing M_* do not play a major role in setting the low-mass MZR slope. Our models suggest that the low-mass MZR slope is invariant out to $z \sim 3.3$ because the metal removal efficiency of winds scales similarly with M_* over this entire redshift range.
8. The evolution of the normalization of the MZR toward lower O/H at fixed M_* with increasing redshift is driven by both an increase in gas fraction and an increase in ζ_{out} at fixed M_* toward high redshift. Evolution of μ_{gas} and ζ_{out} each account for roughly half of the observed metallicity evolution (Figure 13). Thus, compared to low-redshift galaxies of the same mass, high-redshift galaxies have lower metallicity because metals are more heavily diluted in the gas-rich ISM and metals are more efficiently removed from the ISM through outflows.
9. If the dominant mass component of outflows is entrained ISM gas, then $Z_{\text{out}}/Z_{\text{ISM}} \approx 1$ and the outflow mass-loading factor, $\eta_{\text{out}} \equiv M_{\text{out}}/\text{SFR}$, scales as $\eta_{\text{out}} \propto M_*^{-0.35 \pm 0.02}$. This scaling is in agreement with observations of ionized outflows and recent numerical simulations. At fixed M_* , η_{out} increases with increasing redshift. Observational constraints on η_{out} from rest-UV absorption lines suggest that η_{out} increases with increasing SFR at fixed M_* (Figure 15), consistent with our model when the evolution of the SFR– M_* relation is taken into

account. This model implies that, at fixed M_* , both \dot{M}_{out} and \dot{M}_{in} increase relative to SFR with increasing redshift.

10. The FMR does not evolve out to $z \sim 3.3$ because $\mu_{\text{gas}}(M_*, \text{SFR})$ and $\eta_{\text{out}}(M_*, \text{SFR})$ do not evolve with redshift. Over the range $z = 0$ – 3.3 , galaxies at fixed M_* and SFR have similar O/H and gas fractions, leading us to infer that they must also have similar outflow mass and metal loading factors. The dependence of O/H on SFR at fixed M_* not only reflects dilution of ISM metals from recent accretion but is also driven by variations in the metal removal efficiency of outflows. Variations in η_{out} and μ_{gas} correlate, such that galaxies with higher gas fractions have higher outflow mass loading. This picture is in agreement with theoretical work in which such a link between η_{out} and μ_{gas} arises naturally from density variations in a turbulent ISM.

The redshift-invariant MZR slope and FMR, and the gradual evolution of the MZR over $z = 0$ – 3.3 point to a picture in which galaxies remain close to equilibrium between inflows, outflows, and internal gas processing (star formation and gas reservoir growth) without rapid changes in the mode of galaxy assembly over the past 12 Gyr of cosmic history. While it is not feasible to probe gas-phase metallicity evolution at $z > 4$ with current facilities, JWST will provide rest-optical spectra of galaxies at $z = 4$ – 10 in the near future, opening the door to chemical evolution studies in the earliest epoch of galaxy formation. If gas fractions continue rising rapidly beyond $z = 4$, we expect that the shaping of the MZR transitions from being outflow dominated at $z \lesssim 3$ to gas dominated at very high redshifts, which may manifest in a change in slope or evolution rate. Early galaxies may also be out of equilibrium as the gas reservoir is rapidly built up for the first time (Davé et al. 2012). Extending gas-phase abundance studies beyond $z = 4$ is crucial to understanding the formation of the first generation of galaxies.

Support for this work was provided by NASA through the NASA Hubble Fellowship grant #HST-HF2-51469.001-A awarded by the Space Telescope Science Institute, which is operated by the Association of Universities for Research in Astronomy, Incorporated, under NASA contract NAS5-26555. We acknowledge support from NSF AAG grants AST-1312780, 1312547, 1312764, and 1313171; archival grant AR-13907 provided by NASA through the Space Telescope Science Institute; and grant NNX16AF54G from the NASA ADAP program. We also acknowledge a NASA contract supporting the “WFIRST Extragalactic Potential Observations (EXPO) Science Investigation Team” (15-WFIRST15-0004), administered by GSFC. We additionally acknowledge the 3D-HST collaboration for providing spectroscopic and photometric catalogs used in the MOSDEF survey. We wish to extend special thanks to those of Hawaiian ancestry on whose sacred mountain we are privileged to be guests. Without their generous hospitality, the work presented herein would not have been possible.

Appendix A New Nebular Reddening Correction Calibration

Deriving reddening from the observed flux ratio of hydrogen recombination lines widely separated in wavelength (e.g., $\text{H}\alpha/\text{H}\beta$) is considered the gold standard for the dust correction of nebular emission spectra. This analysis includes a sample at

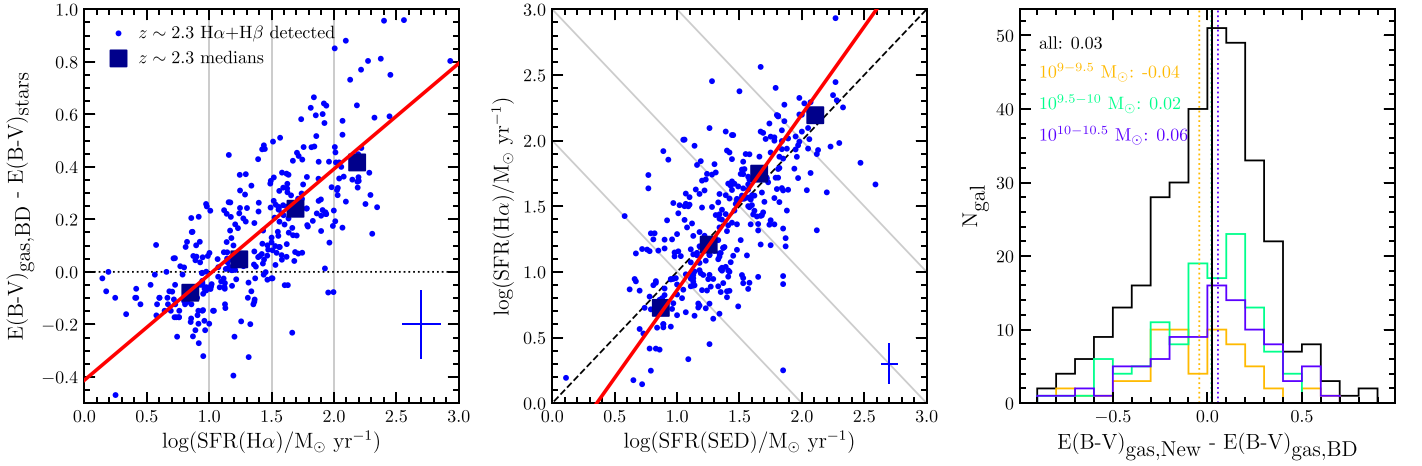


Figure 16. Left: the difference between nebular reddening ($E(B-V)_{\text{gas}}$) and stellar reddening ($E(B-V)_{\text{stars}}$) as a function of $\text{SFR}(\text{H}\alpha)$ for star-forming galaxies at $z \sim 2.3$ with detections of both $\text{H}\beta$ and $\text{H}\alpha$, where $E(B-V)_{\text{gas}}$ is derived using the Balmer decrement. Individual galaxies are shown as blue circles, while medians in bins defined by the gray lines are presented as dark blue squares. The error bar in the lower-right corner denotes the median uncertainty of the individual galaxies. The red line shows the best-fit relation. Middle: $\text{SFR}(\text{H}\alpha)$ versus $\text{SFR}(\text{SED})$, with points and lines as in the right panel. Right: histogram of the difference between $E(B-V)_{\text{gas}}$ derived via our new calibration (Equation (A3)) and $E(B-V)_{\text{gas}}$ inferred from the Balmer decrement. The black line shows the distribution for the entire $z \sim 2.3$ sample, while the colored histograms display the distributions for subsets in stellar mass. Vertical lines show the median offset of each histogram and are given in the text in the top-left corner.

$z=2.9-3.8$ for which $\text{H}\alpha$ is not covered in the spectral bandpass and $\text{H}\beta$ is typically the only H recombination line detected. Furthermore, $\text{H}\beta$ is typically one of the weaker lines and is not detected for all $z \sim 2.3$ sources that have $\text{H}\alpha$ detections. To maximize our sample sizes and avoid biasing the samples by requiring detections of weak lines, we require a dust correction technique that does not rely on detections of certain sets of emission lines. All galaxies in our sample have extensive photometry from which stellar properties (e.g., M_* , $\text{SFR}(\text{SED})$, and $E(B-V)_{\text{stars}}$) were derived through SED fitting (see Section 2.2.2). We calibrated a relation between best-fit properties from SED fitting and $E(B-V)_{\text{gas}}$ derived from the Balmer decrement using a sample of 326 star-forming galaxies at $2.04 \leq z \leq 2.65$ from the MOSDEF survey that has detections of both $\text{H}\alpha$ and $\text{H}\beta$ at $\text{S/N} \geq 3$.

Reddy et al. (2015) noted that the difference between $E(B-V)_{\text{gas}}$ and $E(B-V)_{\text{stars}}$ is a function of $\text{SFR}(\text{H}\alpha)$, where the difference between the reddening of the two components increases with increasing SFR. This relation is displayed in the left panel of Figure 16 for our $z \sim 2.3$ Balmer decrement sample. The best-fit linear relation to the individual galaxies is

$$E(B-V)_{\text{gas}} - E(B-V)_{\text{stars}} = 0.402 \pm 0.019 \times \log\left(\frac{\text{SFR}(\text{H}\alpha)}{M_{\odot} \text{ yr}^{-1}}\right) - 0.413 \pm 0.028, \quad (\text{A1})$$

where the slope and intercept have a covariance of $\rho = -0.94$. Calculating $\text{SFR}(\text{H}\alpha)$ requires a dust correction; therefore, we fit the relation between $\text{SFR}(\text{H}\alpha)$ and $\text{SFR}(\text{SED})$, displayed in the middle panel of Figure 16, obtaining

$$\log\left(\frac{\text{SFR}(\text{H}\alpha)}{M_{\odot} \text{ yr}^{-1}}\right) = 1.338 \pm 0.069 \times \log\left(\frac{\text{SFR}(\text{SED})}{M_{\odot} \text{ yr}^{-1}}\right) - 0.477 \pm 0.098, \quad (\text{A2})$$

with a covariance of $\rho = -0.97$ between the slope and intercept.

Combining Equations (A1) and (A2) yields

$$E(B-V)_{\text{gas}} = E(B-V)_{\text{stars}} - 0.604 + 0.538 \times \log(\text{SFR}(\text{SED})). \quad (\text{A3})$$

Because SFR increases with increasing redshift at fixed M_* while $E(B-V)_{\text{stars}}$ is approximately constant with redshift at fixed M_* (Whitaker et al. 2017; McLure et al. 2018; Cullen et al. 2018), Equation (A3) implies that $E(B-V)_{\text{gas}}$ increases with redshift at fixed M_* . Instead, observations based on the Balmer decrement suggest that $E(B-V)_{\text{gas}}$ at fixed M_* does not significantly evolve out to $z \sim 2.3$ (Theios et al. 2019; A. Shapley et al. 2021, in preparation). At $\log(M_*/M_{\odot}) = 9.9$ (the median mass of our metallicity samples), we find that the mean $\text{SFR}(\text{SED})$ for MOSDEF star-forming galaxies at $z_{\text{med}} = [1.53, 2.29, 3.27]$ is $\langle \log(\text{SFR}(\text{SED})/M_{\odot} \text{ yr}^{-1}) \rangle = [1.26, 1.41, 1.62]$, implying $d\log(\text{SFR}(\text{SED}))/d\log(z) \approx 0.20$. We add a redshift term, normalized to $z = 2.3$, to Equation (A3) to account for the evolution of the $\text{SFR}(\text{SED})$ - M_* relation such that $E(B-V)_{\text{gas}}$ will not evolve at fixed M_* . In this way, we obtain the final expression for dust correction in the absence of a Balmer decrement measurement:

$$E(B-V)_{\text{gas}} = E(B-V)_{\text{stars}} - 0.604 + 0.538 \times [\log(\text{SFR}(\text{SED})) - 0.20 \times (z - 2.3)]. \quad (\text{A4})$$

This calibration is valid over $z \sim 1-4$ and $\log(M_*/M_{\odot}) \sim 9.0-11.0$, and only for stellar properties derived from SED fitting with a similar set of assumptions to ours (Section 2.2.2). Outside of this redshift range, the redshift term may require modification to properly trace the evolution of the star-forming main sequence.

Recent work has suggested that a steep attenuation law similar to the SMC curve is more appropriate for high-redshift galaxies, especially at low M_* and low metallicity (e.g., Capak et al. 2015; Reddy et al. 2018a; Shivaee et al. 2020). If we instead assume subsolar stellar metallicity ($Z_* = 0.0031$) and

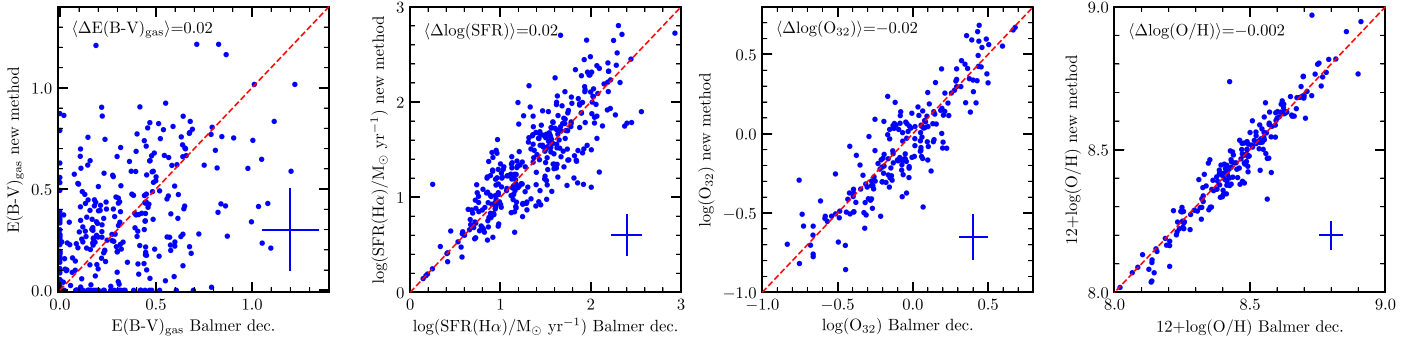


Figure 17. Comparison of $E(B - V)_{\text{gas}}$ (left), SFR($\text{H}\alpha$) (left middle), dust-corrected O_{32} (right middle), and O/H (right) derived using the new $E(B - V)_{\text{gas}}$ calibration (Equation (A3); vertical axis) and $E(B - V)_{\text{gas}}$ based on the Balmer decrement (horizontal axis). Red dashed lines show a one-to-one relation, and the mean vertical offset is given in the upper-left corner of each panel.

the SMC extinction curve of Gordon et al. (2003), the calibration differs:

$$E(B - V)_{\text{gas}} = E(B - V)_{\text{stars}}^{\text{SMC}} - 0.645 + 0.933 \times [\log(\text{SFR}(\text{SED})^{\text{SMC}}) - 0.20 \times (z - 2.3)]. \quad (\text{A5})$$

Equation (A4) should be applied if the Calzetti et al. (2000) curve is assumed for SED fitting, while Equation (A5) should be used in the case of the steeper SMC curve. Note that we obtain consistent nebular reddening estimates for our samples in either case because the SED-derived properties are calibrated to the same Balmer decrement measurements regardless of SED fitting assumptions.

The right panel of Figure 16 displays a histogram of the difference between the new method and Balmer-decrement-derived $E(B - V)_{\text{gas}}$. While there is no significant offset on average between $E(B - V)_{\text{gas}}$ derived using either method, there is significant scatter between the two. The intrinsic scatter between the new and Balmer decrement $E(B - V)_{\text{gas}}$ is 0.23 mag after accounting for measurement uncertainties. This calibration scatter dominates over the formal uncertainties of the best-fit coefficients and is taken into account when estimating SFR, line ratio, and O/H uncertainties (Section 2.2.3). The offset remains small with similar scatter in different bins of M_* (colored histograms in Figure 16), demonstrating that the new reddening calibration will not bias the inferred SFR- M_* relation and MZR. In Figure 17, we compare $E(B - V)_{\text{gas}}$, SFR($\text{H}\alpha$), O_{32} , and O/H derived using this new reddening method to those values obtained using the Balmer decrement. The average offset is small across all four properties,

and no bias is present across the entire dynamic range in each panel.

In Figure 18, we compare $E(B - V)_{\text{gas}}$ derived from the Balmer decrement to three commonly adopted methods in high-redshift galaxy studies: (1) deriving $E(B - V)_{\text{gas}}$ from the rest-frame 1600 Å slope, β_{UV} , (2) $E(B - V)_{\text{gas}} = E(B - V)_{\text{stars}}$, and (3) $E(B - V)_{\text{gas}} = E(B - V)_{\text{stars}}/0.44$. In the first case, we estimated β_{UV} from the photometry (Reddy et al. 2015, 2018b), converted β_{UV} to A_{UV} using the relation of Calzetti et al. (2000), translated A_{UV} to $E(B - V)_{\text{stars}}$ assuming a Calzetti et al. (2000) attenuation curve, and then assumed $E(B - V)_{\text{gas}} = E(B - V)_{\text{stars}}$ derived in this way. In the second and third cases, we use $E(B - V)_{\text{stars}}$ from the best-fit SED model (Section 2.2.2). All three methods show a significant average offset, underestimating $E(B - V)_{\text{gas}}$ in cases 1 and 2 and overestimating it in case 3. The first two cases perform well at low reddening ($E(B - V)_{\text{gas}} < 0.25$), but drastically underestimate $E(B - V)_{\text{gas}}$ with increasing severity as $E(B - V)_{\text{gas}}$ increases, leading to an underestimate of both SFR and metallicity (when based on $[\text{O II}]$, $[\text{O III}]$, and $\text{H}\beta$) for high-mass, dusty objects. Using these two methods, both the SFR- M_* relation and MZR are artificially flattened and have a lower normalization. Assuming $E(B - V)_{\text{gas}} = E(B - V)_{\text{stars}}/0.44$ performs the best out of these methods but still overestimates reddening for low-mass, dust-poor objects. This tension is alleviated if a steeper SMC-like curve is instead assumed for low-mass and low-metallicity galaxies (Shivaei et al. 2020). In summary, our new $E(B - V)_{\text{gas}}$ calibration (Equations (A4) and (1)) performs significantly better than all three of these commonly utilized methods, yielding unbiased SFR and O/H on average.

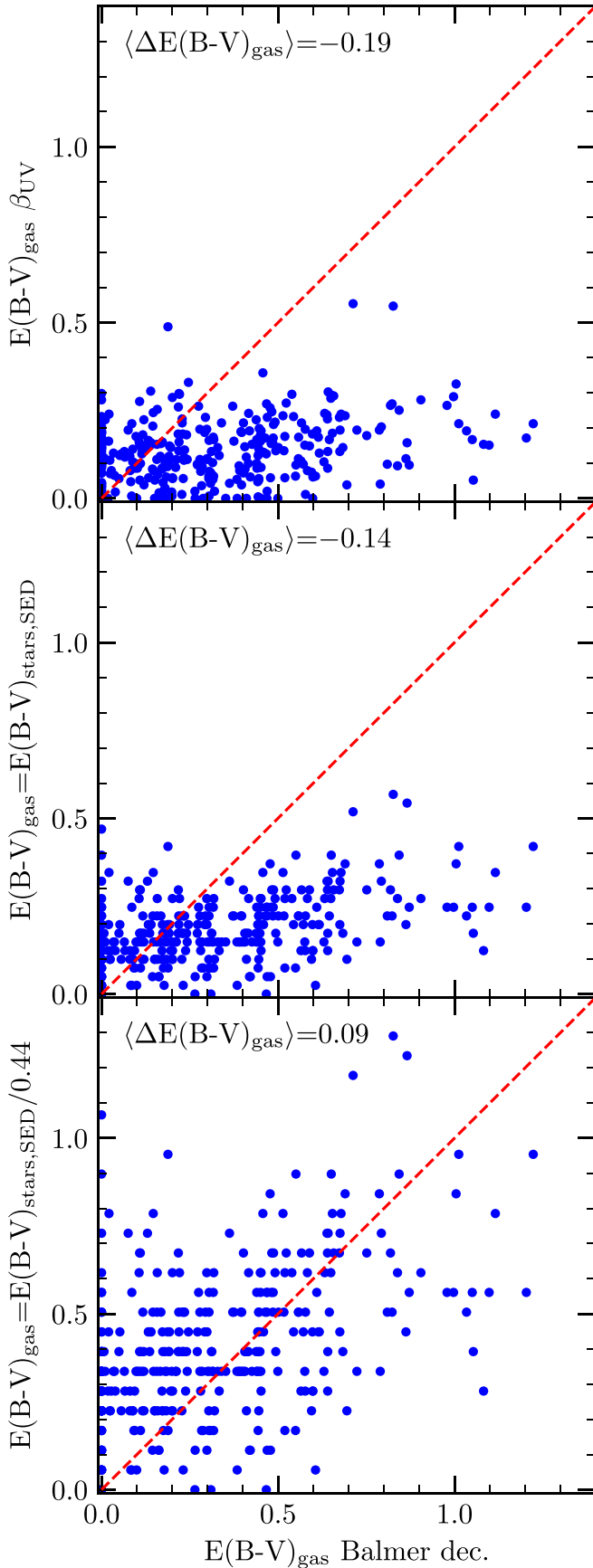


Figure 18. $E(B-V)_{\text{gas}}$ derived from β_{UV} (top), assuming $E(B-V)_{\text{gas}} = E(B-V)_{\text{stars}}$ (middle), and assuming $E(B-V)_{\text{gas}} = E(B-V)_{\text{stars}}/0.44$ (bottom) versus $E(B-V)_{\text{gas}}$ inferred from the Balmer decrement. Red dashed lines show a one-to-one relation, and the mean vertical offset is given in the upper-left corner of each panel.

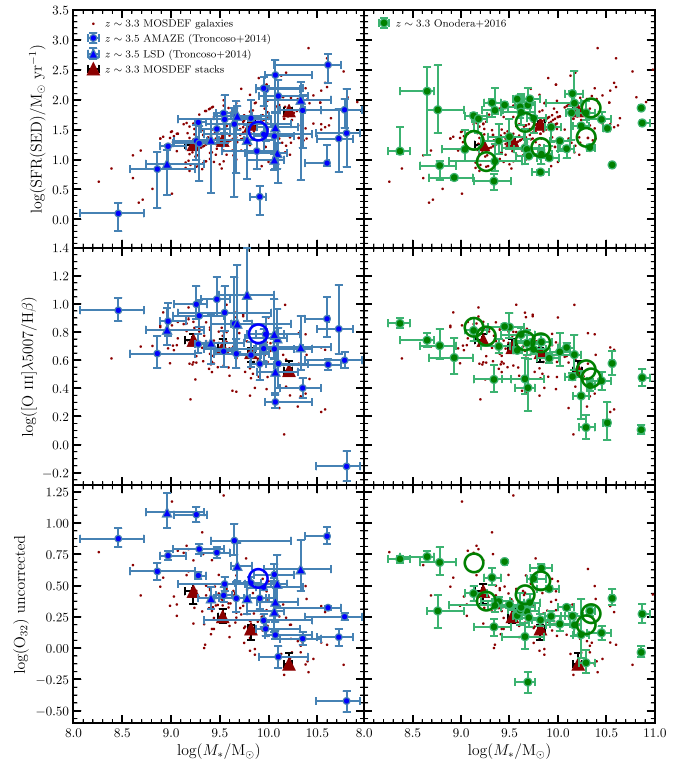


Figure 19. Comparison of the AMAZE+LSD $z \sim 3.4$ sample (left column, blue; Maiolino et al. 2008; Mannucci et al. 2009; Troncoso et al. 2014) and Onodera et al. (2016) $z \sim 3.3$ sample (right column, green) to the MOSDEF $z \sim 3.3$ star-forming galaxies (red). The panels display SFR(SED) (top), $[\text{O III}]\lambda 5007/\text{H}\beta$ (middle), and O_{32} uncorrected for reddening (bottom) versus M_* . The open circle in the left column shows the composite spectrum of all AMAZE+LSD galaxies from Troncoso et al. (2014). The open circles in the right column display the composite spectra in bins of M_* and SFR from Onodera et al. (2016).

















Appendix B Comparison to Literature Samples at $z > 3$

In Figure 19, we compare the properties of the MOSDEF $z \sim 3.3$ star-forming galaxy sample (red, both columns) with those of the AMAZE+LSD $z \sim 3.4$ sample (blue, left column; Maiolino et al. 2008; Mannucci et al. 2009; Troncoso et al. 2014) and the $z \sim 3.3$ sample of Onodera et al. (2016, green, right column). The top panel displays SFR(SED) versus M_* . We choose to compare SFR(SED) instead of the SFR derived from nebular lines because the latter depends on the method used to infer $E(B-V)_{\text{gas}}$. Both literature samples are well matched to the SFR(SED)– M_* relation defined by the MOSDEF galaxies, scattering around the MOSDEF stacks and displaying no obvious biases in SFR. The middle and bottom panels show $[\text{O III}]/\text{H}\beta$ and O_{32} , respectively, as a function of M_* . These line ratios are sensitive to excitation and metallicity such that higher $[\text{O III}]/\text{H}\beta$ and O_{32} correspond to higher excitation and lower metallicity. Here, O_{32} is uncorrected for reddening in order to avoid differences in the inference of $E(B-V)_{\text{gas}}$ between the samples. The Onodera et al. (2016) sample generally follows the sequences described by the MOSDEF $z \sim 3.3$ sample. In contrast, the AMAZE+LSD sample has much higher $[\text{O III}]/\text{H}\beta$ and O_{32} at fixed M_* than the MOSDEF sample. This offset cannot be driven by dust because $[\text{O III}]/\text{H}\beta$ is insensitive to reddening. A consequence is that the AMAZE+LSD sample will have lower O/H at fixed

M_* than the other two samples when applying the same calibrations to all.

The origin of the high-excitation nature of the AMAZE+LSD sample is unclear but is likely related to sample selection. The AMAZE+LSD sample is rest-UV selected using a standard Lyman break technique (Steidel et al. 2003) and should be representative of the Lyman Break Galaxy (LBG) population at $z \sim 3$. The Onodera et al. (2016) sample, on the other hand, is primarily selected based on photometric redshifts using rest-UV to rest-NIR photometry, with an additional requirement that the expected $H\beta$ flux is $>5 \times 10^{-18} \text{ erg s}^{-1} \text{ cm}^{-2}$. Interestingly, the $z \sim 2.3$ KBSS sample (primarily rest-UV selected; Steidel et al. 2014) displays a larger offset than the $z \sim 2.3$ MOSDEF sample (rest-optical selected) in the [NII] BPT diagram despite having similar SFR- M_* distributions, suggesting that the mean excitation properties of LBGs may be different from rest-optical-selected galaxies. These differences highlight the impact that selection effects can have on determinations of the MZR at high redshifts.

ORCID iDs

Ryan L. Sanders  <https://orcid.org/0000-0003-4792-9119>
 Alice E. Shapley  <https://orcid.org/0000-0003-3509-4855>
 Tucker Jones  <https://orcid.org/0000-0001-5860-3419>
 Naveen A. Reddy  <https://orcid.org/0000-0001-9687-4973>
 Mariska Kriek  <https://orcid.org/0000-0002-7613-9872>
 Brian Siana  <https://orcid.org/0000-0002-4935-9511>
 Alison L. Coil  <https://orcid.org/0000-0002-2583-5894>
 Irene Shivaie  <https://orcid.org/0000-0003-4702-7561>
 Romeel Davé  <https://orcid.org/0000-0003-2842-9434>
 Mojegan Azadi  <https://orcid.org/0000-0001-6004-9728>
 Sedona H. Price  <https://orcid.org/0000-0002-0108-4176>
 Gene Leung  <https://orcid.org/0000-0002-9393-6507>
 William R. Freeman  <https://orcid.org/0000-0003-3559-5270>
 Tara Fetherolf  <https://orcid.org/0000-0002-3551-279X>
 Laura de Groot  <https://orcid.org/0000-0001-9022-665X>
 Guillermo Barro  <https://orcid.org/0000-0001-6813-875X>

References

- Andrews, B. H., & Martini, P. 2013, *ApJ*, **765**, 140
 Anglés-Alcázar, D., Faucher-Giguère, C.-A., Kereš, D., et al. 2017, *MNRAS*, **470**, 4698
 Arribas, S., Colina, L., Bellocchi, E., Maiolino, R., & Villar-Martín, M. 2014, *A&A*, **568**, A14
 Azadi, M., Coil, A., Aird, J., et al. 2018, *ApJ*, **866**, 63
 Azadi, M., Coil, A. L., Aird, J., et al. 2017, *ApJ*, **835**, 27
 Baldwin, J. A., Phillips, M. M., & Terlevich, R. 1981, *PASP*, **93**, 5
 Belli, S., Jones, T., Ellis, R. S., & Richard, J. 2013, *ApJ*, **772**, 141
 Berg, D. A., Skillman, E. D., Marble, A. R., et al. 2012, *ApJ*, **754**, 98
 Bian, F., Kewley, L. J., & Dopita, M. A. 2018, *ApJ*, **859**, 175
 Blanc, G. A., Lu, Y., Benson, A., Katsianis, A., & Barraza, M. 2019, *ApJ*, **877**, 6
 Bothwell, M. S., Maiolino, R., Ciccone, C., Peng, Y., & Wagg, J. 2016a, *A&A*, **595**, A48
 Bothwell, M. S., Maiolino, R., Kennicutt, R., et al. 2013, *MNRAS*, **433**, 1425
 Bothwell, M. S., Maiolino, R., Peng, Y., et al. 2016b, *MNRAS*, **455**, 1156
 Bothwell, M. S., Wagg, J., Ciccone, C., et al. 2014, *MNRAS*, **445**, 2599
 Brammer, G. B., van Dokkum, P. G., Franx, M., et al. 2012, *ApJS*, **200**, 13
 Brown, J. S., Martini, P., & Andrews, B. H. 2016, *MNRAS*, **458**, 1529
 Brown, T., Cortese, L., Catinella, B., & Kilborn, V. 2018, *MNRAS*, **473**, 1868
 Calzetti, D., Armus, L., Bohlin, R. C., et al. 2000, *ApJ*, **533**, 682
 Capak, P. L., Carilli, C., Jones, G., et al. 2015, *Natur*, **522**, 455
 Cardelli, J. A., Clayton, G. C., & Mathis, J. S. 1989, *ApJ*, **345**, 245
 Catinella, B., Saintonge, A., Janowiecki, S., et al. 2018, *MNRAS*, **476**, 875
 Chabrier, G. 2003, *PASP*, **115**, 763
 Chisholm, J., Tremonti, C., & Leitherer, C. 2018, *MNRAS*, **481**, 1690
 Chisholm, J., Tremonti, C. A., Leitherer, C., & Chen, Y. 2017, *MNRAS*, **469**, 4831
 Christensen, C. R., Davé, R., Governato, F., et al. 2016, *ApJ*, **824**, 57
 Christensen, L., Richard, J., Hjorth, J., et al. 2012, *MNRAS*, **427**, 1953
 Ciccone, C., Bothwell, M., Wagg, J., et al. 2017, *A&A*, **604**, A53
 Coil, A. L., Aird, J., Reddy, N., et al. 2015, *ApJ*, **801**, 35
 Conroy, C., Gunn, J. E., & White, M. 2009, *ApJ*, **699**, 486
 Cook, D. O., Dale, D. A., Johnson, B. D., et al. 2014, *MNRAS*, **445**, 899
 Cresci, G., Mannucci, F., & Curti, M. 2019, *A&A*, **627**, A42
 Cullen, F., Cirasuolo, M., McLure, R. J., Dunlop, J. S., & Bowler, R. A. A. 2014, *MNRAS*, **440**, 2300
 Cullen, F., McLure, R. J., Dunlop, J. S., et al. 2019, *MNRAS*, **487**, 2038
 Cullen, F., McLure, R. J., Khochfar, S., et al. 2018, *MNRAS*, **476**, 3218
 Curti, M., Cresci, G., Mannucci, F., et al. 2017, *MNRAS*, **465**, 1384
 Curti, M., Maiolino, R., Cirasuolo, M., et al. 2020a, *MNRAS*, **492**, 821
 Curti, M., Mannucci, F., Cresci, G., & Maiolino, R. 2020b, *MNRAS*, **491**, 944
 Dalcanton, J. J. 2007, *ApJ*, **658**, 941
 Davé, R., Anglés-Alcázar, D., Narayanan, D., et al. 2019, *MNRAS*, **486**, 2827
 Davé, R., Finlator, K., & Oppenheimer, B. D. 2011, *MNRAS*, **416**, 1354
 Davé, R., Finlator, K., & Oppenheimer, B. D. 2012, *MNRAS*, **421**, 98
 Davé, R., Rafieferantsoa, M. H., Thompson, R. J., & Hopkins, P. F. 2017, *MNRAS*, **467**, 115
 Davies, R. L., Förster Schreiber, N. M., Übler, H., et al. 2019, *ApJ*, **873**, 122
 Dayal, P., Ferrara, A., & Dunlop, J. S. 2013, *MNRAS*, **430**, 2891
 De Rossi, M. E., Bower, R. G., Font, A. S., Schaye, J., & Theuns, T. 2017, *MNRAS*, **472**, 3354
 Dekel, A., & Silk, J. 1986, *ApJ*, **303**, 39
 Ellison, S. L., Patton, D. R., Simard, L., & McConnachie, A. W. 2008, *ApJL*, **672**, L107
 Erb, D. K., Shapley, A. E., Pettini, M., et al. 2006a, *ApJ*, **644**, 813
 Erb, D. K., Steidel, C. C., Shapley, A. E., et al. 2006b, *ApJ*, **647**, 128
 Faisst, A. L., Capak, P. L., Davidzon, I., et al. 2016, *ApJ*, **822**, 29
 Finlator, K., & Davé, R. 2008, *MNRAS*, **385**, 2181
 Ford, A. B., Davé, R., Oppenheimer, B. D., et al. 2014, *MNRAS*, **444**, 1260
 Förster Schreiber, N. M., Übler, H., Davies, R. L., et al. 2019, *ApJ*, **875**, 21
 Genzel, R., Tacconi, L. J., Lutz, D., et al. 2015, *ApJ*, **800**, 20
 Gordon, K. D., Clayton, G. C., Misselt, K. A., Landolt, A. U., & Wolff, M. J. 2003, *ApJ*, **594**, 279
 Grasshorn Gebhardt, H. S., Zeimann, G. R., Ciardullo, R., et al. 2016, *ApJ*, **817**, 10
 Grogan, N. A., Kocevski, D. D., Faber, S. M., et al. 2011, *ApJS*, **197**, 35
 Gutcke, T. A., & Springel, V. 2019, *MNRAS*, **482**, 118
 Hao, C.-N., Kennicutt, R. C., Johnson, B. D., et al. 2011, *ApJ*, **741**, 124
 Hayward, C. C., & Hopkins, P. F. 2017, *MNRAS*, **465**, 1682
 Heckman, T. M., Alexandroff, R. M., Borthakur, S., Overzier, R., & Leitherer, C. 2015, *ApJ*, **809**, 147
 Henry, A., Scarlata, C., Domínguez, A., et al. 2013, *ApJL*, **776**, L27
 Ho, S. H., Martin, C. L., Kacprzak, G. G., & Churchill, C. W. 2017, *ApJ*, **835**, 267
 Hopkins, P. F., Kereš, D., Oñorbe, J., et al. 2014, *MNRAS*, **445**, 581
 Hunt, L., Dayal, P., Magrini, L., & Ferrara, A. 2016, *MNRAS*, **463**, 2002
 Jeřábková, T., Hasan, Z., Zonoozi, A., Kroupa, P., et al. 2018, *A&A*, **620**, A39
 Jones, T., Martin, C., & Cooper, M. C. 2015, *ApJ*, **813**, 126
 Jones, T., Sanders, R., Roberts-Borsani, G., et al. 2020, *ApJ*, **903**, 150
 Jones, T., Stark, D. P., & Ellis, R. S. 2018, *ApJ*, **863**, 191
 Kacprzak, G. G., van de Voort, F., Glazebrook, K., et al. 2016, *ApJL*, **826**, L11
 Kacprzak, G. G., Yuan, T., Nanayakkara, T., et al. 2015, *ApJL*, **802**, L26
 Kashino, D., Silverman, J. D., Rodighiero, G., et al. 2013, *ApJL*, **777**, L8
 Kashino, D., Silverman, J. D., Sanders, D., et al. 2017, *ApJ*, **835**, 88
 Kashino, D., Silverman, J. D., Sanders, D., et al. 2019, *ApJS*, **241**, 10
 Kauffmann, G., Heckman, T. M., White, S. D. M., et al. 2003, *MNRAS*, **341**, 33
 Kennicutt, R. C., J. 1998, *ApJ*, **498**, 541
 Kewley, L. J., & Dopita, M. A. 2002, *ApJS*, **142**, 35
 Kewley, L. J., Dopita, M. A., Leitherer, C., et al. 2013, *ApJ*, **774**, 100
 Kewley, L. J., & Ellison, S. L. 2008, *ApJ*, **681**, 1183
 Koekemoer, A. M., Faber, S. M., Ferguson, H. C., et al. 2011, *ApJS*, **197**, 36
 Köppen, J., Weidner, C., & Kroupa, P. 2007, *MNRAS*, **375**, 673
 Kriek, M., Shapley, A. E., Reddy, N. A., et al. 2015, *ApJS*, **218**, 15
 Kriek, M., van Dokkum, P. G., Labbé, I., et al. 2009, *ApJ*, **700**, 221
 Kroupa, P. 2001, *MNRAS*, **322**, 231
 Kroupa, P., Tout, C. A., & Gilmore, G. 1993, *MNRAS*, **262**, 545
 Kulas, K. R., McLean, I. S., Shapley, A. E., et al. 2013, *ApJ*, **774**, 130
 Lagos, C. d. P., Theuns, T., Schaye, J., et al. 2016, *MNRAS*, **459**, 2632

- Lara-López, M. A., Cepa, J., Bongiovanni, A., et al. 2010, *A&A*, **521**, L53
- Lee, H., Skillman, E. D., Cannon, J. M., et al. 2006, *ApJ*, **647**, 970
- Leethochawalit, N., Kirby, E. N., Ellis, R. S., Moran, S. M., & Treu, T. 2019, *ApJ*, **885**, 100
- Lelli, F., McGaugh, S. S., & Schombert, J. M. 2016, *ApJL*, **816**, L14
- Lequeux, J., Peimbert, M., Rayo, J. F., Serrano, A., & Torres-Peimbert, S. 1979, *A&A*, **500**, 145
- Leung, G. C. K., Coil, A. L., Aird, J., et al. 2019, *ApJ*, **886**, 11
- Lilly, S. J., Carollo, C. M., Pipino, A., Renzini, A., & Peng, Y. 2013, *ApJ*, **772**, 119
- Liu, D., Schinnerer, E., Groves, B., et al. 2019, *ApJ*, **887**, 235
- Luridiana, V., Morisset, C., & Shaw, R. A. 2015, *A&A*, **573**, A42
- Ly, C., Malkan, M. A., Rigby, J. R., & Nagao, T. 2016, *ApJ*, **828**, 67
- Ly, C., Rigby, J. R., Cooper, M., & Yan, R. 2015, *ApJ*, **805**, 45
- Ma, X., Hopkins, P. F., Faucher-Giguère, C.-A., et al. 2016, *MNRAS*, **456**, 2140
- Maier, C., Lilly, S. J., Ziegler, B. L., et al. 2014, *ApJ*, **792**, 3
- Maiolino, R., Nagao, T., Grazian, A., et al. 2008, *A&A*, **488**, 463
- Mannucci, F., Cresci, G., Maiolino, R., et al. 2009, *MNRAS*, **398**, 1915
- Mannucci, F., Cresci, G., Maiolino, R., Marconi, A., & Gnerucci, A. 2010, *MNRAS*, **408**, 2115
- Martin, C. L., Ho, S. H., Kacprzak, G. G., & Churchill, C. W. 2019, *ApJ*, **878**, 84
- Martin, C. L., Shapley, A. E., Coil, A. L., et al. 2013, *ApJ*, **770**, 41
- McLean, I. S., Steidel, C. C., Epps, H. W., et al. 2012, *Proc. SPIE*, **8446**, 84460
- McLure, R. J., Dunlop, J. S., Cullen, F., et al. 2018, *MNRAS*, **476**, 3991
- Meurer, G. R., Heckman, T. M., & Calzetti, D. 1999, *ApJ*, **521**, 64
- Mitchell, P. D., Schaye, J., Bower, R. G., & Crain, R. A. 2020, *MNRAS*, **494**, 3971
- Momcheva, I. G., Brammer, G. B., van Dokkum, P. G., et al. 2016, *ApJS*, **225**, 27
- Moster, B. P., Naab, T., & White, S. D. M. 2013, *MNRAS*, **428**, 3121
- Moustakas, J., Zaritsky, D., Brown, M., et al. 2011, arXiv:1112.3300
- Muratov, A. L., Kereš, D., Faucher-Giguère, C.-A., et al. 2015, *MNRAS*, **454**, 2691
- Muratov, A. L., Kereš, D., Faucher-Giguère, C.-A., et al. 2017, *MNRAS*, **468**, 4170
- Murray, N., Quataert, E., & Thompson, T. A. 2005, *ApJ*, **618**, 569
- Nelson, D., Pillepich, A., Springel, V., et al. 2019, *MNRAS*, **490**, 3234
- Newman, S. F., Genzel, R., Förster-Schreiber, N. M., et al. 2012, *ApJ*, **761**, 43
- Nomoto, K., Kobayashi, C., & Tominaga, N. 2013, *ARA&A*, **51**, 457
- Nomoto, K., Tominaga, N., Umeda, H., Kobayashi, C., & Maeda, K. 2006, *NuPhA*, **777**, 424
- Okamoto, T., Shimizu, I., & Yoshida, N. 2014, *PASJ*, **66**, 70
- Oke, J. B., & Gunn, J. E. 1983, *ApJ*, **266**, 713
- Onodera, M., Carollo, C. M., Lilly, S., et al. 2016, *ApJ*, **822**, 42
- Oppenheimer, B. D., & Davé, R. 2008, *MNRAS*, **387**, 577
- Osterbrock, D. E., & Ferland, G. J. 2006, *Astrophysics of Gaseous Nebulae and Active Galactic Nuclei* (Melville, NY: Science Univ. Books)
- Pannella, M., Elbaz, D., Daddi, E., et al. 2015, *ApJ*, **807**, 141
- Patrício, V., Christensen, L., Rhodin, H., Cañameras, R., & Lara-López, M. A. 2018, *MNRAS*, **481**, 3520
- Peeples, M. S., & Shankar, F. 2011, *MNRAS*, **417**, 2962
- Peeples, M. S., Werk, J. K., Tumlinson, J., et al. 2014, *ApJ*, **786**, 54
- Pettini, M., & Pagel, B. E. J. 2004, *MNRAS*, **348**, L59
- Price, S. H., Kriek, M., Shapley, A. E., et al. 2016, *ApJ*, **819**, 80
- Puglisi, A., Rodighiero, G., Franceschini, A., et al. 2016, *A&A*, **586**, A83
- Reddy, N. A., Kriek, M., Shapley, A. E., et al. 2015, *ApJ*, **806**, 259
- Reddy, N. A., Oesch, P. A., Bouwens, R. J., et al. 2018a, *ApJ*, **853**, 56
- Reddy, N. A., Shapley, A. E., Sanders, R. L., et al. 2018b, *ApJ*, **869**, 92
- Reddy, N. A., Shapley, A. E., Kriek, M., et al. 2020, *ApJ*, **902**, 123
- Romano, D., Karakas, A. I., Tosi, M., & Matteucci, F. 2010, *A&A*, **522**, A32
- Rudie, G. C., Steidel, C. C., Pettini, M., et al. 2019, *ApJ*, **885**, 61
- Runco, J. N., Shapley, A. E., Sanders, R. L., et al. 2021, *MNRAS*, **502**, 2600
- Saintonge, A., Catinella, B., Cortese, L., et al. 2016, *MNRAS*, **462**, 1749
- Saintonge, A., Catinella, B., Tacconi, L. J., et al. 2017, *ApJS*, **233**, 22
- Salim, S., Lee, J. C., Davé, R., & Dickinson, M. 2015, *ApJ*, **808**, 25
- Salpeter, E. E. 1955, *ApJ*, **121**, 161
- Sancisi, R., Fraternali, F., Oosterloo, T., & van der Hulst, T. 2008, *A&ARv*, **15**, 189
- Sanders, R. L., Jones, T., Shapley, A. E., et al. 2020a, *ApJL*, **888**, L11
- Sanders, R. L., Shapley, A. E., Kriek, M., et al. 2015, *ApJ*, **799**, 138
- Sanders, R. L., Shapley, A. E., Kriek, M., et al. 2016, *ApJ*, **816**, 23
- Sanders, R. L., Shapley, A. E., Kriek, M., et al. 2018, *ApJ*, **858**, 99
- Sanders, R. L., Shapley, A. E., Reddy, N. A., et al. 2020b, *MNRAS*, **491**, 1427
- Sanders, R. L., Shapley, A. E., Zhang, K., & Yan, R. 2017, *ApJ*, **850**, 136
- Savaglio, S., Glazebrook, K., Le Borgne, D., et al. 2005, *ApJ*, **635**, 260
- Schmidt, M. 1959, *ApJ*, **129**, 243
- Schneider, F. R. N., Sana, H., Evans, C. J., et al. 2018, *Sci*, **359**, 69
- Scoville, N., Lee, N., Vanden Bout, P., et al. 2017, *ApJ*, **837**, 150
- Senchyna, P., Stark, D. P., Vidal-García, A., et al. 2017, *MNRAS*, **472**, 2608
- Shapley, A. E., Reddy, N. A., Kriek, M., et al. 2015, *ApJ*, **801**, 88
- Shapley, A. E., Sanders, R. L., Reddy, N. A., et al. 2017, *ApJL*, **846**, L30
- Shapley, A. E., Sanders, R. L., Shao, P., et al. 2019, *ApJL*, **881**, L35
- Shivaei, I., Reddy, N., Rieke, G., et al. 2020, *ApJ*, **899**, 117
- Shivaei, I., Reddy, N. A., Shapley, A. E., et al. 2015, *ApJ*, **815**, 98
- Skelton, R. E., Whitaker, K. E., Momcheva, I. G., et al. 2014, *ApJS*, **214**, 24
- Speagle, J. S., Steinhardt, C. L., Capak, P. L., & Silverman, J. D. 2014, *ApJS*, **214**, 15
- Steidel, C. C., Adelberger, K. L., Shapley, A. E., et al. 2003, *ApJ*, **592**, 728
- Steidel, C. C., Erb, D. K., Shapley, A. E., et al. 2010, *ApJ*, **717**, 289
- Steidel, C. C., Rudie, G. C., Strom, A. L., et al. 2014, *ApJ*, **795**, 165
- Steidel, C. C., Strom, A. L., Pettini, M., et al. 2016, *ApJ*, **826**, 159
- Storey, P. J., & Zeppen, C. J. 2000, *MNRAS*, **312**, 813
- Stott, J. P., Sobral, D., Bower, R., et al. 2013, *MNRAS*, **436**, 1130
- Strom, A. L., Steidel, C. C., Rudie, G. C., et al. 2017, *ApJ*, **836**, 164
- Strom, A. L., Steidel, C. C., Rudie, G. C., Trainor, R. F., & Pettini, M. 2018, *ApJ*, **868**, 117
- Suzuki, T. L., Kodama, T., Onodera, M., et al. 2017, *ApJ*, **849**, 39
- Tacconi, L. J., Genzel, R., Saintonge, A., et al. 2018, *ApJ*, **853**, 179
- Tacconi, L. J., Neri, R., Genzel, R., et al. 2013, *ApJ*, **768**, 74
- Telford, O. G., Dalcanton, J. J., Skillman, E. D., & Conroy, C. 2016, *ApJ*, **827**, 35
- Theios, R. L., Steidel, C. C., Strom, A. L., et al. 2019, *ApJ*, **871**, 128
- Topping, M. W., Shapley, A. E., Reddy, N. A., et al. 2020a, *MNRAS*, **499**, 1652
- Topping, M. W., Shapley, A. E., Reddy, N. A., et al. 2020b, *MNRAS*, **495**, 4430
- Torrey, P., Vogelsberger, M., Marinacci, F., et al. 2019, *MNRAS*, **484**, 5587
- Tremonti, C. A., Heckman, T. M., Kauffmann, G., et al. 2004, *ApJ*, **613**, 898
- Troncoso, P., Maiolino, R., Sommariva, V., et al. 2014, *A&A*, **563**, A58
- Vale Asari, N., Couto, G. S., Cid Fernandes, R., et al. 2019, *MNRAS*, **489**, 4721
- van der Wel, A., Franx, M., van Dokkum, P. G., et al. 2014, *ApJ*, **788**, 28
- Vincenzo, F., Matteucci, F., Belfiore, F., & Maiolino, R. 2016, *MNRAS*, **455**, 4183
- Whitaker, K. E., Pope, A., Cybulski, R., et al. 2017, *ApJ*, **850**, 208
- Woosley, S. E., & Weaver, T. A. 1995, *ApJS*, **101**, 181
- Wuyts, E., Kurk, J., Förster Schreiber, N. M., et al. 2014, *ApJL*, **789**, L40
- Wuyts, E., Rigby, J. R., Sharon, K., & Gladders, M. D. 2012, *ApJ*, **755**, 73
- Wuyts, E., Wisnioski, E., Fossati, M., et al. 2016, *ApJ*, **827**, 74
- Yabe, K., Ohta, K., Akiyama, M., et al. 2015, *PASJ*, **67**, 102
- Yates, R. M., Kauffmann, G., & Guo, Q. 2012, *MNRAS*, **422**, 215
- York, D. G., Adelman, J., Anderson, J. E., Jr, et al. 2000, *AJ*, **120**, 1579
- Zahid, H. J., Dima, G. I., Kudritzki, R.-P., et al. 2014a, *ApJ*, **791**, 130
- Zahid, H. J., Kashino, D., Silverman, J. D., et al. 2014b, *ApJ*, **792**, 75
- Zahid, H. J., Kewley, L. J., & Bresolin, F. 2011, *ApJ*, **730**, 137
- Zhang, K., Yan, R., Bundy, K., et al. 2017, *MNRAS*, **466**, 3217